

12-9-2009

Electromagnetic Field Control and Optimization Using Metamaterials

Jeffrey S. McGuirk

Follow this and additional works at: <https://scholar.afit.edu/etd>

Part of the [Electrical and Computer Engineering Commons](#)

Recommended Citation

McGuirk, Jeffrey S., "Electromagnetic Field Control and Optimization Using Metamaterials" (2009). *Theses and Dissertations*. 1966.
<https://scholar.afit.edu/etd/1966>

This Dissertation is brought to you for free and open access by the Student Graduate Works at AFIT Scholar. It has been accepted for inclusion in Theses and Dissertations by an authorized administrator of AFIT Scholar. For more information, please contact richard.mansfield@afit.edu.



ELECTROMAGNETIC FIELD CONTROL
AND
OPTIMIZATION USING METAMATERIALS

DISSERTATION

Jeffrey S. McGuirk, Major, USAF

AFIT/DEE/ENG/09-13

DEPARTMENT OF THE AIR FORCE
AIR UNIVERSITY

AIR FORCE INSTITUTE OF TECHNOLOGY

Wright-Patterson Air Force Base, Ohio

APPROVED FOR PUBLIC RELEASE; DISTRIBUTION UNLIMITED.

The views expressed in this dissertation are those of the author and do not reflect the official policy or position of the United States Air Force, Department of Defense, or the United States Government.

AFIT/DEE/ENG/09-13

ELECTROMAGNETIC FIELD CONTROL
AND
OPTIMIZATION USING METAMATERIALS

DISSERTATION

Presented to the Faculty
Graduate School of Engineering and Management
Air Force Institute of Technology
Air University
Air Education and Training Command
in Partial Fulfillment of the Requirements for the
Degree of Doctor of Philosophy

Jeffrey S. McGuirk, B.S.E.E., M.S.E.E.

Major, USAF

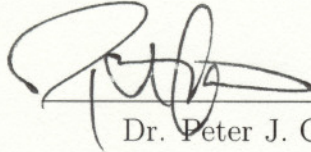
December 2009

APPROVED FOR PUBLIC RELEASE; DISTRIBUTION UNLIMITED.

ELECTROMAGNETIC FIELD CONTROL
AND
OPTIMIZATION USING METAMATERIALS

Jeffrey S. McGuirk, B.S.E.E., M.S.E.E.
Major, USAF

Approved:



Dr. Peter J. Collins (Chairman)

28 SEP 2009

Date



Dr. Michael J. Havrilla (Member)

22 Sep 2009

Date

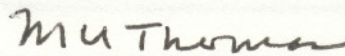


Dr. Aihua W. Wood (Member)

22 Sept. 2009

Date

Accepted:



M. U. Thomas

30 Sep 2009

Date

Dean, Graduate School of Engineering and Management

Abstract

Transformation optics has shown the ability to cloak an object from incident electromagnetic radiation is theoretically possible. However, the constitutive parameters dictated by the theory are inhomogeneous, anisotropic, and, in some instances, singular at various locations. In order for a cloak to be practically realized, simplified parameter sets are required. However, the simplified parameters result in a degradation in the cloaking function.

Constitutive parameters for simplified two-dimensional cylindrical cloaks have been developed with two specific material property constraints. It was initially believed satisfying these two constraints would result in the simplified cylindrical cloaks satisfying the same wave equation as an ideal cloak. Because of this error, the simplified two-dimensional cylindrical cloaks were not perfect. The error in the initial derivation of the original simplified parameter sets was noted in the published literature. However, no analysis was done to determine all material parameter constraints to enable a perfect two-dimensional cylindrical cloak. This research developed a third constraint on the material parameters. It was shown as the material parameters better satisfy this new equation, a two-dimensional cylindrical cloak's hidden region is better shielded from incident radiation. Additionally, a novel way to derive simplified material parameters for two-dimensional cylindrical cloaks was developed. A Taylor series expansion dictated by the new constraint equation led to simplified cloaks with significantly improved scattering width performances when compared to previous published results.

During the course of this research, it was noted all cloak simulations are performed using finite element method (FEM) based numerical methods. While accurate, FEM methods can be computationally intensive and time consuming. A Green's function was used to accurately calculate scattering widths from a two-dimensional

cylindrical cloak with a perfect electrically conducting inner shell. Significant time improvements were achieved using the Green's function compared to an FEM solution particularly as the computational domain size is increased.

Finally, cloaks are physically realized using metamaterials. Design of metamaterials has typically been done empirically. Shifts in S-parameter measurements and the resulting extracted constitutive parameters are used to determine the impact to resonant regions due to various geometries. A new way to design and possibly optimize unit cell metamaterials was investigated using an eigendecomposition method to identify unit cell resonances. Different structures were shown to have different resonances, and control of the resonant locations can lead to optimum designs.

Acknowledgements

First, I must thank my wife and son for their support during this endeavor. Without them, I surely would have gone mad. Also helping to ensure my sanity remained in check was my advisor, Dr. Pete Collins, whose positive attitude kept me going through many dark hours. I must also extend a debt of gratitude to my committee members, Dr. Mike Havrilla and Dr. Aihua Wood, whose mentoring, advice, and keen insights were integral to the success of this research.

Special thanks to Auburn and Dudley, because they always greeted me with a wagging tail, a happy bark, and the unmitigated love and dedication only dogs can have. It's true that petting a four-legged friend is a great stress reliever, and Auburn and Dudley certainly received their share of pets over the last three years.

To my friends in the Behind AFIT Research Facility aka *the BARF*, let me simply say thanks for the camaraderie. You all made it a joy (or at least alleviated the pain) to come to work each day. And although our research areas were different, I believe we all concluded the same thing: When in doubt, go running.

T'is not the destination but the journey.

Jeffrey S. McGuirk

Table of Contents

	Page
Abstract	iv
Acknowledgements	vi
List of Figures	ix
List of Tables	xii
List of Abbreviations	xiii
I. Introduction	1
1.1 Long Term Problem Statement	3
1.2 Transformation Optics	5
1.2.1 Transformation Optics Cloaking Example	7
1.2.2 Cloaking and Transformation Optics	11
1.2.3 Cloaking and the Speed of Light	12
1.3 Summary of Research Goals	13
1.4 Dissertation Organization	15
II. Cloaking Background	16
2.1 Perfect Cloaking Theoretical Analysis	16
2.2 Simplified Cylindrical Cloaks	19
2.3 Cloaking Limitations	26
2.4 Alternate Cloaking Methods	30
2.5 Summary	33
III. Metamaterials Background	34
3.1 Creating Effective Permittivity	36
3.2 Creating Effective Permeability	39
3.2.1 Edge Coupled Split Ring Resonator	39
3.2.2 Omega Split Ring Resonator	40
3.2.3 Additional Structures	42
3.3 Measuring Metamaterial Constitutive Parameters	43
3.3.1 Nicolson-Ross-Weir Algorithm	44
3.3.2 Metamaterial Constitutive Parameter Extraction	47
3.4 Alternate Parameter Retrieval Method	51
3.5 Tunable Metamaterials	52
3.6 Summary	55

	Page
IV. Improved Simplified Parameters for Two-Dimensional Cylindrical Cloaks	56
4.1 Constraint Equations	56
4.2 Reducing field transmission into the hidden region	63
4.3 Improved Cylindrical Cloak Parameters	71
4.4 Analysis of Cloak Performance	74
4.5 Summary	80
V. Computational Improvement Using a Green's Function	82
5.1 Solution Geometry	82
5.2 Green's Function for a Layered PEC Cylinder	85
5.3 FEM and Green's Function Comparison	89
5.4 Summary	93
VI. Metamaterial Eigenfrequency Decomposition	95
6.1 Comsol and the Finite Element Method	95
6.2 Comsol Formulation Verification	100
6.3 Eigendecomposition	101
6.4 Eigendecomposition Verification	102
6.5 S-Parameter Measurements	105
6.6 Unit Cell Eigendecomposition	108
6.7 Summary	111
VII. Conclusions	113
7.1 Research Summary	113
7.2 Recommendations for Future Research	114
7.3 Acknowledgement	117
Appendix A. Material Parameter Derivation	118
Appendix B. Green's Function Derivation	125
Appendix C. Vector Basis Functions	139
Bibliography	146

List of Figures

Figure		Page
1.1.	RCS Measurement Setup	4
1.2.	Generic Transformation Space	6
1.3.	Example Transformation Spaces	7
1.4.	Transformed Coordinate System	9
1.5.	Cloaking Transient Response	13
2.1.	Two-Dimensional Cylindrical Cloak Geometry	19
3.1.	ELC Resonator	37
3.2.	ELC Electric Field Coupling	38
3.3.	ELC Operation with No Magnetic Field Coupling	38
3.4.	Edge Coupled Split Ring Resonator	39
3.5.	Ω -Ring Geometry	41
3.6.	Axially Symmetric Ring	42
3.7.	S-Ring Geometry	43
3.8.	Unit Cell Geometry for Simplified Cloak Construction	44
3.9.	Tuned Metamaterial Using Capacitors	53
3.10.	Tuned Metamaterial Using Variable Capacitor	54
3.11.	Tuned Metamaterial Using N-Type Silicon	54
4.1.	Scattered Field Magnitude for Various Cloaked Objects	60
4.2.	Normalized Scattering Width for Various Cloaked Objects	60
4.3.	Scattering Width Differences for PEC Cylinder and Square	61
4.4.	Scattered Electric Field of Various Improved Cloaked Objects	62
4.5.	Normalized Scattering Widths for Improved Cloaked	62
4.6.	Scattering Width Differences for PEC Cylinder and Square in Improved Cloak	63
4.7.	Calculated Values for the Left Side of Equation 4.13	64

Figure		Page
4.8.	Scattering Width Difference for Alternate Cloak 1	65
4.9.	Scattering Width Difference for Alternate Cloak 2	66
4.10.	Hidden Region Electric Field Magnitude	67
4.11.	Scattering Widths for Cloaked PEC Cylinders	68
4.12.	Scattered Electric Field Magnitude for Alternate Cloak 3	69
4.13.	Normalized Scattering Width	69
4.14.	Material Parameter Behavior as a Function of r	73
4.15.	Real Part of Total E_z	75
4.16.	Real Part of Scattered E_z	76
4.17.	Real Part of Scattered E_z for Second Order Cloak	77
4.18.	Scattering Width for Empty Simulation Domain	78
4.19.	Comparison of Cloak Scattering Width Performance	79
4.20.	Performance of Cloak Scattering Width for Large b	80
5.1.	FEM Simulation Geometry	83
5.2.	Analytic and FEM-Determined PEC Cylinder Scattering Width	84
5.3.	Green's Function Derivation Problem Geometry	86
5.4.	Scattering Width Results for 20-Layer Isotropic Cloak	90
5.5.	Scattering Width Results for 40-Layer Isotropic Cloak	91
5.6.	FEM Larger Computational Domain Geometry	92
5.7.	Scattering Widths for Larger Cloaked PEC Cylinder	93
6.1.	PEC Rectangular Resonator Geometry	103
6.2.	PEC Resonator Eigenfrequencies	104
6.3.	Unit Cell for S-Parameter Measurements	106
6.4.	S-Parameter Measurements and Extracted Index of Refraction	107
6.5.	S-Parameter Magnitude Comparison for Mesh Densities	108
6.6.	S-Parameter Magnitudes for Gap Modifications	109
6.7.	Eigenvalues for Gap Modifications	110
6.8.	Eigenvalues from 6-18 GHz	111

Figure		Page
6.9.	Extracted Eigenfrequencies Using Different Meshes	112
7.1.	Three-Dimensional Cylindrical Cloak	115
A.1.	Differential Parallelepiped Element	120
A.2.	Line Integral Differential Components	121
B.1.	Problem Geometry for Green's Function Derivation	125
B.2.	Green's Function Verification	138
C.1.	Local Tetrahedral Element	139

List of Tables

Table		Page
4.1.	Total Hidden Region Energy and Outer Layer Impedance . . .	66
4.2.	Simplified Material Parameter Values	72
5.1.	Analytic and FEM Solution Comparisons	85
6.1.	Eigenfrequencies in GHz for PEC Rectangular Resonator . . .	105
6.2.	Mesh Density and Impedance Matrix Size	107
C.1.	Edge Node Numbers	140
C.2.	Example Tetrahedral Element Node Locations	142

List of Abbreviations

Abbreviation		Page
RCS	Radar Cross Section	1
RAM	Radar Absorbing Materials	1
DUT	Device Under Test	2
FDTD	Finite-Difference Time-Domain	12
PEC	Perfect Electric Conductor	15
FEM	Finite Element Method	18
TM	Transverse Magnetic	18
TE	Transverse Electric	20
DNG	Double Negative	34
ELC	Electric-Inductive-Capacitive	37
EC-SRR	Edge Coupled Split Ring Resonator	39
NRW	Nicolson-Ross-Weir	45
HFSS	High Frequency Structure Simulator	50
MEMS	Microelectromechanical Systems	53
MEL	Maximum Element Length	84
NRTF	National Radar Cross Section Test Facility	117

ELECTROMAGNETIC FIELD CONTROL
AND
OPTIMIZATION USING METAMATERIALS

I. Introduction

Radar cross section (RCS) reduction has been a goal of scientists and engineers since the first major uses of radar in World War II. A wide body of knowledge exists on passive techniques used to control scattering due to incident electromagnetic energy. These techniques can be divided into two main sub-categories: shaping and radar absorbing materials (RAM). The effectiveness of both categories are typically dependent on the frequency, incident angle, and polarization of the illuminating energy.

The goal of shaping is to scatter the incident energy from the target such that the amount of energy returned toward the radar is minimized. This type of RCS control has proven to be very effective for monostatic radars where the transmit and receive antennas are collocated. For a threat aircraft, the attack profile can be controlled such that a small range of target angles will be presented to the radar. Shaping can be used to reduce the RCS at these angles and increase the aircraft's stealthiness. However, a rule of thumb for shaping is a reduction in the RCS at one aspect angle is always accompanied by an increase at another [49]. Consider a two-dimensional RCS (i.e. echowidth). If all 360° of measurement angles are equally important, shaping will reduce the echowidth at one angle while increasing it at another angle (or several other angles). In some instances, this is acceptable. As an example, the technique of lobe width control allows the RCS to balloon in certain sectors where significant scattered energy does not impact the desired result. In other instances, lobe width control is an unacceptable way to control RCS. It is easy to see a low-RCS threat designed to act against a monostatic radar will have a significantly reduced capability against a

bistatic radar, whether the bistatic radar is an integrated network of transmitters and receivers or if the radar is simply making use of transmitters of opportunity.

The goal of RAM is to convert the incident electromagnetic energy into heat, thereby reducing the amount of scattered electromagnetic energy capable of being detected by the radar sensors. Note RAM cannot reduce the forward scatter of an object, but it is very effective in controlling the back scatter. This can be done with either an electric or magnetic loss tangent in the RAM material. Narrow band RAM coatings, such as the Salisbury screen and Dallenbach layer, have been used since the 1950's [94]. Modern radar systems span a wide range across the electromagnetic spectrum, with most operating between 220 MHz - 35 GHz; however, over-the-horizon and millimeter wave radars operate outside this range [87]. Many radars also have a wide operational bandwidth. Therefore, wide band RAM is very desirable. The first broadband absorber was a Jaumann absorber, which can be thought of as a multilayered Salisbury screen [94]. Another type of broadband RAM are the carbon-loaded foam absorbers used in anechoic chambers to limit the scattered energy from surfaces other than the device-under-test (DUT) [48]. Typical RAM employed on modern aircraft is some type of iron ball paint. The paint contains tiny spheres coated with carbonyl iron or ferrite. Incident electromagnetic energy interacts with these spheres, resulting in the electromagnetic energy being converted to heat [3].

There are significant implications when using RAM. First, most are toxic to some degree. During the first Gulf War, maintenance crews noted a large number of dead bats in the hangars where the F-117 was kept. Their deaths were attributed to long exposure to the RAM coupled with a lack of ventilation [1]. Additionally, RAM coatings require precise application methods, as the coating thickness and smoothness must be uniform across the surface of the substrate. The application process typically involves robotic sprayers that can accurately control the coating thickness [3]. Furthermore, the applied coatings require strict constitutive parameter tolerances as well as uniformity in order to achieve the desired result. Therefore, costs increase drastically when working with RAM. Also, any type of RAM coating increases an

object's weight. For aircraft, weight increases can have significant impact on performance. RAM is not simply a covering that can be easily applied to an aircraft or other body to reduce its RCS. Rather, working with RAM, from its manufacture to application, is a technically detailed, costly process.

When used together, shaping and RAM make effective RCS reduction tools, but the limits of their effectiveness are being approached in the field of RCS measurements. These limits are particularly noticeable when the DUT has a low RCS. The low RCS makes it difficult to differentiate radar returns resulting from the DUT and other objects inherent in the measurement system. This limitation is discussed in the following section.

1.1 Long Term Problem Statement

RCS measurements are obtained using test ranges. Static test ranges can be either indoor or outdoor, with each having its positives and negatives. For physically large targets, an outdoor test range is typically required. The ideal outdoor test range has minimal background signals and little to no secondary scattering sources. This allows the measured RCS to be as close to the actual RCS as possible. To avoid ground bounce interaction, the target is mounted a considerable distance off the ground. A metal pylon is often used as the primary support structure. Other support systems exist, such as foam columns and string support systems [48], but neither is currently capable of supporting heavy or awkwardly shaped targets. The basic measurement setup is shown in Figure 1.1. The top picture is an aerial view of an outdoor range in New Mexico. A bank of antennas is located at one end of the range (lower right in Figure 1.1). The different antennas allow for different frequency bands to be measured. The target is located opposite the antenna bank (lower left in Figure 1.1). Note the absence of any significant structures surrounding the pylon and radar.

The target can be rotated and inclined to allow measurements of all desired azimuth and elevation angles. The pylon itself does not rotate, but, like all objects,

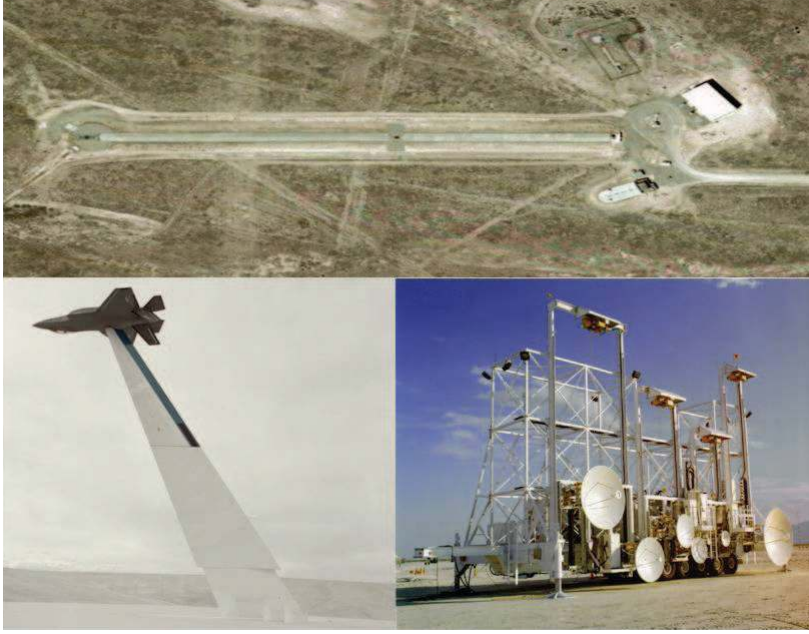


Figure 1.1: RCS Measurement Setup [4–6]

it scatters incident energy. Pylons have been shaped to enable them to support significant weight while minimizing RCS in the backscattering direction. Additionally, RAM has also been incorporated into the pylons' designs to help reduce the scattered energy.

The collected data is processed to calculate the DUT's RCS. The calculation used to determine the RCS is a vector background subtraction defined as [24]

$$\sigma = \left| \frac{\vec{E}_T^s - \vec{E}_{TB}^s}{\vec{E}_C^s - \vec{E}_{CB}^s} \right|^2 \sigma_{CAL}, \quad (1.1)$$

where σ is the measured RCS, \vec{E}_T^s is the scattered field when the target is mounted on the pylon, \vec{E}_{TB}^s is the scattered field when the target is not on the pylon, \vec{E}_C^s is the scattered field from a calibration target, \vec{E}_{CB}^s is the scattered field when the calibration target is removed, and σ_{CAL} is the calculated RCS of the calibration target. Additionally, the calibration target is typically a simple shape with an easily theoretically determined RCS. This calibration is done to identify and remove sources of

scattered energy other than the DUT as well as compensate for systematic errors due to the non-ideal radar. However, the calibration, while good, is limited. Equation 1.1 cannot be used to calibrate scattered energy resulting from a target-pylon interaction. This is when the scattered energy from the target (pylon) strikes the pylon (target) and results in a signal measured by the radar. Such a return is only present when the target is mounted on the pylon. Thus, it cannot be corrected via a calibration. Typically, fields from this type of interaction are small compared to the target's scattered field. However, for low RCS targets, the interaction can be on the same order of magnitude. Therefore, a way to reduce the bistatic RCS of the pylon is required. A bistatic reduction is necessary because the energy scattered from the target can strike the pylon from a large number of angles. RAM and shaping have been successfully used, but as the DUT RCS continues to decrease, an alternate way to control the component of the scattered field resulting from a target-pylon interaction is required.

1.2 Transformation Optics

Transformation optics is a relatively new field that provides the fundamental theory enabling precise control of electromagnetic waves. Control of electromagnetic waves is certainly not a new technology. Waveguides and fiber optics have been doing just that for over a century. A key distinction is waveguides and fiber optics are guiding structures operating such that their boundaries confine the fields within a desired space. Transformation optics uses a smooth variation in the media constitutive parameters to steer the fields in a desired manner. The precision with which transformation optics allows one to control an electromagnetic field is unprecedented and could lend itself to the target-pylon scattering reduction problem.

Transformation optics works because geometric rays propagate along a given trajectory and obey Fermat's principle. Fermat's principle states light waves of a given frequency propagate along the path between two points which takes the least time [64]. For an isotropic, homogeneous medium, the result is that light rays propagate in a straight line. However, when the medium is anisotropic and inhomogeneous, the path

which the rays travel can be quite complex. Thus, by controlling the constitutive material parameters $(\vec{\mu}_r, \vec{\epsilon}_r)$, electromagnetic energy can be guided in any way one sees fit. But how does one exactly design a desired electromagnetic response in a system? Specifically, other than using trial and error, how can one design the required constitutive parameters of a medium to result in a desired electromagnetic effect?

Theoretically, it is actually quite simple. First, one develops a transformed space in which electromagnetic waves propagate in a desired manner. A generic transformed space is shown in Figure 1.2. This new space is then related to Cartesian coordinates

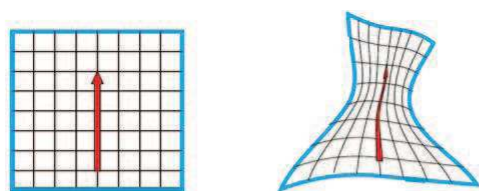


Figure 1.2: Generic transformation space [93]

using a coordinate transformation. Ward and Pendry showed Maxwell's equations are invariant under any type of coordinate transform i.e. the equations are the same in all coordinate systems with only the permittivity and permeability changing values [97]. Thus, in the transformed space, Maxwell's equations correctly describe the behavior of the electromagnetic waves. One may use the invariance of Maxwell's equations to derive a material with constitutive parameters defined using a permittivity and permeability tensor. When this material is placed in Cartesian coordinates, the resulting field behavior accurately mimics the field behavior in the transformed space (reference Appendix A). The material defined by the permittivity and permeability tensors is what creates the desired electromagnetic effects. The permittivity and permeability tensors are easily calculable once the coordinate transformation has been defined.

The transformed space can encompass any type of electromagnetic behavior one desires provided a one-to-one transformation exists between the coordinate systems. Simple waveguide bends, field concentrators, and space that contains holes where no radiation is present are just some examples that have been simulated in computational

software packages. These transformed spaces and simulation results are shown in Figure 1.3.

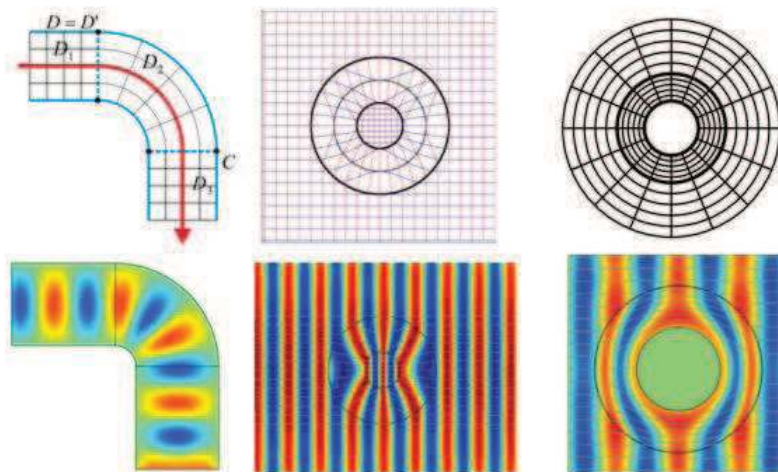


Figure 1.3: Transformation spaces such as a waveguide bend [93], a field concentrator [73], and a cylindrical cloak [56]

At this point, it is instructive to discuss precisely how the medium’s constitutive parameters are derived. As an example, consider electromagnetic cloaking. The ability to cloak an object using metamaterials (defined in Chapter III) was first discussed by Pendry *et al.* [72] and Leonhardt [55] in 2006. The techniques discussed by each are similar, but this research focuses on Pendry’s method, which uses the transformation optics approach described above. An electromagnetic cloak guides energy around a particular region much like flowing water is guided around a stone. The hidden region is void of electromagnetic energy, meaning an object can be placed in the hidden region without perturbing the field. What follows below is an example of the transformation optics approach used to derive the material parameters for an infinitely long cylindrical electromagnetic cloak.

1.2.1 Transformation Optics Cloaking Example. Per transformation optics, the behavior of electromagnetic waves in a transformed coordinate system can be modeled in Cartesian coordinates using a material with specific permittivity and permeability tensors [72, 97]. This derivation is shown in detail in Appendix A, and

the resulting constitutive parameter tensors are given by

$$\hat{\varepsilon}^{ij} = g^{ij} |\hat{u}_1 \cdot (\hat{u}_2 \times \hat{u}_3)| Q_1 Q_2 Q_3 (Q_i Q_j)^{-1}, \quad (1.2)$$

$$\hat{\mu}^{ij} = g^{ij} |\hat{u}_1 \cdot (\hat{u}_2 \times \hat{u}_3)| Q_1 Q_2 Q_3 (Q_i Q_j)^{-1}, \quad (1.3)$$

where g^{ij} are the components of the inverse of the coordinate system's metric tensor which is defined as

$$g = \begin{pmatrix} \hat{u}_1 \cdot \hat{u}_1 & \hat{u}_1 \cdot \hat{u}_2 & \hat{u}_1 \cdot \hat{u}_3 \\ \hat{u}_2 \cdot \hat{u}_1 & \hat{u}_2 \cdot \hat{u}_2 & \hat{u}_2 \cdot \hat{u}_3 \\ \hat{u}_3 \cdot \hat{u}_1 & \hat{u}_3 \cdot \hat{u}_2 & \hat{u}_3 \cdot \hat{u}_3 \end{pmatrix}. \quad (1.4)$$

Note \hat{u}_i are the unit vectors in the $i = 1, 2, 3$ direction in the transformed coordinate system, and

$$Q_{ij} = \frac{\partial x}{\partial q_i} \frac{\partial x}{\partial q_j} + \frac{\partial y}{\partial q_i} \frac{\partial y}{\partial q_j} + \frac{\partial z}{\partial q_i} \frac{\partial z}{\partial q_j}, \quad (1.5)$$

$$Q_i^2 = Q_{ii}, \quad Q_i = \sqrt{Q_{ii}}. \quad (1.6)$$

An electromagnetic cloak can be developed by creating a transformed coordinate system that contains voids where electromagnetic energy will not propagate. The electromagnetic field behavior in the transformed coordinate system is then mimicked in Cartesian coordinates using a material with permeability and permittivity whose properties are described by Equations 1.2 and 1.3.

Consider a transformed cylindrical coordinate system with coordinates (r', θ', z') such that all points in Cartesian space where $r < b$ are mapped to the annular region, $a < r' < b$. This can be written mathematically as

$$r' = \left(1 - \frac{a}{b}\right) r + a, \quad (1.7)$$

where r' is the radial location in the transformed coordinate system and r is the radial location in a Cartesian coordinate system. The result is a transformed coordinate system where there are no points in the region $r' < a$. This is shown in Figure 1.4. In

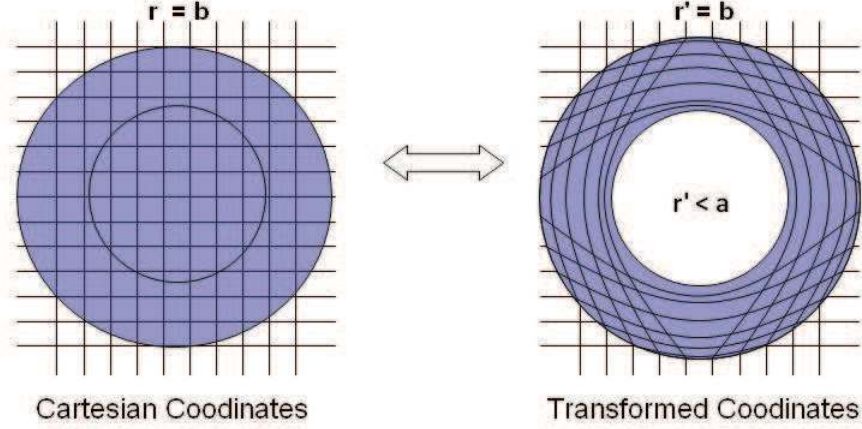


Figure 1.4: Transformed Coordinate System

the transformed coordinate system, no electromagnetic energy will propagate in the region $r' < a$ because this region theoretically does not exist. Space is curved around it.

The permittivity and permeability tensors which electromagnetically mimic the curvature of the transformed space can be found as follows. The mapping from the transformed coordinate system where $r' < a$ does not exist to Cartesian coordinates can be written as

$$x = \frac{(r' - a)b}{b - a} \cos \theta', \quad y = \frac{(r' - a)b}{b - a} \sin \theta', \quad z = z'. \quad (1.8)$$

Note the transformed coordinate system is an orthogonal coordinate system with unit vectors \hat{r} , $\hat{\theta}$, and \hat{z} . Thus, the metric tensor is

$$g = \begin{pmatrix} \hat{r} \cdot \hat{r} & \hat{r} \cdot \hat{\theta} & \hat{r} \cdot \hat{z} \\ \hat{\theta} \cdot \hat{r} & \hat{\theta} \cdot \hat{\theta} & \hat{\theta} \cdot \hat{z} \\ \hat{z} \cdot \hat{r} & \hat{z} \cdot \hat{\theta} & \hat{z} \cdot \hat{z} \end{pmatrix} = \begin{pmatrix} 1 & 0 & 0 \\ 0 & 1 & 0 \\ 0 & 0 & 1 \end{pmatrix}. \quad (1.9)$$

This result simplifies the expressions in Equations 1.2 and 1.3 due to the fact

$$g^{ij} \left| \hat{r} \cdot (\hat{\theta} \times \hat{z}) \right| = \delta_{ij}, \quad (1.10)$$

where δ_{ij} is the Kronecker delta function. Next, the Q_i^2 values can be found.

$$Q_1^2 = \left(\frac{\partial x}{\partial r}\right)^2 + \left(\frac{\partial y}{\partial r}\right)^2 + \left(\frac{\partial z}{\partial r}\right)^2 \quad (1.11)$$

$$Q_2^2 = \left(\frac{1}{r} \frac{\partial x}{\partial \theta}\right)^2 + \left(\frac{1}{r} \frac{\partial y}{\partial \theta}\right)^2 + \left(\frac{1}{r} \frac{\partial z}{\partial \theta}\right)^2 \quad (1.12)$$

$$Q_3^2 = 1 \quad (1.13)$$

The partial derivatives can be expressed as

$$\frac{\partial x}{\partial r} = \frac{b}{b-a} \cos \theta, \quad \frac{\partial y}{\partial r} = \frac{b}{b-a} \sin \theta, \quad \frac{\partial z}{\partial r} = 0. \quad (1.14)$$

$$\frac{1}{r} \frac{\partial x}{\partial \theta} = -\frac{(r-a)b \sin \theta}{b-a} \frac{1}{r}, \quad \frac{1}{r} \frac{\partial y}{\partial \theta} = \frac{(r-a)b \cos \theta}{b-a} \frac{1}{r}, \quad \frac{1}{r} \frac{\partial z}{\partial \theta} = 0. \quad (1.15)$$

$$\frac{\partial x}{\partial z} = 0, \quad \frac{\partial y}{\partial z} = 0, \quad \frac{\partial z}{\partial z} = 1. \quad (1.16)$$

Multiplying out, the result is

$$Q_1 = \frac{b}{b-a}, \quad (1.17)$$

$$Q_2 = \frac{r-a}{r} \frac{b}{b-a}, \quad (1.18)$$

$$Q_3 = 1. \quad (1.19)$$

Using these values in Equations 1.2 and 1.3 results in the following for the permittivity and permeability tensors [79].

$$\varepsilon_r = \mu_r = \frac{r-a}{r} \quad (1.20)$$

$$\varepsilon_\theta = \mu_\theta = \frac{r}{r-a} \quad (1.21)$$

$$\varepsilon_z = \mu_z = \left(\frac{r-a}{r}\right) \left(\frac{b}{b-a}\right)^2 \quad (1.22)$$

These can be rewritten as a tensor where the non-diagonal terms in the tensor matrix are zero.

$$\vec{\mu} = \vec{\varepsilon} = \begin{pmatrix} \frac{r-a}{a} & 0 & 0 \\ 0 & \frac{r}{r-a} & 0 \\ 0 & 0 & \left(\frac{b}{b-a}\right)^2 \frac{r-a}{r} \end{pmatrix} \quad (1.23)$$

A material with the parameters shown in Equation 1.23 and immersed in free space will guide all electromagnetic energy around the region, $r < a$, much like the energy would propagate in the transformed coordinate system shown in Figure 1.4. Thus, any object placed in this region will not scatter any electromagnetic energy. Hence, the material parameters shown in Equation 1.23 effectively define an electromagnetic cloak.

1.2.2 Cloaking and Transformation Optics. As shown in the previous section, it is theoretically possible to guide incident electromagnetic energy around an object such that the object has no scattered field. One simply needs to use a material having the constitutive properties described by Equation 1.23. Transformation optics led to this result and, in essence, showed cloaking is theoretically possible [72]. However, this does not mean the hard part is done. Quite the contrary, the difficulty lies in developing a material with the desired constitutive parameters. Note the spatial variation in the cylindrical cloak's material parameters. Adding to the complexity is the material parameter anisotropy. A material with the properties shown in Equation 1.23 does not exist naturally. Fortunately, advances in micro- and nano-fabrication methods have allowed the creation of man-made materials using sub-wavelength structures with the desired material properties dictated by transformation optics [83]. Such materials are commonly referred to as metamaterials. Metamaterials are the enabling building blocks to a number of applications spawned from transformation optics. Metamaterials will be discussed in detail in Chapter III.

Metamaterials do not yet enable one to manufacture an ideal cloak with the parameters describe by Equation 1.23. At r close to a , the diagonal terms in Equation

1.23 are going to either zero or infinity. A material with infinite permittivity/permeability will likely never be possible to manufacture. Also, all existing materials have at least some type of loss. Creating lossless materials, particularly those with magnetic effects, is extremely difficult. Additionally, the required material parameters have anisotropic and spatially varying μ and ε , which is quite challenging to make. However, simplifications to the material parameter set can be made (Section 2.2). These simplifications result in less-than-ideal cloaking performance, but the end result does maintain some of the ideal cloak's electromagnetic wave-controlling properties. A simplified cylindrical cloak with a material parameter set derived from the ideal parameters shown in Equation 1.23 has recently been manufactured and tested [79] with promising results.

1.2.3 Cloaking and the Speed of Light. It has been shown it is possible to cloak a region of space such that an observer would not see any difference in the electromagnetic fields when an object is placed in this hidden region. This seems to violate the fact that energy cannot propagate faster than the speed of light. After all, the energy must be bent around an object and maintain the same relative phase as the energy propagating in free space. Since curving around an object requires the energy to travel a further distance, it seems that the energy must propagate faster than the speed of light. However, this is not exactly how the cloaking process works. The energy does have to travel a longer distance. However, the cloak is not transporting energy faster than the speed of light. Rather, stored energy built up during the transition from the transient to the steady-state phase allows only one specific frequency's phase fronts to exceed the speed of light [2]. This was demonstrated by Liang *et al.* using a finite-difference time-domain (FDTD), with the results shown in Figure 1.5. Note how it does take some time for the cloak to reach its stable state. The time in Figure 1.5 image (a), where the incident wave first reaches the cloak until steady-state is reached in image (f) is approximately 15 periods of the the incident field [59].

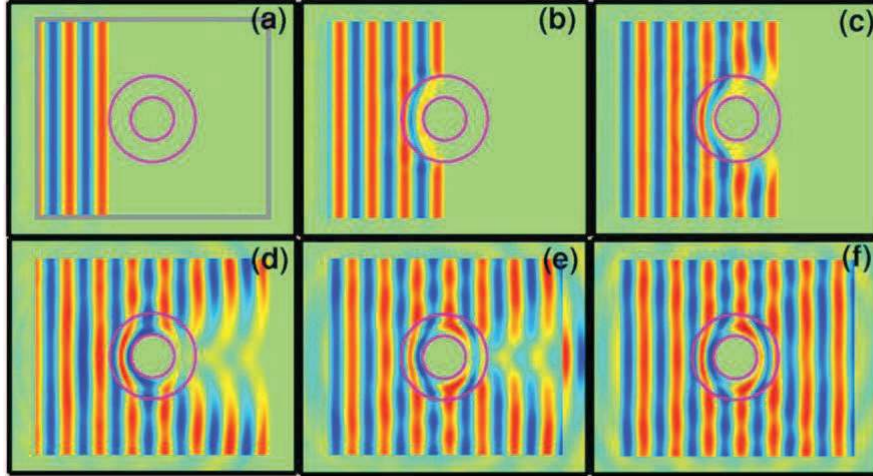


Figure 1.5: Cylindrical cloak response in the transient to steady-state phase. [59]

While still a long way from implementing a cloaking device as seen in *Star Trek*, cloaks present a new paradigm in terms of RCS reduction, whether it be creating an ideal cloak (not likely in the near future) or using a modified cloaking structure in conjunction with shaping and RAM to further reduce an object's overall signature. Developing a cloaking mechanism for a support pylon on an RCS range could help reduce the target-pylon interactions which result in the undesired scattered fields due to target-pylon interactions discussed in Section 1.1.

1.3 Summary of Research Goals

The intent of this research is to investigate whether cloaks are a viable option for the stated long-term problem. Obviously, a three-dimensional cloak would be required for any real implementation. For this research, however, only two-dimensional cylindrical cloaks are considered. This is due to the fact computer requirements for three-dimensional cloak simulations are rather extensive, whereas two-dimensional simulations are easily performed on a standard desktop computer. The work is likely extendable to the three-dimensional case, although there are definite issues which must be considered (Section 7.2). Additionally, a unique way to design metamaterials to increase their bandwidth is investigated.

There are two main thrusts of this research. First, a way to develop simplified material parameter sets for cylindrical cloaks is investigated. This is important because for the parameter set defined by Equation 1.23, at the location $r = a$, μ_r , ε_r , μ_z , and ε_z all equal zero while μ_θ and ε_θ are both infinite. These values are unattainable no matter how evolved metamaterial manufacturing capability becomes. There have been some generic simplified parameter sets published in the literature. These simplified parameter sets maintain some cloaking capability, but because their constitutive parameters are not ideal, cloaking functionality is degraded (Section 2.2). A method to define a simplified parameter set based on the existing metamaterial manufacturing capabilities has not been developed. Such a process would enable cylindrical cloak parameters to be defined in terms of what is achievable, thereby not putting limits or requirements on the manufacturing processes. As the ability to manufacture metamaterials continues to advance, material parameter sets with more difficult values will be able to be obtained.

The second thrust of this research involves increasing the effective bandwidth of cloaks. Note the ideal cylindrical cloak's material parameters shown in Equation 1.23 are independent of frequency. Hence, in theory the cloak is wide band and would be well suited for helping to reduce a pylon-target interaction. However, current research has shown passive metamaterials used to realize a cloak have a very narrow operational bandwidth (Chapter III). Therefore, a cloak constructed using these metamaterials would be operationally limited to a small range of frequencies. The narrowband nature of metamaterials does create a problem because RCS ranges operate over a significant bandwidth. A narrow band solution would not be of much use. This research investigates a unique way to increase the bandwidth of a metamaterial. Making the building blocks have a broadband response would result in the cloak being operational over a larger band of frequencies and would help make cloaks a more viable option for reducing RCS measurement error.

1.4 Dissertation Organization

This dissertation is organized as follows. Background information on cloaking theory, the cylindrical cloak, simplified cloaks, and alternatives to cloaking are covered in Chapter II. Chapter III examines fundamentals in metamaterials and how they are designed in order to create artificial magnetic and electric effects. Additionally, common methods used to measure the constitutive properties of metamaterials are explained. Chapter IV derives a new constraint equation on the material parameters for ideal cylindrical cloaks, which is then used as the foundation to develop simplified material parameter sets. Chapter V shows how a Green's function formulation can be used to decrease solution time for a cylindrically cloaked perfect electrically conducting (PEC) cylinder. Chapter VI investigates a method to design and possibly increase the bandwidth of metamaterials. Finally, in Chapter VII, conclusions for the research are summarized with recommendations for future research.

II. Cloaking Background

The transformation optics design approach discussed in Chapter I provides a recipe for various types of electromagnetic field control. This research focuses on electromagnetic cloaking, which was first put forth by Pendry *et al.* in 2006 [72]. Since the publication of this ground-breaking work, there have been numerous papers published analyzing the behavior of ideal cloaks using common electromagnetic analysis techniques. The relevant works are discussed below. As noted in Section 1.2.2, materials for an ideal cylindrical cloak do not exist, neither naturally nor can they be perfectly manufactured. This limitation necessitates simplified parameter sets. A number of simplified parameter sets for a two-dimensional cylindrical cloak have been developed. These are discussed in addition to their various short-comings. Finally, other cloaking options not based on transformation optics are briefly discussed and documented. The limitations associated with ideal cloaking that involve the design and manufacture of metamaterials will be discussed in Chapter III.

2.1 *Perfect Cloaking Theoretical Analysis*

Since Pendry *et al.*'s initial paper in 2006, there has been a significant effort confirming that perfect cloaking is theoretically possible, assuming the ideal constitutive parameters dictated by transformation optics could be achieved. Schurig *et al.* developed a method to perform ray-tracing within a cloak in order to confirm the cloak behaves as theoretically derived [81]. For spherical and cylindrical cloaks, they showed via ray-tracing the complex material acts as a perfect cloaking mechanism for the desired hidden region while resulting in no perturbation to the incident ray trajectory outside the cloaking body.

Leonhardt and Philbin demonstrated how transformation optics and the associated behavior of the electromagnetic fields can be described using the general theory of relativity [56]. They developed a formulation which takes a desired function, whether it be cloaking, perfect lenses, or the behavior of artificial black holes, and finds the properties of the material needed to generate the desired behavior. They showed the

behavior of electromagnetic fields in cloaks can be included and described within the framework of general relativity, which further solidified the validity of electromagnetic cloaking as described by transformation optics.

Chen *et al.* performed a full wave Mie scattering analysis on a spherical cloak [18]. They quantitatively solved for the scattered fields from an ideal spherical cloak and determined the scattering would be identically zero. When loss was introduced to the cloaking material, bistatic scattering resulted, with larger losses equating to larger scattered fields. However, the addition of loss did not affect the back-scattered field in that the monostatic return was still zero. This result is very different from that of regular particles and applies only to the spherical cloak. When introducing loss to the ideal parameters for a cylindrical cloak, the monostatic return is not identically zero.

Ruan *et al.* used cylindrical wave expansion to solve for the scattered field from an ideal cylindrical cloak. They also solved for the field transmitted into the hidden region. They confirmed by applying boundary conditions the ideal cloak is perfect by proving the coefficients for the scattered field from the cloak and the transmitted field into the hidden region were all zero [77]. This proved a cylindrical cloak with the ideal parameters shown in Equation 1.23 has no reflected field in addition to providing a hidden region ($r < a$ in Figure 1.4) which is completely shielded from electromagnetic energy.

Weder studied first-order and higher-order spherical cloaks. He proved for any frequency that ideal cloaks have no scattered field. Additionally, he showed that no incident energy can penetrate into a cloak's hidden region, and that if a source were placed in the hidden region, its energy would not leave the concealed area [98]. This makes sense because reciprocity holds for spherical cloaks since the permittivity and permeability tensors are symmetric [52].

Zhang *et al.* developed the equations to formulate the material parameters necessary to cloak an object in a slowly varying, multilayered, inhomogeneous envi-

ronment [106]. The work by Pendry *et al.* assumed a cloak immersed in homogeneous free space. Zhang *et al.*'s analysis is similar to the original work by Ward and Pendry. Their simulations showed successful cloaking of an object. The application for their work is cloaking objects in a layered media or at an interface between two media, such as a ship at sea or a building in the hot desert air.

A computer simulation of the perfect two-dimensional cylindrical cloak was done by Cummer *et al.* They performed a full-wave finite element method (FEM) simulation of the ideal two-dimensional cylindrical cloak using the Comsol Multiphysics FEM-based electromagnetics solver [28]. They simulated the two-dimensional cylindrical cloak for both lossless and lossy materials using a transverse magnetic (TM^z) incident wave (an electromagnetic wave with only a \hat{z} -component for the electric field vector). Their simulation results clearly showed the cloak operating as theoretically predicted with some degradation in performance when loss was introduced.

There are a number of papers which derive the theoretical equations for various cloaking geometries. Ma *et al.* [60] used the transformation optics algorithm described by Pendry *et al.* to derive the material parameter equations for an elliptical cylindrical cloak with similar results shown in [45]. Kwon and Werner did a similar analysis, but they considered an eccentric elliptic electromagnetic cloak [53]. Rahm *et al.* designed and simulated a square cloak and a cylindrical concentrator, which, instead of cloaking a certain region, focuses fields from one region into another [73]. Jiang *et al.* considered conformal, arbitrarily shaped cloaks [44]. These papers all performed simulations using the Comsol Multiphysics software package, and the results clearly showed the cloaks (or the concentrator) working as predicted by the original theory.

Zhao *et al.* performed a full-wave FDTD analysis of a two-dimensional cylindrical cloak. They used the Drude dispersion model to represent the permittivity and permeability of the cloak's material parameters. As with other simulations, they found a cloak with ideal parameters effectively hides an object placed within the cloaking shell from incident electromagnetic energy. Liang *et al.* also performed

FDTD simulations on a cylindrical cloak and found the cloak to work as expected. However they noted a strong forward scattering from the cloak during the dynamic processes when the incident waveform first strikes the cloak, an effect that can be controlled by varying the dispersive parameters in the Drude model [59].

These theoretical results support the original derivation that a cloak of a specific geometry with material parameters derived according to the transformation optics method put forth by Pendry *et al.* does indeed result in a perfectly cloaked region.

2.2 Simplified Cylindrical Cloaks

This section focuses solely on two-dimensional cylindrical cloaks. The units for this geometry in this work are (r, ϕ, z) , which is consistent with the work published by Schurig *et al.* [79]. The cylindrical cloak has a hidden region located at $r < a$, where a is the inner boundary. Objects placed in the hidden region are completely shielded from electromagnetic energy. The outer boundary of the cloak is located at $r = b$. Additionally, all analysis in this work assumes plane wave incidence. This geometry is shown in Figure 2.1.

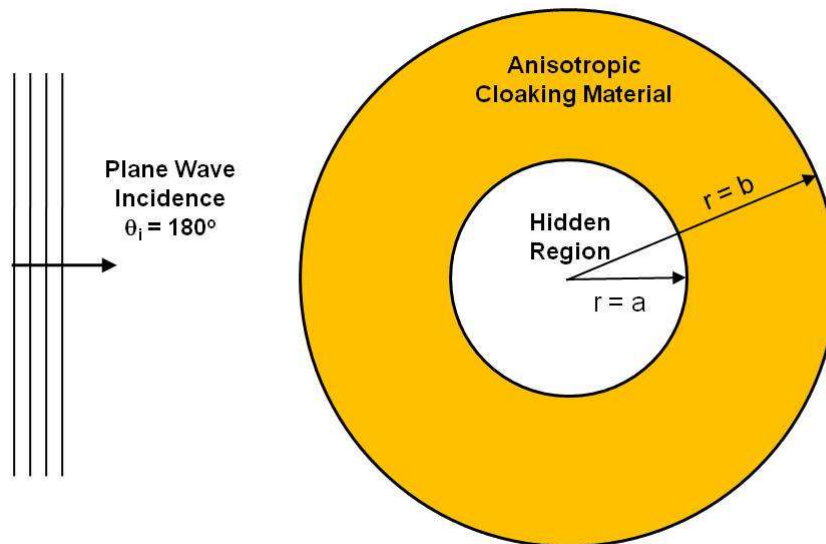


Figure 2.1: Two-dimensional cylindrical cloak geometry

When examining the material properties of a cylindrical cloak (Equation 1.23), it is obvious such a material would not likely occur naturally. First note the cloak is lossless. All materials have loss, and it is very difficult to manufacture magnetic materials with even small losses. Also, μ_r , ε_r , μ_z and ε_z all equal zero at $r = a$. Additionally μ_θ and ε_θ are each infinite at $r = a$. Thus, not only are these materials not naturally occurring, it is not currently possible to manufacture them, nor is it very likely technology would ever enable the manufacture of infinite values. Because of this, simplified parameter sets have been derived with the intent of creating manufacturable constitutive parameter values while limiting the reduction in cloak functionality as much as possible.

As a way to reduce the number of constitutive parameters required to realize a manufacturable cloak, the incident field can be decomposed into transverse electric (TE) and transverse magnetic (TM) field components. Thus, for TE^z fields only μ_z , ε_r , and ε_θ are required when analyzing field behavior. TM^z fields require ε_z , μ_r , and μ_θ .

The first sets of simplified material parameters for a cylindrical cloak were developed for specific incident field polarizations with the goal of satisfying the same governing wave equation within the simplified cloak that is satisfied in the ideal cloak [79]. For an assumed incident field type, Maxwell's equations can be used to define a wave equation that governs the field behavior within a given space. Assuming TM^z incidence, Maxwell's equations can be expressed as

$$E_z = \frac{1}{j\omega\varepsilon_z\varepsilon_0r} \left[\frac{\partial(rH_\theta)}{\partial r} - \frac{\partial H_r}{\partial \theta} \right], \quad (2.1)$$

$$H_r = -\frac{1}{j\omega\mu_r\mu_0r} \frac{\partial E_z}{\partial \theta}, \quad (2.2)$$

$$H_\theta = \frac{1}{j\omega\mu_\theta\mu_0} \frac{\partial E_z}{\partial r}, \quad (2.3)$$

where E_z is the \hat{z} -component of the electric field, H_r is the \hat{r} -component of the magnetic field, H_θ is the $\hat{\theta}$ -component of the magnetic field, r is the radial location,

ε_o and μ_o are the permittivity and permeability of free space, ε_z , μ_θ , and μ_r are the relative permittivity and permeability tensor values, and ω is the angular frequency of the incident electromagnetic field. The general wave equation governing the behavior of TM^z fields within a complex anisotropic material with spatially varying constitutive parameters can be developed by substituting Equations 2.2 and 2.3 into Equation 2.1.

$$E_z = \frac{1}{j\omega\varepsilon_z\varepsilon_or} \left[\frac{\partial}{\partial r} \left(\frac{r}{j\omega\mu_\theta\mu_o} \frac{\partial E_z}{\partial r} \right) - \frac{\partial}{\partial \theta} \left(-\frac{1}{j\omega\mu_r\mu_or} \frac{\partial E_z}{\partial \theta} \right) \right] \quad (2.4)$$

Note that j , ω , μ_o , and ε_o are all independent of r and θ . Therefore, they can be removed from the differentiation operations.

$$E_z = -\frac{1}{\omega^2\mu_o\varepsilon_o\varepsilon_zr} \left[\frac{\partial}{\partial r} \left(\frac{r}{\mu_\theta} \frac{\partial E_z}{\partial r} \right) + \frac{\partial}{\partial \theta} \left(\frac{1}{\mu_r r} \frac{\partial E_z}{\partial \theta} \right) \right] \quad (2.5)$$

Since r is not a function of θ , it can be removed from the $\frac{\partial}{\partial \theta}$ operation. Additionally, k_o is the free-space wave number defined as $k_o = \omega\sqrt{\mu_o\varepsilon_o}$. Therefore, Equation 2.5 can be rewritten as

$$\frac{1}{\varepsilon_z r} \left[\frac{\partial}{\partial r} \left(\frac{r}{\mu_\theta} \frac{\partial E_z}{\partial r} \right) \right] + \frac{1}{\varepsilon_z r^2} \frac{\partial}{\partial \theta} \left(\frac{1}{\mu_r} \frac{\partial E_z}{\partial \theta} \right) + k_o^2 E_z = 0. \quad (2.6)$$

Equation 2.6 is the general wave equation that describes the behavior of a TM^z electromagnetic field in a cylindrical anisotropic media. This equation will be used in the development of simplified constitutive parameter sets for cylindrical cloaks.

Schurig *et al.* were the first to derive a set of simplified material parameters for a two-dimensional cylindrical cloak [79]. However, when deriving the wave equation that governs the fields within the cloak, the procedure they used assumed a priori μ_θ was constant. Their intent was to eventually simplify μ_θ to a constant value, but doing so when developing the wave equation was mathematically incorrect [101, 102]. Because of this error, Schurig *et al.* simply removed μ_θ from the differentiation operation with respect to r in Equation 2.5. Thus, the following was thought to be

the wave equation for TM^z fields in a complex anisotropic medium.

$$\frac{1}{\varepsilon_z \mu_\theta} \frac{\partial^2 E_z}{\partial r^2} + \frac{1}{\varepsilon_z \mu_\theta} \frac{1}{r} \frac{\partial E_z}{\partial r} + \frac{1}{\varepsilon_z \mu_r} \frac{1}{r^2} \frac{\partial^2 E_z}{\partial \theta^2} + k_o^2 E_z = 0 \quad (2.7)$$

Note Equation 2.7 does not equal Equation 2.6 if μ_θ is r -dependent. Not realizing this, Schurig *et al.* then substituted the ideal cylindrical cloak's material parameters for a TM^z incident field into Equation 2.7. The following is the result.

$$\left(\frac{b-a}{b}\right)^2 \frac{\partial^2 E_z}{\partial r^2} + \left(\frac{b-a}{b}\right)^2 \frac{1}{r} \frac{\partial E_z}{\partial r} + \left(\frac{b-a}{b}\right)^2 \left(\frac{1}{r-a}\right)^2 \frac{\partial^2 E_z}{\partial \theta^2} + k_o^2 E_z = 0 \quad (2.8)$$

Schurig *et al.* believed Equation 2.8 was the correct wave equation for TM^z fields in an ideal cylindrical cloak. Their goal was to develop a simplified cylindrical cloak whose internal field behavior would match the field behavior in a cloak with ideal parameters. Therefore, they compared Equations 2.7 and 2.8 and concluded the following were the only material constraints on a simplified cylindrical cloak's material parameters for TM^z incident fields in order for the electric field to satisfy the same wave equation as that of an ideal cloak [79].

$$\frac{1}{\varepsilon_z \mu_\theta} = \left(\frac{b-a}{b}\right)^2 \quad (2.9)$$

$$\frac{1}{\varepsilon_z \mu_r} = \left(\frac{b-a}{b}\right)^2 \left(\frac{r}{r-a}\right)^2 \quad (2.10)$$

By examining Equations 2.9 and 2.10, Schurig *et al.* developed the following set of material parameters for a simplified cylindrical cloak.

$$\mu_r = \left(\frac{r-a}{r}\right)^2, \quad \mu_\theta = 1, \quad \varepsilon_z = \left(\frac{b}{b-a}\right)^2. \quad (2.11)$$

Note that μ_θ is indeed a constant like they assumed, but because this was assumed before all mathematical operations were completed, their results were not entirely correct. The material parameters shown in Equation 2.11 do satisfy Equations 2.9 and 2.10, and, as will be shown in Chapter IV, Equations 2.9 and 2.10 are some (but

not all) of the constraint equations on the material parameters for an ideal cylindrical cloak. Thus, the simplified parameters developed by Schurig *et al.*, though obtained using a method with a mathematical error, did show good results. Simulations showed a cloak with these simplified parameters maintained much of the power-flow bending and low-reflection characteristics of the ideal cloak [28].

These simplified parameters are not nearly as complex as the ideal material parameters from a manufacturing perspective, as ε_z is now position invariant. Additionally, Schurig *et al.* defined $\mu_\theta = 1$ because this is an easily obtainable value. The only spatially varying parameter is μ_r . No parameters are infinite and only $\mu_r = 0$ at $r = a$. However, in order to realize such a device, one further simplification had to be made. Note that μ_r is still spatially varying. Concentric, homogeneous layers with $\mu_r = \mu_n$ were used, where μ_n is a constant value for the n^{th} layer. A cloak with these simplified parameters was manufactured using metamaterials [79]. The results were not as good as the simulated values with varying μ_r , but they did show the ability to partially cloak an object.

The simplified parameter set shown in Equation 2.11 was used in the design and simulation of a cloak manufactured using metamaterials consisting of high permittivity ferroelectric rods. Gaillot *et al.* used metamaterial building blocks consisting of $\text{Ba}_x\text{Sr}_{1-x}\text{TiO}_3$ rods, and by adjusting the rod radii, they could control the resonant frequency. Much like Schurig *et al.*, Gaillot *et al.* created the radial variation in μ_r by creating layers of concentric rings. The difference is the operating frequency of their cloak was 0.58 THz compared to 8.5 GHz for the Schurig *et al.* cloak. Gaillot *et al.* also performed simulations using the commercial FEM software package, High Frequency Structure Simulator. Their work was unique because, unlike Cummer *et al.* in [28], Gaillot *et al.*'s simulated the individual building blocks of their cloak i.e. the metamaterial structures. Cummer *et al.* used continuous subdomains in their simulations. The results of Gaillot *et al.*'s work showed a simplified cloak with some of the ideal characteristics operating in the THz region [35].

The original simplified parameter set was used to develop a material parameter set for construction of a non-magnetic simplified cylindrical cloak for TE^z incident fields at optical frequencies [14]. A non-magnetic cloak was desired due to the difficulty in manufacturing materials with a magnetic response at optical wavelengths. Recall for TE^z incident fields, the constitutive parameters required are μ_z , ε_θ , and ε_r . Following a derivation process similar to that done by Schurig *et al.* and described above, the constraint equations for TE^z incident fields were thought to be

$$\frac{1}{\mu_z \varepsilon_\theta} = \left(\frac{b-a}{b} \right)^2, \quad (2.12)$$

$$\frac{1}{\mu_z \varepsilon_r} = \left(\frac{b-a}{b} \right)^2 \left(\frac{r}{r-a} \right)^2. \quad (2.13)$$

Using Equations 2.12 and 2.13 and the desire to limit the material parameters to non-magnetic effects, the following simplified material parameters were developed.

$$\mu_z = 1, \quad \varepsilon_\theta = \left(\frac{b}{b-a} \right)^2, \quad \varepsilon_r = \left(\frac{b}{b-a} \right)^2 \left(\frac{r-a}{r} \right)^2 \quad (2.14)$$

Much like the results in [28], simulations showed this simplified cloak maintains some of the characteristics of the ideal cloak [14].

There have been improvements to the original simplified parameters. An obvious shortcoming of the original simplified parameters is the large reflection at the cloak's outer boundary. The ideal cloak has an impedance matched to free space at $r = b$. The original simplified cloak does not, resulting in a significant reflection at the cloaking body and free space interface. To fix this problem, it was noted the transformation, denoted as $g(r')$, mapping the space $r' < b$ to the cylindrical shell $a < r < b$, can have multiple forms [15]. The linear transformation has the form

$$r = g(r') = \left(1 - \frac{a}{b} \right) r' + a, \quad (2.15)$$

while a quadratic transformation can have the form

$$r = g(r') = \left[1 - \frac{a}{b} + p(r' - b) + 1 \right] r' + a. \quad (2.16)$$

As before, a and b are the inner and outer radii of the cloak while p is a parameter which will be determined shortly. It can be shown using the procedure developed in [72] the material parameters for the ideal cylindrical cloak can be represented as

$$\varepsilon_r = \left(\frac{r'}{r} \right) \frac{\partial g(r')}{\partial r'}, \quad \varepsilon_\theta = \frac{1}{\varepsilon_r}, \quad \varepsilon_z = \left(\frac{r'}{r} \right) \left[\frac{\partial g(r')}{\partial r'} \right]^{-1}, \quad (2.17)$$

$$\mu_r = \left(\frac{r'}{r} \right) \frac{\partial g(r')}{\partial r'}, \quad \mu_\theta = \frac{1}{\mu_r}, \quad \mu_z = \left(\frac{r'}{r} \right) \left[\frac{\partial g(r')}{\partial r'} \right]^{-1}. \quad (2.18)$$

A reduced parameter set was desired for TM^z incident fields. When simplifying the ideal parameter set shown in Equations 2.17 and 2.18, the constraints defined by Equations 2.9 and 2.10 were used as the only limits on the material parameters. Hence, by setting $\varepsilon_z = 1$, the following define a set simplified parameters.

$$\mu_r = \left(\frac{r'}{r} \right)^2, \quad \mu_\theta = \left[\frac{\partial g(r')}{\partial r'} \right]^{-2}, \quad \varepsilon_z = 1. \quad (2.19)$$

To match the impedance to free space at $r = b$, the following constraint was applied.

$$Z|_{r=b} = \sqrt{\frac{\mu_\theta}{\varepsilon_z}} = \frac{\partial g(r')}{\partial r'} \Big|_{r=b} = 1 \quad (2.20)$$

Using the condition imposed in Equation 2.20, the variable p in Equation 2.16 is found to be $p = \frac{a}{b^2}$. For $g(r')$ equal to that shown in Equation 2.16 with $p = \frac{a}{b^2}$, the parameter set is called a quadratic cloak [15]. The quadratic cloak satisfies the material constraints shown in Equations 2.9 and 2.10 and has a matched impedance at $r = b$. A limit on the quadratic cloak is the value $\frac{a}{b} < 0.5$ to ensure a monotonic transformation [15]; however, its performance in terms of reducing the scattering width of a PEC cylinder was better than that of the cloak with the original simplified parameters.

A second set of material parameters with a matched impedance at $r = b$ that satisfies equations (2.9) and (2.10) was developed [102]. These are shown below.

$$\mu_r = \left(\frac{r-a}{r}\right)^2 \frac{b}{b-a}, \quad \mu_\theta = \frac{b}{b-a}, \quad \varepsilon_z = \frac{b}{b-a}. \quad (2.21)$$

To the author's knowledge, the parameter set in Equation 2.21 was not derived from a governing equation. Rather, the values seem to have been found by simply using Equations 2.9 and 2.10 and determining values which satisfy these constraints while also having a matched impedance at $r = b$. For this work, the cloak with parameters shown in Equation 2.21 will be called the improved cloak. The performance in terms of reducing the scattering width of a cloaked PEC cylinder by the improved cloak and the quadratic cloak are similar for certain values of a and b . However, it has been shown the improved cloak has a more consistent performance as the ratio of $\frac{a}{b}$ varies [102]. Additionally, the improved cloak has only one spatially varying material parameter while the quadratic cloak has two, making the improved cloaks parameters easier to manufacture than those of the quadratic cloak.

2.3 Cloaking Limitations

As stated in the previous section, the ideal cylindrical cloak has constitutive parameters equal to zero or infinity, values which are not possible to obtain and are the motivation to develop simplified parameter sets. It is obvious since the ideal parameter values won't be obtained, there will be a reduction in cloak performance. Isić *et al.* analyzed cloak performance based on the inability to precisely manufacture the ideal cloak's constitutive parameters [43]. Note for the ideal cloak, $\mu_r = 0$ at the inner boundary, $r = a$. This also means $\mu_\theta \rightarrow \infty$ at the outer boundary, $r = b$. It is not possible to achieve these values. For their analysis, Isić *et al.* let the parameters for a TM^z incident wave be

$$\mu_r = \frac{r - \frac{b(a-r_1)}{b-r_1}}{r} \quad (2.22)$$

$$\mu_\theta = \frac{r}{r - \frac{b(a-r_1)}{b-r_1}} \quad (2.23)$$

$$\varepsilon_z = \frac{r - \frac{b(a-r_1)}{b-r_1}}{r} \left(\frac{b-a}{b-r_1} \right)^2 \quad (2.24)$$

The parameter, r_1 , is a measure of the imperfectness of a cloak. An ideal cloak has $r_1 = 0$. At this value Equations 2.22 - 2.24 simplify to the ideal parameters. Defining

$$\delta\mu_r = \mu_r(r = a) - \mu_{r_{ideal}}(r = a) \quad (2.25)$$

and since $\mu_{r_{ideal}}(r = a) = 0$, they solve for r_1 to be

$$r_1 = \frac{ab\delta\mu_r}{b - a(1 - \delta\mu_r)}. \quad (2.26)$$

For a TM^z plane wave incident on the imperfect cloak, and with a PEC cylinder placed in the hidden region, they solved boundary conditions and found the coefficients for the scattered field. For small r_1 , the dominant scattering term is the zeroth order mode, which matches the results of Ruan *et al.*. Isić *et al.* defined q as the ratio of the scattering width of an uncloaked PEC cylinder to that of a cloaked PEC cylinder and find that

$$q \cong \frac{2.29 \ln^2(k_o r_1)}{\pi \lambda_o}. \quad (2.27)$$

If one-order of magnitude scattering width reduction is desired, $q = 10$. The parameters r_1 and $\delta\mu_r$ can be found using Equations 2.26 and 2.27. For $q = 10$, $\lambda_o = 0.25$ m, $a = \lambda_o$, and $b = 2\lambda_o$, they found that $\delta\mu_r \cong 0.01$. This means in order to reduce the scattering width by 10 dB using a cylindrical cloak, the constitutive parameter, $\mu_r = 0.01$ at $r = a$ [43]. Such manufacturing control is possible, but anything more is approaching the current technological limit. In [42], Isić *et al.* provide a more mathematically rigorous derivation of the scattering from imperfect cloaks. They conclude that a PEC object placed in the hidden region of an imperfect cloak has a reduction in its echo width by a factor of $\frac{a}{r_1}$ [42]. They consider one order of magnitude reduction an optimistic result.

Ruan *et al.* performed a similar analysis and examined the effects of a slight perturbation in the location of the cloak's inner boundary. They found even small perturbations result in scattering from the cloaking body. A perturbation takes the form of the inner cloak boundary being located at a distance $r = a + \delta$ instead of the ideal location $r = a$. Even for very small δ , such as $\delta = 10^{-5}a$, there is a noticeable scattered field [77]. The size of the scattered field is dependent on the cloak geometry. As an example, consider a cloak with boundaries $a = \lambda$ and $b = 2a$. A \hat{z} -directed incident and scattered electric field can be represented using cylindrical wave expansion as [13]

$$E_z^i = E_o \sum_{-\infty}^{\infty} a_n J_n(kr) e^{jn\phi}, \quad (2.28)$$

$$E_z^s = E_o \sum_{-\infty}^{\infty} c_n H_n^{(2)}(kr) e^{jn\phi}, \quad (2.29)$$

where E_o is a constant value. The scattering coefficient for each order can be defined as

$$\alpha_n^s = \frac{c_n}{a_n}. \quad (2.30)$$

For $\delta = 10^{-5}a$, $|\alpha_0^s| = 0.175$. For orders where $n \neq 0$, $|\alpha_n^s| < 10^{-9}$, meaning the zeroth order is the dominant scattering term. Additionally, it was shown as $\delta \rightarrow 0$, convergence of $|\alpha_0^s|$ is slow [77].

In addition to having constitutive parameters which are unattainable, perfect cloaks also have a bandwidth issue. Yao *et al.* investigated whether or not the material making up an electromagnetic cloak could be frequency invariant [104]. They concluded that, due to causality, the cloak must be dispersive. A nondispersive cloak results in group velocities greater than the speed of light. Additionally, they found there must be a strong absorption at the cloak's frequency of operation. This results in a significant forward shadow. They did conclude the cloak is an effective instrument to reduce backscatter but only for a narrow bandwidth.

Chen *et al.* had similar conclusions regarding the bandwidth as a result of the limit imposed on group velocities [20]. They considered a more generic form of the cylindrical transformation such that they are mapping the region $r_o \leq r \leq b$ to $a \leq r \leq b$. In the example in Section 1.2.1, $r_o = 0$. Chen *et al.* showed perfect cloaking is possible only at one single frequency. If more than one frequency is considered, the group velocities exceed the speed of light. Therefore, they considered a cloak such that r_o is now a function of frequency, $r_o(\omega)$. Note $r_o(\omega)$ can be zero at one particular frequency and also have small, but non-zero values throughout a nearby bandwidth. They simulated a cloak with the following material parameters.

$$\mu_r = \left(\frac{r-a}{r}\right)^2, \quad \mu_\theta = 1, \quad \varepsilon_z = \left(\frac{b-r_o(\omega)}{b-a}\right)^2. \quad (2.31)$$

They show the bandwidth limitation for this material parameter set to be

$$\frac{\Delta\omega}{\omega} \leq \frac{\Delta r_o}{a}. \quad (2.32)$$

They simulated their designed cloak and found it to have an operational bandwidth from 8.5 - 8.75 GHz, with the cross section of a PEC cylinder being 30% compared to that of an uncloaked cylinder.

As a way to increase the operational bandwidth of a cylindrical cloak, Wang *et al.* proposed creating a cylindrical cloak out of active metamaterials [96]. They designed a simplified cylindrical cloak with material parameters shown in Equation 2.14 and repeated below for convenience.

$$\mu_z = 1, \quad \varepsilon_\theta = \left(\frac{b}{b-a}\right)^2, \quad \varepsilon_r = \left(\frac{b}{b-a}\right)^2 \left(\frac{r-a}{r}\right)^2. \quad (2.33)$$

Note for their effort, they assumed a TE^z incident waveform. For their cloak implementation, they proposed to use active metamaterials. Passive metamaterials are dispersive (to be discussed in Chapter III) i.e. their constitutive parameters vary as a function of frequency. For the geometry of their cloak and assumed incident field

type, the μ_z and ε_θ values will be determined by the substrate used in the metamaterial manufacture, and the substrate is not dispersive in the desired frequency range. However, ε_r is determined by the configuration of the metallic structures within the metamaterial and is highly dispersive. In order to allow a band of operating frequencies, Wang *et al.* proposed using a variable capacitor mounted between metal strips. The capacitance between the metal strips helps control ε_r . A DC bias can be used to change the capacitance on the variable capacitor. As frequency is changed, the capacitance is changed in order to keep the ε_r at the required value dictated by Equation 2.33. Wang *et al.* did not build any devices, but their numeric simulations showed their concept is valid. The instantaneous bandwidth of the cloak was not increased, but it was able to operate over a wider bandwidth.

The final work discussed in this section is not really a short-coming of cloaks, but rather a unique way in which the cloaking capability can be turned off. Chen *et al.* used the transformation optics approach to develop a material that when placed in the hidden region of an ideal cylindrical cloak results in the object within the hidden region being seen by incident radiation. A PEC cylinder was placed in the hidden region of an ideal cloak and was coated with a specific anisotropic material with a negative refractive index. Chen *et al.* termed this material the anti-cloak. The anti-cloak effectively annihilates the functionality of the ideal cloak and shifts the hidden region out to the cloak's boundary thereby making it visible. They proved the existence of scattered fields by matching boundary conditions [21].

2.4 *Alternate Cloaking Methods*

This section is by no means a complete listing of the additional work going on with regards to cloaking, but it does provide a general summary of additional work being done in this field.

The work done by Huang *et al.* is cloaking as described by transformation optics. However, to implement the cloak, they did not use anisotropic materials. Rather, they assumed a TE^z incident wave and simulated a two-dimensional cylindrical cloak

realized using homogeneous isotropic materials. They did this by using the fact a layered structure of homogeneous isotropic material can be treated as a single anisotropic medium provided the layers are small compared to wavelength [40]. For a given set of two layers of material that are sufficiently thin, the effective permittivities are [100]

$$\varepsilon_\theta = \frac{\varepsilon_1 + \eta\varepsilon_2}{1 + \eta}, \quad (2.34)$$

$$\frac{1}{\varepsilon_r} = \frac{1}{1 + \eta} \left(\frac{1}{\varepsilon_1} + \frac{\eta}{\varepsilon_2} \right), \quad (2.35)$$

where $\eta = \frac{d_2}{d_1}$ and d_i are the thicknesses of the two layers. Huang *et al.* used Equations 2.34 and 2.35 to derive the appropriate material parameters and thicknesses for a cylindrical cloak with parameters defined by Equation 2.33. They approximated the radial variation in ε_r using ten anisotropic layers, resulting in their isotropic, homogeneous cloak having twenty layers. Their results showed good cloaking performance with a 12 dB reduction in forward scattering when comparing a cloaked to an un-cloaked PEC cylinder. There was a reduced scattering for all observation angles, but the reduction was on the order of 3-4 dB. Since Huang's method uses homogeneous materials in their implementation, the bandwidth problem inherent with metamaterials (see Chapter III) is somewhat avoided. However, extreme parameter values would still be required to manufacture such a cloak, and homogeneous materials with these extreme values over significant bandwidths do not exist.

Alù and Engheta have investigated an alternative method to hide objects [8, 9]. Their method uses plasmonic and metamaterial coatings to reduce the scattering from an object. There are electrical size limitations, but the advantage of their method is the material coatings are homogeneous and isotropic. A disadvantage is the plasmonic coating is dependent on the shape and material properties of the object to be hidden.

Miller [65] proposed a method to cloak a region of space that uses sensors and active surface sources. Passive sensors are used at the boundary of the region to be cloaked. The incident radiation is sensed, and the type of surface sources to be placed

which generate the appropriate signals which make the region appear transparent to the incident field to an outside observer can be mathematically determined. The method has the advantage of being broadband. The disadvantage is actual implementation for broad-band electromagnetic waves is difficult due to the speed of propagation. Zambonelli and Mamei proposed something similar by suggesting cloaking can be achieved by real-time scene manipulation. Active sensor networks embedded in “garments” (cloaks) could sense the incident electromagnetic energy and then radiate the appropriate response to make the cloak invisible [105]. This work was a theoretical speculation as to what might be possible in the future as active sensor technology evolves.

Kildal *et al.* performed an interesting comparison between the cloaking method described in [72] and the efficacy of scattering reduction when using geometric shaping with hard and soft surfaces. Specifically, they compared the theoretical and realizable performances of cloaking a PEC cylinder of radius $2a$ using a cloak made of metamaterials and a shaped geometry with a hard surface. The shaped geometry with hard surface is limited by the fact the incident angle of the electromagnetic radiation must be known, whereas a metamaterial cloak theoretically works independent of angle. However, they state this appears to be the only area where the metamaterial cloak is better suited, and they are quick to point out a combined TE/TM realization of a shaped geometry with a hard surface is realizable and performs as well as individual TE or TM structures. Due to the complex anisotropy of the materials required to implement the metamaterial cloak, only a TM realization has been physically realized. Additionally the metamaterial cloak has an extremely narrow bandwidth, whereas the shaped geometry with hard surface have approximately a 20% operational bandwidth. They conclude Pendry *et al.*'s cloaking method, while exotic, does not compare to current technology of shaping and RAM [47].

2.5 *Summary*

This chapter presented background analysis showing cloaking as derived from transformation optics is theoretically possible, although bandwidth will be limited due to constraints imposed by causality requirements. Additionally, due to singularities in the required material parameters for a two-dimensional cylindrical cloak, and also due to the manufacturing constraints, reduced parameter sets were developed. The reduced parameter sets will be further discussed in Chapter IV. Alternate cloaking methods were discussed, and the work done by Huang *et al.* will be used in Chapter V.

III. Metamaterials Background

The intent of this chapter is not to define or categorize metamaterials. This is already an extensive effort, and even the mere definition of metamaterial evokes much discussion [84]. In this effort, metamaterials will be defined as they were in the work by Lapine and Tretyakov [54]:

(A) metamaterial is an arrangement of artificial structural elements designed to achieve advantageous and unusual properties.

No specific requirements regarding the material's resulting constitutive parameters are stated, nor does this limit previously "named" materials from being included in this definition. Examples of these older materials are chiral materials, artificial dielectrics, and artificial magnetics [107]. Newer media that have recently been developed are Veselago media, which are also known as double-negative (DNG) media. In a Veselago medium, both the effective permeability and permittivity are less than zero. Additionally, there are materials where only the permittivity or permeability is less than zero. These are referred to as epsilon-negative and mu-negative materials respectively [30]. Note that nowhere in this research are materials with negative permeability or permittivity required. It must also be stressed there is considerable debate as to the validity of the experimental results proving the existence of DNG materials [66]; however, the substance of that debate is outside the scope of this effort.

As stated in Section 1.2.2, metamaterials are man-made materials with sub-wavelength, often periodic structures. The structures are usually metallic. The geometry and periodicity of the structure enables one to create a material with desired effective permittivity and permeability values that are either isotropic or anisotropic. This is advantageous because, as discussed in Chapter II, cloaks require materials with specific anisotropic constitutive parameters. Precise control of the material parameters is required during manufacturing because deviations from the specified values result in degraded performance [42, 101]. Therefore, metamaterials are the ideal building blocks for not only cloaks, but for any material design created using the transformation optics approach.

Metamaterials are typically periodic lattices of unit cells. Within each unit cell is some type of metallic inclusion whose shape determines the type of bulk effect desired. In order to realize bulk effective material parameters, the size of a unit cell, a (also known as the lattice constant), is much smaller than the operating wavelength. There has not been a theoretically determined limit for a such that if the limit is passed, the material immediately stops exhibiting bulk constitutive parameters. However, the rule of thumb appears to be [86]

$$0.01 < \frac{a}{\lambda} < 0.2. \quad (3.1)$$

This research focuses on metamaterials operating in the 10 GHz region. At 10 GHz, the wavelength is three centimeters. Therefore, metamaterial lattice constants will be no larger than six millimeters. This rule of thumb is crucially important if one is to properly use Maxwell's equations in their macroscopic form to analyze metamaterials.

A short-coming of metamaterials is they are dispersive. This means their constitutive parameters vary as a function of frequency. The dispersiveness can be mathematically represented using the following general formulas [30]:

$$\varepsilon(\omega) = \varepsilon_o \left(1 - \frac{\omega_{pe}^2}{\omega^2 - j\Gamma_e\omega} \right), \quad (3.2)$$

$$\mu(\omega) = \mu_o \left(1 - \frac{\omega_{pm}^2}{\omega^2 - j\Gamma_m\omega} \right), \quad (3.3)$$

where ω_{pe} is the electric plasma frequency and ω_{pm} is the magnetic plasma frequency which can be controlled by varying the properties of the unit cell. Γ_e and Γ_m are damping terms associated with losses in the materials.

What follows in the subsequent sections is a discussion of some of the more common metamaterial structures that are used to artificially create effective electric and magnetic mediums. Note most of the recent work with metamaterials has been designing and manufacturing materials that will exhibit negative refraction. As stated above, negative refraction will not be required for this effort, nor does this effort intend

to debate the existence of DNG materials. However, the structures used to create the desired constitutive parameters will be useful. This discussion is by no means comprehensive, and is intended to give an overview of how metamaterials realize the desired properties.

3.1 Creating Effective Permittivity

The first work in creating artificial permittivities to result in an electromagnetic effect was done by Kock in 1946. He used conducting plates of a certain shape and prescribed spacing to create a microwave lens [50]. An electromagnetic field incident upon such a structure will undergo a focusing effect, much the same way light does when refracted by an optical dielectric lens. In essence, the geometry of the conducting plates created a bulk permittivity as seen by incident electromagnetic energy. Similarly, Kock used conducting paint on cellophane globes to create a bulk permittivity effect which helped to reduce the weight of standard dielectric lenses [51].

Since the initial work by Kock, there have been a great number of contributors to the field of artificial dielectrics. Much effort was done in the 1950's and 1960's to produce artificial dielectrics for use with radar. It is now widely known lattice structures of metallic spheres, disks, or rods can create a medium with an effective permittivity. Depending on the spacing between the lattice objects, and the polarization and frequency of the electromagnetic field, the permittivity varies [23]. Rotman showed how a periodic lattice of metallic rods can be used to simulate the behavior of a plasma. Plasmas have a negative permittivity while their relative permeability is unity. The rodded artificial dielectric in [76] effectively simulated a plasma.

Pendry *et al.* used a similar structure of thin wires to create an effective negative permittivity in the gigahertz range. Prior to their work, the electric plasma frequency (Equation 3.2) was typically confined to the optical frequencies. They achieved the frequency reduction by emphasizing the requirement for very thin wires, which reduces the electron density thereby lowering the plasma frequency. Results were obtained using numerical simulations which confirmed the theoretical derivations [71]. Pendry

et al. extended their results in [69] by creating an array of gold-plated tungsten wires with a diameter of $20 \mu\text{m}$. The spacing (lattice constant) between the wires was 5 mm. As mentioned in Section 2.2, Gaillot *et al* used arrays of gold-plated tungsten rods to create the desired radial permittivity variation in a simulation of a simplified cylindrical cloak [35].

An alternate way to create an artificial permittivity is to use an electric-inductive-capacitive (ELC) resonator. An ELC resonator was created because researchers found fabrication of a three dimensional wire array was difficult, and also that extremely thin wires have too high of losses [80]. An ELC resonator has a unit cell structure shown in Figure 3.1.

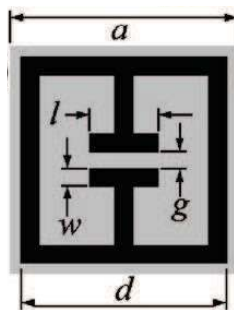


Figure 3.1: ELC Resonator [80]

The ELC resonator operates as follows. For the field configuration shown in Figure 3.2, the current flow is due solely to electric field coupling. There is no magnetic field coupling because the magnetic field is in the same plane as the device. Charge builds up on the center T's which creates a capacitance. The outer loops act as two oppositely wound inductors. This structure acts as an equivalent circuit where a capacitor is in parallel with two inductors (Figure 3.2, lower right). For this particular field configuration, the capacitive element couples to the incident electric field and gives the metamaterial the artificial permittivity. When the magnetic field is perpendicular to the plane of the device, as shown in Figure 3.3, the currents in the loops cancel, resulting in no magnetic moment. There is no coupling to the electric field because there is not a significant capacitance which allows current to flow. Controlling

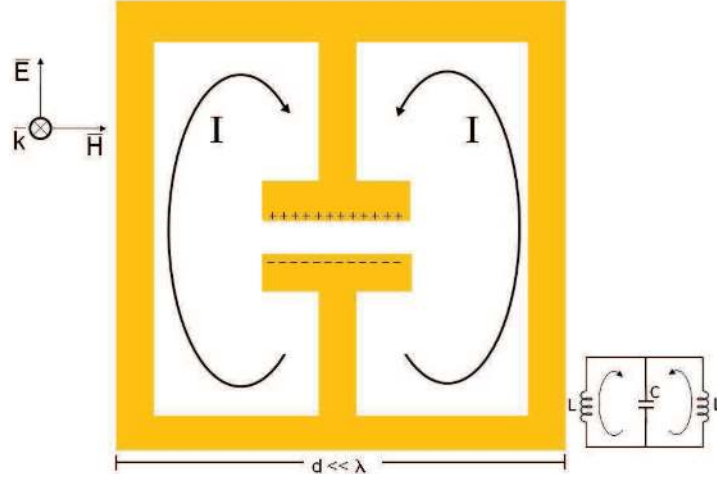


Figure 3.2: ELC Electric Field Coupling

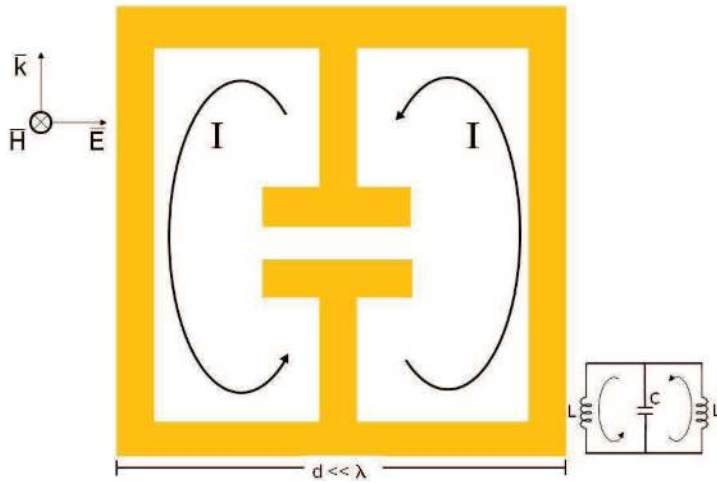


Figure 3.3: ELC Operation with No Magnetic Field Coupling

the capacitance and the inductance is done by varying the parameters a , d , l , w , and g shown in Figure 3.1. These parameters determine the resonant frequency of the device. Schurig *et al.* obtained simulated S-parameter measurements on an ELC array using Microwave Design Studio, an electromagnetics simulation software package based on a finite integral time domain formulation. They also built a single-layered array of structures and obtained excellent agreement between extracted parameters (see Section 3.3) from simulated and experimentally obtained measurements.

3.2 Creating Effective Permeability

There was a significant push in the late 1990's to create magnetic effects from non-magnetic materials due to the quest to create DNG media. A variety of structures has been analyzed which generate magnetic responses. The following subsections discuss these structures. The primary focus of the research has been manufacturing a DNG medium. However, these various structures are beneficial because they enable the ability to create metamaterials with a specified permeability at a desired frequency. The different designs each have their own positive and negative aspects.

3.2.1 Edge Coupled Split Ring Resonator. Pendry *et al.* developed what is commonly called the edge coupled split ring resonator (EC-SRR). The basic building block for the EC-SRR is the split ring structure shown in Figure 3.4. The gold structures in the figure are thin layers of metal mounted on a substrate. The device is excited by a plane wave propagating in the plane of the device with the magnetic field normal to the plane of the rings. Since the magnetic flux is perpendicular to the

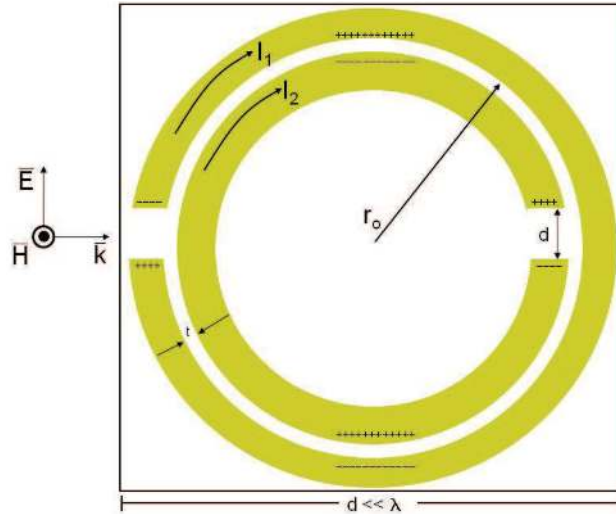


Figure 3.4: Edge Coupled Split Ring Resonator

plane of the rings, an electromotive force results causing current to flow. In general,

the electromotive force is [74]

$$EMF = \oint \vec{E} \cdot d\vec{l} = -j\omega \int_S \vec{B} \cdot d\vec{S}. \quad (3.4)$$

The average radius of the two rings is r_0 . Thus, $EMF \cong -j\omega\pi r_0^2 B_z$ [62]. The flowing current in the inner and outer rings creates the magnetic moment, resulting in an artificial permeability. Current flow is possible due to the capacitance in the ring gaps (t and d in Figure 3.4). A stronger capacitance will result in more current flowing because capacitance, charge, and voltage are related by [74]

$$C = \frac{Q}{V}. \quad (3.5)$$

Current flowing in the outer and inner loops results in the device having an inductance which is related to the radius of the rings. The capacitance and inductance results in the device having a resonant frequency of $\frac{1}{\sqrt{LC}}$. Detailed analytic derivations for C and L are provided in [78].

Typically, an EC-SRR is called an SRR. Such a configuration of an EC-SRR results in a material with an effective permeability described by Equation 3.3, where, for this geometry, ω_{pm} and Γ_m are controlled by the various dimensions of the geometry within the unit cell in addition to the lattice spacing [70]. Aydin *et al.* showed using simulations and experimentally that increasing both d and t shifts the resonant frequency higher due to the reduced capacitance [12]. An array of SRRs as shown in Figure 3.4 in combination with an array of metallic wires was used to create the first composite DNG medium [88] (although as stated earlier, there is some debating the meaning of these results).

3.2.2 Omega Split Ring Resonator. Another geometry used to create magnetic effects is the Ω ring. However, unlike the EC-SRR, which has no electric effects without being used in conjunction with a rod lattice, the Ω ring couples to the electric and magnetic fields. A typical Ω ring geometry is shown in Figure 3.5. Currents are

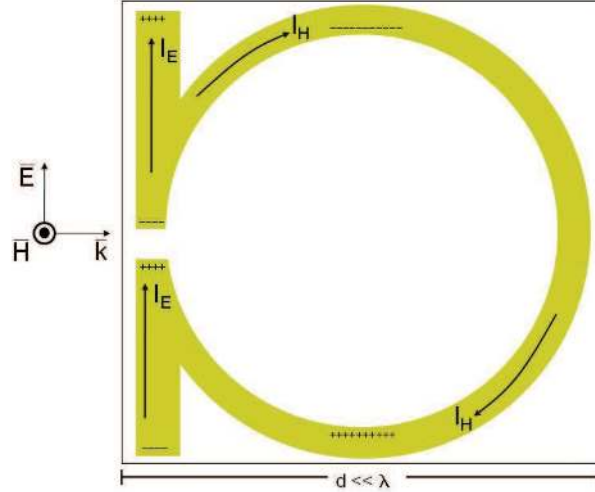


Figure 3.5: Ω -Ring Geometry

excited in the rod-portion of the Ω ring due to the incident electric field. Charge builds up in the gap and the rod ends, resulting electric moments which creates the artificial permittivity. The magnetic field is normal to the plane of the device. This excites a current, which flows in the ring portion of the geometry, creating the magnetic moments resulting in an artificial permeability. An array of Ω rings is bianisotropic. This is because the charge build up in the rings resulting from the current induced by the magnetic field results in a series of electric dipoles. Simovski and He showed that two Ω geometries printed in opposite directions on opposing sides of a dielectric do not have any magnetoelectric [85]. The opposing direction of current flow in the rings results in the electric dipoles induced by the magnetic field cancelling. Note the original EC-SRR developed by Pendry *et al.* was also shown to have bianisotropic effects [62], although these effects can be minimized by varying the EC-SRR orientation throughout a lattice. Huangfu *et al.* used an Ω -like structure to build a DNG medium whose effects manifested from 12-13 GHz. Only a periodic structure consisting of elements shown in Figure 3.5 were required. They did not have to include a lattice of thin metallic wires to generate the negative permittivity. This is because the rods connecting the Ω structures serve this function. Huangfu *et al.*'s results showed

more bandwidth where the DNG effect took place [41], and they also reported smaller losses than those experiments which used ring geometries.

3.2.3 Additional Structures. O'Brien and Pendry developed what is now called an axially symmetric ring. The geometry is very similar to the EC-SRR in the previous subsection except instead of rings, rectangular structures are used. This is shown in Figure 3.6. The advantage of this type of geometry is the structure is more

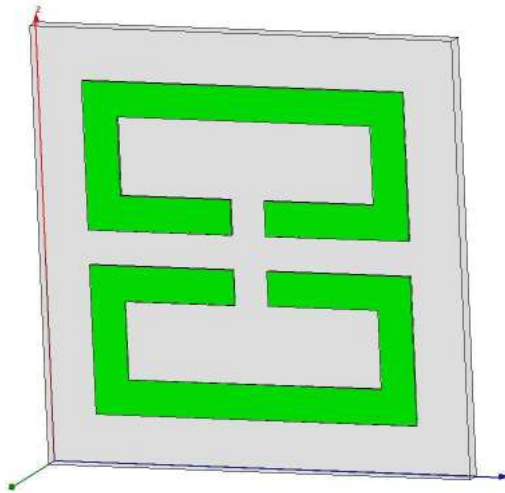


Figure 3.6: Axially Symmetric Ring

conducive to manufacturing at the sub-micron wavelengths [68]. These smaller structures would enable the desired effects to manifest at optical frequencies provided the metal maintains its good conductor properties at these higher frequencies. O'Brien and Pendry used a such a structure in conjunction with a lattice of thin metallic wires to create a DNG medium operational at 76 THz. There are also results presented in [30] where a negative permeability was demonstrated using an array of axially symmetric SRRs between 8.2 and 8.7 GHz.

An additional metamaterial structure is called the S-ring. Its geometry is shown in Figure 3.7. Much like the Ω -ring, the S-ring geometry does not require the use of metallic rods to generate an electric effect. Chen *et al.* designed and fabricated a DNG metamaterial using the S-ring structures, with an operational frequency of 10.9 - 13.5

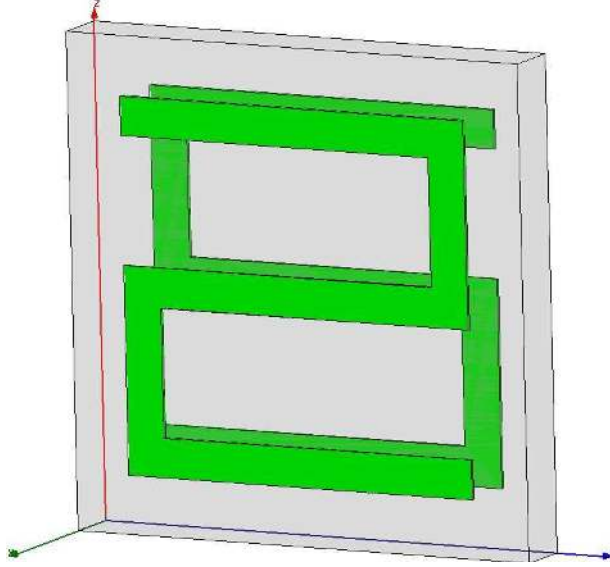


Figure 3.7: S-Ring Geometry

GHz, which is a significant increase in bandwidth compared to early implementations [17]. They performed a detailed theoretical analysis and develop the theory which governs the effective constitutive parameters of an S-ring metamaterial [16].

There are other types of structures that can be used. In fact, when Schurig *et al.* manufactured the first simplified cylindrical cloak, the unit cells contained aspects of the axially symmetric SRR in addition to the ELC-resonator. A picture of the basic geometry of the unit cell is shown in Figure 3.8. Changing various dimensions of the cell (l , s , w , and r) alters the cell capacitance and inductance, thereby creating the desired permittivity and permeability specified by the simplified cloak's material parameters.

Obviously, there are limitless types of geometries which could be used to create artificial electric and magnetic effects. However, in order avoid simply trial and error, one must understand how the fields interact with the devices.

3.3 Measuring Metamaterial Constitutive Parameters

As stated in the previous sections, there has been much work developing periodic lattices of unit cells which exhibit artificial permittivity and permeability. This

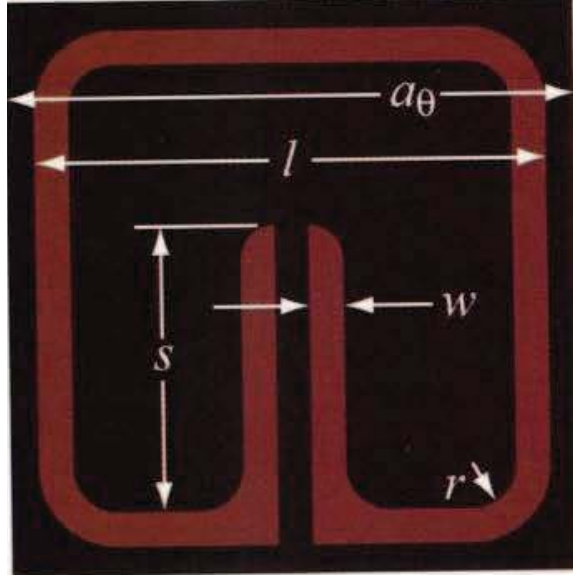


Figure 3.8: Unit Cell Geometry for Simplified Cloak Construction [79]

has led to a good understanding of how to create bulk artificial electromagnetic effects using metamaterials. For most experiments, the proof the metamaterial was exhibiting DNG behavior was obtained by empirically measuring the refracted angle of incident energy at various frequencies. If this angle was negative, it was concluded the material had a negative index of refraction and therefore simultaneously negative permittivity and permeability. This can be considered an indirect measurement of the constitutive parameters because the materials themselves were not explicitly measured. Therefore, direct methods to measure the permittivity and permeability have been developed. There has been much discussion during the past decade whether standard material parameter retrieval algorithms can be used when characterizing metamaterials. In the following sections, a standard material retrieval algorithm is presented followed by various analyses done on metamaterial characterization using this algorithm. Limitations of the retrieval algorithm are discussed with possible alternative measurement techniques documented.

3.3.1 Nicolson-Ross-Weir Algorithm. A common method to extract permittivity and permeability from a homogeneous material slab is to obtain S-parameter

measurements and then use the Nicolson-Ross-Weir (NRW) algorithm to extract the constitutive parameters [67, 99]. The NRW algorithm is derived as follows. From a sample of an infinite length of planar material, it can be shown that

$$S_{11} = \frac{R[1 - P^2]}{1 - R^2P^2}, \quad (3.6)$$

$$S_{21} = \frac{P[1 - R^2]}{1 - R^2P^2}, \quad (3.7)$$

where $P = e^{-jkd}$ and is called the phase delay, k is the wave number in the slab of material, and d is the material slab thickness [39]. The reflection coefficient, R , from an infinite slab of planar material in free space is

$$R = \frac{Z - Z_o}{Z + Z_o}, \quad (3.8)$$

where Z and Z_o are the intrinsic impedance of the material and free space respectively and $Z = \sqrt{\mu/\epsilon}$ [13]. It has been assumed a transverse electromagnetic wave propagating in its fundamental mode will be used to interrogate the material. Note also that $k = \omega\sqrt{\mu\epsilon} = \omega\sqrt{\mu_o\epsilon_o\mu_r\epsilon_r} = \frac{\omega}{c}\sqrt{\mu_r\epsilon_r}$ where c is the free space speed of light. Thus, by finding R and P , one can use their respective definitions to find μ_r and ϵ_r .

First, one must find expressions for R and P using only the S-parameters. It is possible to solve Equations 3.6 and 3.7 for P [39].

$$P = \frac{S_{21}}{1 - RS_{11}} \quad (3.9)$$

Equation 3.9 can be used to write a quadratic expression for R .

$$R^2 - 2QR + 1 = 0 \quad (3.10)$$

where

$$Q = \frac{S_{11}^2 - S_{21}^2 + 1}{2S_{11}^2} \quad (3.11)$$

Therefore R is found to have two solutions.

$$R_{1,2} = Q \pm \sqrt{Q^2 - 1}, \quad (3.12)$$

The sign choice is made such that $|R| < 1$ [67]. Note R is now expressed simply in terms of the S_{11} and S_{21} measurements. Once R is found, P can be found using Equation 3.9 [39].

Equation 3.8 can be expanded using the definition of Z .

$$R = \frac{\sqrt{\frac{\mu_r \mu_o}{\varepsilon_r \varepsilon_o}} - \sqrt{\frac{\mu_o}{\varepsilon_o}}}{\sqrt{\frac{\mu_r \mu_o}{\varepsilon_r \varepsilon_o}} + \sqrt{\frac{\mu_o}{\varepsilon_o}}} \quad (3.13)$$

This can be simplified to

$$R = \frac{\sqrt{\frac{\mu_r}{\varepsilon_r} - 1}}{\sqrt{\frac{\mu_r}{\varepsilon_r} + 1}}. \quad (3.14)$$

Rearranging Equation 3.14 leads to the final form

$$z = \sqrt{\frac{\mu_r}{\varepsilon_r}} = \frac{1 + R}{1 - R}, \quad (3.15)$$

where z is commonly called the normalized intrinsic impedance. Similarly, the expanded expression for k can be used to expand the expression for P as

$$P = e^{-jkd} = e^{-j\frac{\omega}{c}\sqrt{\mu_r \varepsilon_r}d}. \quad (3.16)$$

Solving Equation 3.16 for $\sqrt{\mu_r \varepsilon_r}$ yields [67]

$$y = \sqrt{\mu_r \varepsilon_r} = \frac{jc \ln P}{\omega}. \quad (3.17)$$

Using Equations 3.15 and 3.17, one can write expressions for μ_r and ε_r in terms of R and P which can be expressed using only the measured S-parameters (Equations 3.9

and 3.12) [67].

$$\mu_r = yz, \quad \varepsilon_r = \frac{y}{z} \quad (3.18)$$

Thus, μ_r and ε_r can be found using only the S-parameter measurements.

3.3.2 Metamaterial Constitutive Parameter Extraction. Smith *et al.* were the first to use the NRW algorithm to extract constitutive parameters from metamaterial measurements obtained from simulations. They used reflection and transmission coefficients (effectively S_{11} and S_{21}) generated using a transfer matrix simulation on a periodic array of wires, a periodic array of SRRs, and a periodic array of a wire-SRR structure. The extracted constitutive parameters for these media were consistent with Equations 3.2 and 3.3 [89]. Markoš and Soukoulis obtained similar results using simulated reflection and transmission coefficient data to obtain the constitutive parameters of metamaterials [61].

There are some issues which must be considered when extracting constitutive parameters from metamaterials using the NRW algorithm. Smith *et al.* emphasize the process is only accurate when measuring metamaterials which do not have chiral or bianisotropic effects [89]. A metamaterial consisting of an array of wires does not exhibit any of these behaviors. However, as shown by Marqués *et al.*, an array of SRRs does exhibit bianisotropic effects [62]. This does not mean Smith *et al.*'s material parameters are not accurate because their devices possessed small chiral effects. Thus, admittedly their measurements could not be considered exact, but they believed they were still a good estimate of the constitutive parameters [89]. Thus, when performing these types of measurements, one must have a general idea as to the extent the material will exhibit bianisotropic behavior. If it is theoretically believed the material will have large chiral effects, than an alternate method to extract material parameters will be required [58]. This is due to the fact the wave number, k , is a function of not only μ and ε but also the magnetoelectric coupling coefficients. Hence, the NRW algorithm assumes the material being analyzed is isotropic and homogeneous.

Another issue encountered when extracting material parameters from S-parameter measurements of metamaterials using the NRW algorithm has to do with the sign choice on the square root used in the parameter extraction. To help explain, consider an alternate form of the equations used to determine z . As noted in the previous section, z is the normalized impedance. Equation 3.15 can be expanded and expressed using only the S-parameter measurements.

$$z = \pm \sqrt{\frac{(1 + S_{11})^2 - S_{21}^2}{(1 - S_{11})^2 - S_{21}^2}} \quad (3.19)$$

Note that z will have both a real and imaginary component due to the complex nature of the S-parameter measurements. For passive materials, the real part of the normalized impedance must be positive [22], which makes the sign choice in Equation 3.19 obvious.

The assumption of passive materials also helps in determining another sign choice in the parameter extraction. Recall that $P = e^{-jkd}$ and that $k = \omega\sqrt{\mu_r\mu_o\varepsilon_r\varepsilon_o}$. The index of refraction, n can be defined as

$$n = \sqrt{\mu_r\varepsilon_r}. \quad (3.20)$$

Additionally, the free space wave number, k_o is defined as

$$k_o = \omega\sqrt{\mu_o\varepsilon_o}. \quad (3.21)$$

Using Equations 3.20 and 3.21, the equation defining the phase advance, P , can be rewritten as

$$P = e^{-jk_ond}. \quad (3.22)$$

Equation 3.22 can be expressed solely in terms of the S-parameter measurements.

$$e^{-jk_ond} = X \pm j\sqrt{1 - X^2} \quad (3.23)$$

where

$$X = \frac{1}{2S_{21}(1 - S_{11}^2 + S_{21}^2)}. \quad (3.24)$$

The sign choice in Equation 3.22 is made knowing the imaginary part of the refractive index for passive materials must be less than zero [89]. Solving for the real part of the refractive index does present problems due to the multiple branches of the complex logarithm. Specifically, when solving Equation 3.22, one gets

$$\ln P + jm2\pi = -jk_o nd, \quad (3.25)$$

where the $jm2\pi$ term accounts for the branch choice. Note that $\ln P$ will have both a real and imaginary component because P is a complex quantity. Hence, this can be rewritten as

$$Re[\ln(P)] + jIm[\ln(P)] + jm2\pi = -jk_o nd. \quad (3.26)$$

Solving for n yields

$$n = \frac{1}{k_o d} ([-Im \ln(P)] - 2m\pi + jRe[\ln(P)]). \quad (3.27)$$

Due to branch cuts, the real part of n is ambiguous. This ambiguity typically does not cause problems because the thickness of a material sample is usually known. This may not be the case for a metamaterial. Ambiguities can arise because the sample width and the reference plane (first effective boundary) of a sample of metamaterial are sometimes not known. The reference plane is the location after which reflected waves from plane wave incidence exhibit plane wave behavior [22]. Additionally, the sample width of a metamaterial may also be ambiguous due to the fact metamaterials may not have well defined surfaces. In [89], Smith *et al.* note that more than one sample thickness must be measured in order to identify the correct branches. Different thicknesses should result in the same material parameters; thus, the two measurements are compared and the branch which makes the solutions identical is chosen. The authors suggest using sample thicknesses as small as possible in order

to make the branch cuts further apart, which will make the selection of the correct branch easier.

Chen *et al.* present an improved method for choosing the correct branch cut. They use the requirement the constitutive material parameters are continuous functions of frequency [89] and use an iterative approach. They assume they have a correct value for the refractive index at a given frequency and use a Taylor series to expand P in Equation 3.22 at the next sampled frequency and choose the branch cut which as close to possible enforces the continuity requirement [22].

Other authors have used the NRW algorithm to extract constitutive material parameters from both simulated and experimental S-parameter data from metamaterials. Ziolkowski simulated arrays of SRRs and also arrays of capacitively loaded strips. His designs were simulated using High Frequency Structure Simulator (HFSS), a commercial FEM-based electromagnetics software package and also using the commercial FDTD package produced by Ocotillo ElectroMagnetics. He provided a slight deviation to the extraction formulas because he noted when S_{11} and S_{21} are nearly zero, choosing the sign of a square root becomes ambiguous. His measured results compared favorably to experimental results, with the errors attributed to imprecision in the manufacturing of the devices [108].

Greggor *et al.* simulated a standard SRR and wire configuration in the 13 - 15 GHz range using Microwave Design Studio . They used the simulated S-parameters to determine the refractive index, n . They then manufactured the metamaterial and obtained measurements. Values for n obtained from the simulated data were in agreement within 20% of the values obtained using measured data [37]. Smith *et al.* used the same parameter retrieval method they developed in [89] to extract the material parameters from metamaterials whose unit cells were not homogeneous. They simulated metal wire and SRR unit cell arrays using HFSS. They found no changes were necessary provided the unit cells are periodic along the direction of propagation [90].

Chen *et al.* used the same NRW algorithm, although their equations were slightly different because they interrogated the material in a waveguide using a dominant TE₁₀ mode, which changes the impedance of the medium and the resulting equations for μ_r and ε_r developed in Section 3.3.1. They obtained S-parameter measurements of an array on metamaterial unit cells with an SRR-type geometry. By rotating the geometry of the SRRs and then performing different S-parameter measurements, Chen *et al.* were able to extract the entire permittivity and permeability tensors, something which had not yet been done using measured data [19].

For the work discussed in Chapter VI, the parameter retrieval method discussed in this and the previous subsections are used. The software package to perform simulated S-parameter measurements on unit cells used was Comsol Multiphysics, which has not been cited as used for this type of work in the literature. However, at the 2008 Comsol Multiphysics conference, Urzhumov presented a detailed procedure to extract constitutive parameters from simulated S-parameter measurements using Comsol. His method mirrored that presented in this subsection, with the only differences being in the implementation in the software [92]. This will be discussed further in Chapter VI

3.4 *Alternate Parameter Retrieval Method*

An alternate technique to extract material parameters for metamaterial unit cells was put forth by Smith and Pendry. The process is called field averaging. The extraction of material parameters using this method can only be accomplished from simulations of unit cells. It is not applicable to experimental data. Fundamentally, field averaging is a rather simple concept. It uses the basic relationship between the electric (magnetic) field and electric (magnetic) displacement vectors. Specifically, for materials with no magnetoelectric coupling, the relationships are

$$D = \varepsilon_o \vec{\varepsilon}_r \cdot \vec{E} \quad B = \mu_o \vec{\mu}_r \cdot \vec{H} \quad (3.28)$$

A plane wave excitation in one of the unit axis directions is assumed. Additionally, the medium is assumed to be reciprocal i.e. the constitutive parameter tensors only have nonzero diagonal terms. It is possible to solve for the component values ($\varepsilon_x, \varepsilon_y, \varepsilon_z, \mu_x, \mu_y, \mu_z$) by using the simulated values for all field components and performing a simple division. As an example, for a plane wave excitation that has only an \hat{x} -directed electric field, $\varepsilon_x = \frac{D_x}{E_x}$.

In a metamaterial unit cell simulation, the field values are known at all points in the geometric grid used to model the material. Obviously one cannot simply perform this division at each location in the grid because the goal is to define bulk material parameters. Thus, Smith and Pendry define field averages along the various faces and edges of the unit cells, which are then used as the bulk values to calculate the permittivity and permeability tensors [91]. Simulations of various metamaterial cell geometries were performed and material parameters extracted. Results closely matched those obtained using the NRW retrieval techniques previously discussed. It was noted during the analysis the extracted parameters exhibited a spatial dispersion. If the unit cells were filled with nothing i.e. a metamaterial composed solely of free space, the extracted material parameters were μ_o and ε_o but multiplied by a $\frac{\sin(x)}{x}$ -type term. Thus, the spatial dispersion in the parameters was determined to be a function of the simulation. Fortunately, it appears the dispersion can be eliminated simply by scaling by the $\frac{\sin(x)}{x}$ term [91]. The advantage of parameter extraction using field averaging is there are no decisions required in terms of signs on square roots or on logarithm branches. The disadvantage is, although quite simple in concept, implementation is fairly complex and computationally expensive. There are other approaches similar to field averaging, such as field summation that are conceptually similar, the exception being how the bulk field values are computed [57].

3.5 Tunable Metamaterials

As discussed in Sections 3.1 and 3.2, it is possible to create metamaterials with specific electric and magnetic properties. However, once the devices are created, the

resonant frequencies are fixed. There has been research into unique ways to alter the resonant frequency of general SRR-structures following fabrication of the devices.

Aydin and Ozbay manufactured SRRs, similar to the one showed in Figure 3.4, and altered the SRR's capacitance by mounting capacitors between various aspects of the SRR. This is shown in Figure 3.9. Note how the capacitors are mounted both



Figure 3.9: SRR devices with capacitors mounted post-fabrication [11]

between the gaps in each of the rings and also between the inner and outer rings themselves. The mounted capacitor obviously changed the overall capacitance of the cell, which would down shift the magnetic plasma frequency (ω_{pm} in Equation 3.3). Aydin and Ozbay proved the change in frequency by measuring the S-parameters of the device before and after capacitor mounting [11]. As expected, when different capacitor values were used, different magnitudes of frequency shift were observed.

Shadrivov *et al.* did similar work, except instead of mounting a standard capacitor between the gaps or rings of a standard SRR, they mounted a variable-capacitor-diode, whose capacitance can be controlled by applying a DC bias voltage. Their device is shown in Figure 3.10. By varying the voltage from -1 to 1 volt, they were able to achieve a tuning range of 630 MHz [82]. Similar work was done by Gil *et al.* who mounted a varactor onto a SRR and achieved approximately 500 MHz of tuning capability [36]. Hand and Cummer also tuned the resonant frequency of an SRR, but they used a microelectromechanical systems (MEMS) switch to alter the capacitance of the structure. Unlike Gil *et al.* and Shadrivov *et al.*, Hand and Cummer did not obtain a tuned range of operating frequencies. Rather, turning the switch on or off created two different resonant frequencies approximately 800 MHz apart [38].



Figure 3.10: Variable-capacitor-diode mounted on an SRR device [82]

Degiron *et al.* performed conceptually similar experiments in that their desire was to control the magnetic resonance of an SRR-type structure. However, their approach was rather unique. They used a single gapped ring of copper (in essence, only one of the rings of an edge-coupled SRR) and placed a piece of n-type silicon in the gap. This is shown in Figure 3.11. An 815 nm laser was used to illuminate the

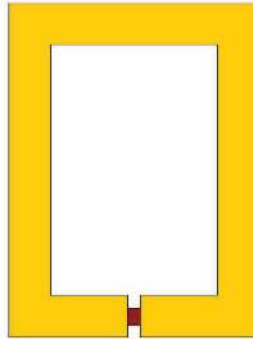


Figure 3.11: N-type silicon in SRR gap

silicon at intensity levels from 0 - 5 mW. S-parameter measurements were taken, with the primary focus being on the S_{21} i.e. transmission parameter. As the intensity of the illumination increased, the conductivity of the silicon increased, thereby shorting out the ring and removing the resonance, which manifested itself as an increase in the S_{21} measurement. Degiron *et al.* also found controlling the gap between the silicon and the edge of the rings had an effect on the resonant frequency of the device [29].

Finally, Rederus used a variable capacitive MEMS device mounted in gap in an SRR. The MEMS device consisted of cantilevered beams that, when activated, would alter the capacitance of the SRR, thus changing the resonant frequency [75]. The main advantage of Rederus's design was his device was fabricated in-situ with the SRR, resulting in a much cleaner device than those fabricated by Aydin and Ozbay and Shadrivov *et al.* Due to technical issues, S-parameter measurements were not taken, but it was shown the activated MEMS device could add 0.54 - 0.62 pF of capacitance to the SRR.

3.6 Summary

This chapter presented various unit cell structures which have been used to create effective bulk permittivity and/or permeability effects in man-made materials. The NRW algorithm, which can be used to extract the material parameters from some geometries, was documented with its limitations and ambiguities when measuring metamaterials were delineated.

IV. Improved Simplified Parameters for Two-Dimensional Cylindrical Cloaks

In Section 2.2, it was shown Schurig *et al.* made an error when deriving the wave equation for a TM^z electromagnetic field in an anisotropic cloak. Their error was assuming μ_θ was constant [101]. However, as clearly seen in Equation 1.21, the ideal value for μ_θ is not spatially invariant. Thus, the simplified parameter sets developed, while shown to work reasonably well, were not correctly obtained. In this chapter, all constraint equations for the material parameters of an ideal cylindrical cloak are derived using the correct form of the wave equation. Using these constraint equations, it is first shown how varying μ_θ can control the amount of field transmitted into the cloak's hidden region. It is then shown how all constraint equations can be used to derive simplified material parameter sets whose complexity can be tailored depending on the available manufacturing capabilities of metamaterials.

4.1 Constraint Equations

In order to develop all the constraint equations on the material properties of an ideal cylindrical cloak, the correct wave equation must first be derived. Since it is known a priori the ideal parameters are θ -invariant but not r -invariant, the general wave equation for TM^z fields in anisotropic media shown in Equation 2.6 can be expanded analytically to

$$\frac{1}{\varepsilon_z \mu_\theta} \frac{\partial^2 E_z}{\partial r^2} + \left[\frac{1}{\varepsilon_z \mu_\theta} \frac{1}{r} - \frac{\mu'_\theta}{\varepsilon_z \mu_\theta^2} \right] \frac{\partial E_z}{\partial r} + \frac{1}{\varepsilon_z \mu_r} \frac{1}{r^2} \frac{\partial^2 E_z}{\partial \theta^2} + k_o^2 E_z = 0. \quad (4.1)$$

Note ' implies differentiation with respect to r . This analysis can be extended to TE^z fields by letting

$$E_z \rightarrow H_z, \quad \varepsilon_z \rightarrow \mu_z, \quad \mu_\theta \rightarrow \varepsilon_\theta, \quad \mu_r \rightarrow \varepsilon_r. \quad (4.2)$$

Recall the ideal parameters for an ideal cylindrical cloak for TM^z incident fields are

$$\mu_r = \frac{r-a}{r}, \quad \mu_\theta = \frac{r}{r-a}, \quad \varepsilon_z = \left(\frac{r-a}{r}\right) \left(\frac{b}{b-a}\right)^2. \quad (4.3)$$

When one uses the ideal cylindrical cloak's material parameters shown in Equation 4.3 in the general wave equation shown in Equation 4.1, the result is the wave equation for TM^z fields in an ideal cylindrical cloak.

$$\left(\frac{b-a}{b}\right)^2 \frac{\partial^2 E_z}{\partial r^2} + \left(\frac{b-a}{b}\right)^2 \frac{1}{r-a} \frac{\partial E_z}{\partial r} + \left(\frac{b-a}{b}\right)^2 \left(\frac{1}{r-a}\right)^2 \frac{\partial^2 E_z}{\partial \theta^2} + k_o^2 E_z = 0 \quad (4.4)$$

As discussed in Section 2.2, the original simplified material parameters for cylindrical cloaks for TM^Z incident field are

$$\mu_r = \left(\frac{r-a}{r}\right)^2, \quad \mu_\theta = 1, \quad \varepsilon_z = \left(\frac{b}{b-a}\right)^2. \quad (4.5)$$

The material parameters shown in Equation 4.5 were initially thought to satisfy the same wave equation as the ideal parameter set. However, Yan *et al.* showed the procedure leading to this conclusion was questionable by proving the simplified and ideal parameter sets satisfy different wave equations [101]. This is explicitly seen by substituting the simplified material parameters shown in Equation 4.5 into Equation 4.1. The resulting wave equation is shown below.

$$\left(\frac{b-a}{b}\right)^2 \frac{\partial^2 E_z}{\partial r^2} + \left(\frac{b-a}{b}\right)^2 \frac{1}{r} \frac{\partial E_z}{\partial r} + \left(\frac{b-a}{b}\right)^2 \left(\frac{1}{r-a}\right)^2 \frac{\partial^2 E_z}{\partial \theta^2} + k_o^2 E_z = 0 \quad (4.6)$$

Note the subtle difference in Equation 4.6 compared to Equation 4.4. The wave equation using the original simplified parameters has a $1/r$ factor in front of the $\partial E_z/\partial r$ term. The wave equation using the ideal parameters has a factor of $1/(r-a)$ for this same term. Thus, for values such that $r \gg a$, the field behavior of the two cloaks will be similar [101], but they certainly do not satisfy the same wave equation. Since the ideal cylindrical cloak effectively guides electromagnetic energy around the hidden region, it makes sense that a simplified cloak, whose wave equation differs from

that of the ideal cloak, has energy transmitted into this same region [101]. It also makes sense that, because the wave equations are similar for the region away from $r = a$, the simplified parameter set performed reasonably well in terms of cloaking capability.

By comparing Equations 4.1 and 4.4, one finds the cylindrical cloak's constitutive parameters must meet the following conditions in order to achieve ideal cloaking for TM^z fields [63].

$$\frac{1}{\varepsilon_z \mu_\theta} = \left(\frac{b-a}{b} \right)^2 \quad (4.7)$$

$$\frac{1}{\varepsilon_z \mu_r} = \left(\frac{b-a}{b} \right)^2 \left(\frac{r}{r-a} \right)^2 \quad (4.8)$$

$$\frac{1}{\varepsilon_z \mu_\theta} \frac{1}{r} - \frac{\mu'_\theta}{\varepsilon_z \mu_\theta^2} = \frac{1}{r-a} \left(\frac{b-a}{b} \right)^2 \quad (4.9)$$

The third constraint equation given in Equation 4.9 had not appeared in the literature prior to this research and forms the basis for the alternative simplified parameters proposed later in this chapter.

The ideal cylindrical cloak also has an impedance at the outer boundary, $r = b$, that matches free space.

$$Z_{ideal} = \sqrt{\frac{\mu_\theta}{\varepsilon_z}} \Big|_{r=b} = 1 \quad (4.10)$$

The simplified parameters shown in Equation 4.5 satisfy Equations 4.7 and 4.8 but do not satisfy Equation 4.9. Additionally, the impedance mismatch at $r = b$ for the cylindrical cloak with the same simplified constitutive parameters and using $a = \lambda$ and $b = 2\lambda$ is

$$Z_{simp} = \sqrt{\frac{\mu_\theta}{\varepsilon_z}} \Big|_{r=b} = 0.5 \quad (4.11)$$

Obviously, there will be a scattered field from the simplified cylindrical cloak with an object in its hidden region. However, what is the dominant factor in the scattered field? Is it the impedance mismatch at $r = b$, or is it due to a scattered field resulting from the incident field being transmitted into the hidden region and being

reflected by the hidden object? This question motivated the investigation discussed in the following paragraphs. Initially, this work attempted to minimize the energy transmitted into the hidden region. It was theorized less energy transmitted into the hidden region would result in less energy that can be scattered by the cloaked object, possibly resulting in a smaller total scattered field. The constraints on the cylindrical cloak's ideal constitutive parameters defined in Equations 4.7 - 4.9 were used to define parameter sets in order to control the amount of energy transmitted into the cloak's hidden region. The cloaks' effectiveness was then analyzed in terms of the amount of energy in the hidden region and of the overall scattering width of the cloaking structure.

Simulations using Comsol Multiphysics were performed on the original simplified cylindrical cloak (Equation 4.5). These were performed with a PEC cylinder with radius $r = a$ and a square PEC with side length a separately in the cloak's hidden region. These objects were chosen because the intent was to show objects with different scattering properties placed in the hidden region impact the cloak's overall scattered field. Since the simulation wavelength is $\lambda = a$, the objects placed in the hidden region are on the order of one wavelength in size. The chosen objects have significantly different shapes and areas; thus, the overall scattered fields should differ due to field penetration into the hidden region. Additionally, a simulation was done with no objects in the hidden region. All simulation results are shown in Figure 4.1. Note the fields in the hidden region for the empty cloak, an expected result based on the work done in [101]. Based on these images, it is difficult to fully comprehend the size and pattern of the scattered field for each geometry. Therefore, the Comsol simulation results were transformed to a far zone two-dimensional scattering width. The scattering width for each geometry is plotted as a function of θ in Figure 4.2 (θ is the bistatic angle with $\theta = 0^\circ$ being the forward scatter direction). Every scattering width plot in this section is normalized by the maximum scattering width value for an uncloaked PEC cylinder of radius a .

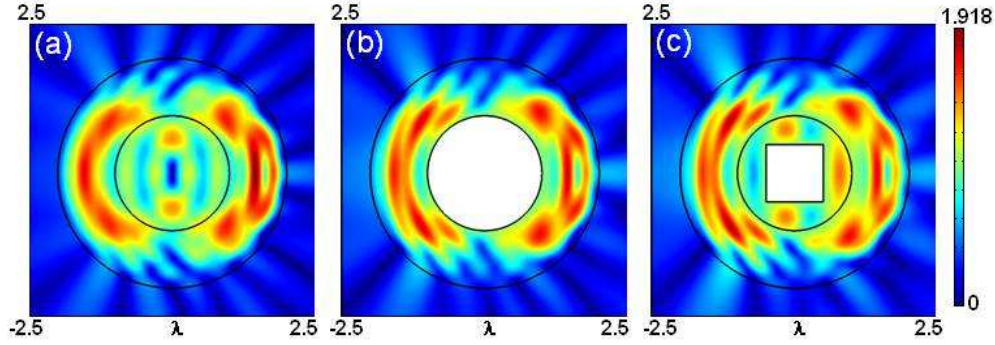


Figure 4.1: Scattered electric field magnitudes for a simplified cylindrical cloak that has (a) nothing, (b) a PEC cylinder with radius a , and (c) a square PEC of side length a in the hidden region.

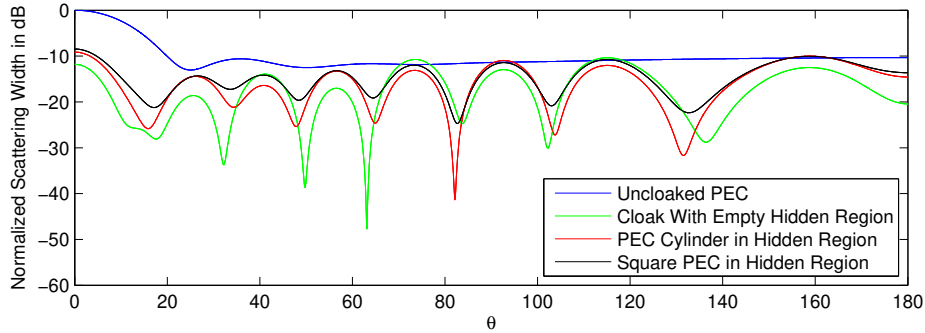


Figure 4.2: Normalized scattering width for a simplified cloak with various hidden objects.

Note the cloaked PEC cylinder (red line in Figure 4.2) does have a smaller scattering width than an uncloaked PEC cylinder (blue line). Also note the variation in the scattering widths between the cloaked cylinder and square (black line). This variation is due to different objects being placed in the hidden region. To better see how the scattering width is changed when different objects are inserted into the hidden region, the difference between the scattering widths of a cloaked PEC cylinder and cloaked PEC square were plotted. The results are shown in Figure 4.3. Obviously, changing the object in the hidden region has an impact on the overall scattered field for this set of constitutive parameters. The question is, will minimizing the field transmitted into the hidden region reduce the overall scattered field variations caused by the different hidden objects?

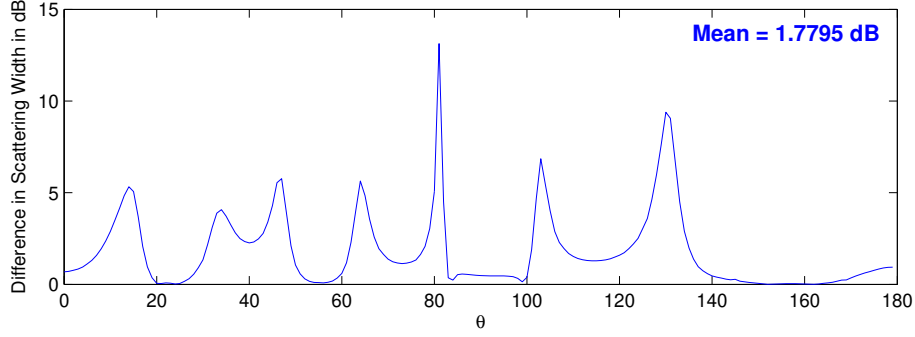


Figure 4.3: Scattering width difference for a simplified cloak with a PEC cylinder and a PEC square in the hidden region.

As discussed in Section 2.2, there have been suggested improvements to the original simplified constitutive parameters [14, 101]. The improved set of constitutive parameters for TM^z incident fields put forth in [102] are shown in Equation 4.12.

$$\mu_r = \left(\frac{r-a}{r}\right)^2 \frac{b}{b-a}, \quad \mu_\theta = \frac{b}{b-a}, \quad \varepsilon_z = \frac{b}{b-a}. \quad (4.12)$$

The improved parameter set was developed with the goal of reducing the overall scattering width of the cloaking structure by matching the cloak's impedance to free space at $r = b$ while still satisfying the requirements shown in Equations 4.7 and 4.8. As with the initial simplified parameters, the improved set does not satisfy the third constraint equation shown in Equation 4.9. Comsol simulations of a cylindrical cloak with the constitutive parameters shown in Equation 4.12 were performed. The cloak was simulated with no object in the hidden region, and with a PEC cylinder of radius a and a square PEC with side length a separately in the hidden region. The results are shown in Figure 4.4. It is obvious the scattered field magnitudes in the region $r > b$ are larger for the two cloaks with objects in the hidden region. To better show this, the scattered field results were transformed to the far zone. These results are shown in Figure 4.5. The goal of reducing the overall scattering width from a cloak with simplified parameters was achieved using the constitutive parameters shown in Equation 4.12. This is due to the matched impedance at $r = b$. However, notice how the scattered fields have a greater change in magnitude when the objects in the

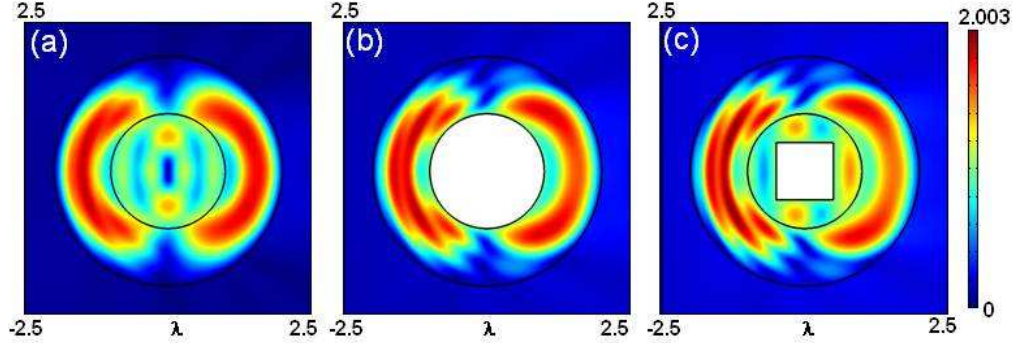


Figure 4.4: Scattered electric field magnitude for an improved cylindrical cloak that has (a) nothing, (b) PEC cylinder of radius a , and (c) square PEC of side length a in the hidden region.

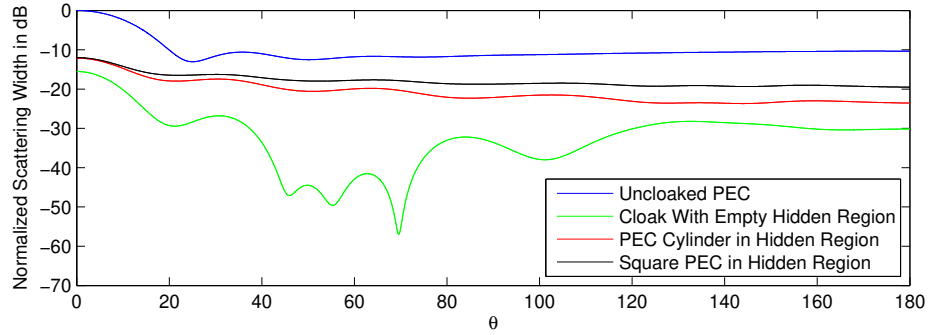


Figure 4.5: Normalized scattering widths from an improved simplified cloak.

hidden region are changed. As before, this can be seen by comparing the difference in the scattering widths for the cloaked PEC cylinder (red line in Figure 4.5) and the cloaked square PEC (black line). This is shown in Figure 4.6. The average difference in scattering width for a simplified cylindrical cloak with the parameters shown in Equation 4.5 having a PEC cylinder and square in the hidden region was 1.77 dB. The average difference in scattering width for the improved cylindrical cloak with the parameters shown in Equation 4.12 was 2.90 dB. Therefore, even though overall scattering width has been reduced (due to the matched impedance at $r = b$), the larger variation in the scattered fields when different objects were placed in the hidden region suggests more energy is being transmitted into the hidden region of the cloak with the improved constitutive parameters than the hidden region for the cloak with the original simplified parameters. This implies a matched impedance at $r = b$ is

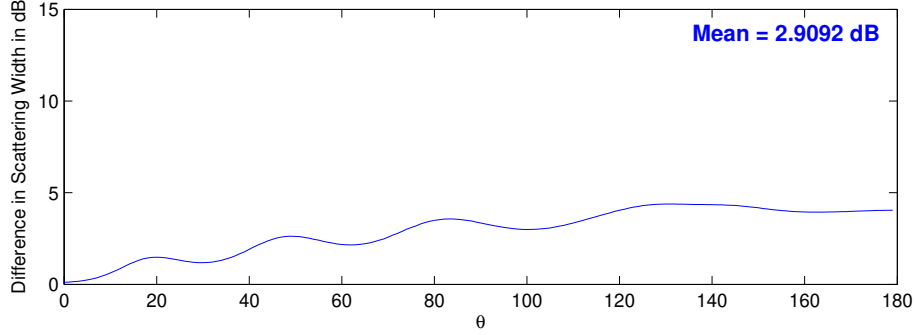


Figure 4.6: Scattering width difference for an improved simplified cloak with a PEC cylinder and a square PEC in the hidden region.

more important for signature width reduction than minimizing the field transmitted into the hidden region. This is further tested in the next section. It will be shown for these two cloaks that the value of μ_θ determines the size of the field transmitted into the hidden region.

4.2 Reducing field transmission into the hidden region

As previously mentioned, the constitutive parameters of an ideal cloak for TM^z incident waves must satisfy the constraints shown in Equations 4.7 - 4.9. The simplified cloaks in the literature focus on satisfying Equations 4.7 and 4.8. Equation 4.9 has never before been discussed, likely due to the assumptions used when the initial set of simplified parameters was put forth. In what follows, the importance of Equation 4.9 is analyzed in terms of overall scattering width and of how well the hidden region is shielded from incident energy.

If one first assumes a cloak's constitutive parameters satisfy Equations 4.7 and 4.8, Equation 4.9 can be written in a more compact form. This is shown in Equation 4.13.

$$\mu'_\theta + \mu_\theta \frac{a}{r(r-a)} = 0 \quad (4.13)$$

Note that $a < r \leq b$. The analysis is initially confined to cloaks with a constant value for μ_θ (i.e. $\mu'_\theta = 0$). This means the smaller μ_θ , the less error there will be for any value of r when trying to satisfy Equation 4.13. The left-hand side of Equation

4.13 can be calculated using the values for μ_θ for the initial simplified parameter set ($\mu_\theta = 1$) and the improved parameter set ($\mu_\theta = \frac{b}{b-a}$). These are plotted as a function of r in Figure 4.7. For this plot, $a = 1$ and $b = 2$. Two additional plots are shown in this graph, and these will be discussed later. Since the ideal value for

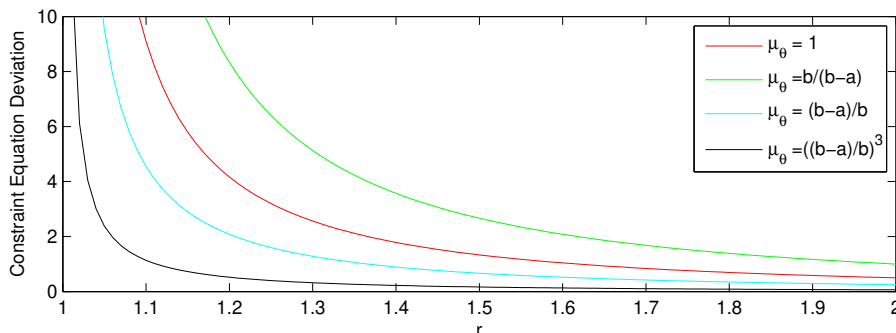


Figure 4.7: The calculated values for the left-hand side of Equation 4.13 using non-ideal values for μ_θ . Values for μ_θ are 1 (red line), $\frac{b}{b-a}$ (green line), $\frac{b-a}{b}$ (cyan line), and $\left(\frac{b-a}{b}\right)^3$ (black line).

Equation 4.13 is zero for all values of r . A larger calculated value for the left-hand side of Equation 4.13 using a non-ideal value for μ_θ means a larger deviation in the material parameter from that of the ideal cloak. Based on this graph, one would expect to find the field transmitted into the hidden region for the cloak with the initial simplified parameter set ($\mu_\theta = 1$) to be less than the hidden region field for the improved parameter set ($\mu_\theta = \frac{b}{b-a}$). This is due to the fact the value for μ_θ for the initial parameter set results in a smaller error in Equation 4.13 than the value for μ_θ in the improved parameter set. Hence, changing objects in the hidden region for the cloak with the original simplified parameters (Figure 4.1) would have less impact on the overall scattered field than changing objects in the hidden region of a cloak with the improved parameters (Figure 4.4). This is precisely what we have shown in Figures 4.3 and 4.6.

Other parameter sets can satisfy Equations 4.7 and 4.8 but also further reduce the deviation from Equation 4.13, resulting in a reduction in the field transmitted into the hidden region. The parameter sets shown in Equations 4.14 and 4.15 meet these

conditions. Their deviations from the ideal value of Equation 4.13 were calculated. The results are plotted in Figure 4.7.

$$\mu_r = \left(\frac{r-a}{r}\right)^2 \frac{b-a}{b}, \quad \mu_\theta = \frac{b-a}{b}, \quad \varepsilon_z = \left(\frac{b}{b-a}\right)^3. \quad (4.14)$$

$$\mu_r = \left(\frac{r-a}{r}\right)^2 \left(\frac{b-a}{b}\right)^3, \quad \mu_\theta = \left(\frac{b-a}{b}\right)^3, \quad \varepsilon_z = \left(\frac{b}{b-a}\right)^5. \quad (4.15)$$

Obviously no attempt was made to match impedances at the $r = b$ interface for the parameter sets shown in Equations 4.14 and 4.15, as the goal was to show a reduction in the field transmitted into the hidden region. The cloaks were simulated with material parameters shown in Equations 4.14 and 4.15 with a PEC cylinder of radius a and with a square PEC with side length a in the hidden region. The difference in scattering widths are plotted for each of these cloaks. The results are shown in Figures 4.8 and 4.9. As expected, the average difference in scattering width

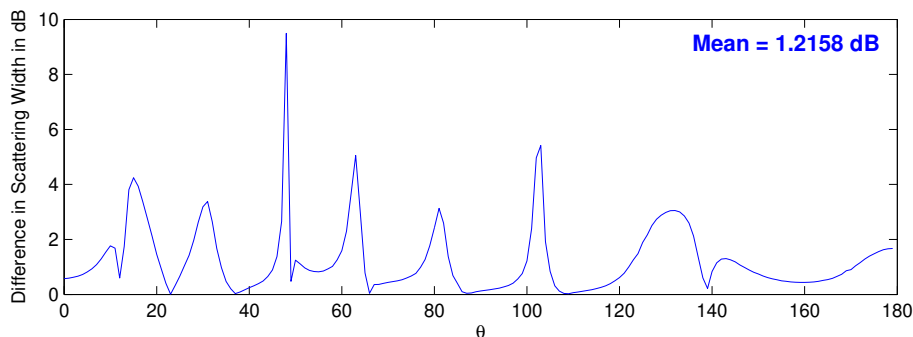


Figure 4.8: Scattering width difference for a cloak with parameters shown in Equation 4.14 with a PEC cylinder and square in the hidden region.

is decreased when $\mu_\theta = \frac{b-a}{b}$ and $\mu_\theta = \left(\frac{b-a}{b}\right)^3$ respectively, leading to the conclusion that the field transmitted into the hidden region is being reduced as μ_θ is decreased.

To further show how Equation 4.13 determines the amount of energy transmitted into a simplified cylindrical cloak's hidden region, cloaks with the material parameters shown in Equations 4.5, 4.12, 4.14, and 4.15 were simulated. No objects were placed in their hidden regions, and the total electric field magnitudes in the hidden regions for each cloak are plotted in Figure 4.10. The images in Figure 4.10 clearly

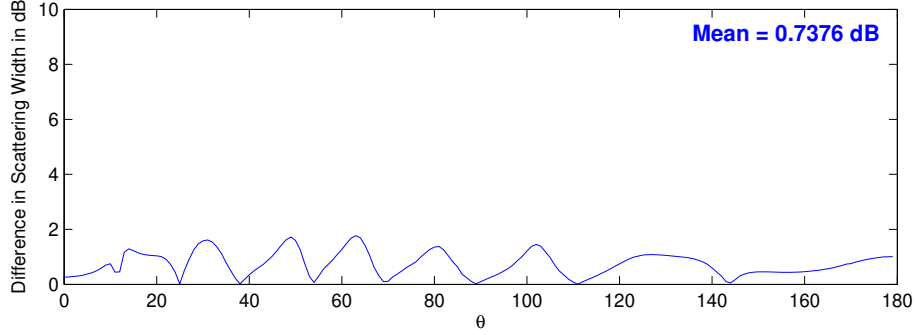


Figure 4.9: Scattering width difference for a cloak with parameters shown in Equation 4.15 with a PEC cylinder and square in the hidden region.

Table 4.1: Hidden Region Total Energy and Impedance for Different Cloaks

μ_θ	Total Energy	$Z _{r=b}$
$\frac{b}{b-a}$	2.76 pJ	1
1	2.24 pJ	0.5
$\frac{b-a}{b}$	1.35 pJ	0.25
$\left(\frac{b}{b-a}\right)^3$	0.42 pJ	0.0625

show as the cloak takes on values of μ_θ which make the left-hand side of Equation 4.13 closer to zero for all values of r , there is less field transmitted into the hidden region. As additional proof, the energy density in the hidden region can be integrated to determine the regions' total energies. These results are shown in Table 4.1. Note the cloak with material parameters shown in Equation 4.15 has the smallest total energy in the hidden region. Therefore it is the best of the four cloaks considered at shielding the hidden region. However, there is a price to pay for this improved shielding performance. Table 4.1 also shows the impedance for each cloak at $r = b$. The cloak with the best shielding of the hidden region also has the worst impedance mismatch at the cloak outer boundary. As demonstrated earlier, an impedance mismatch at the boundary results in the cloaking body having a significant scattered field. Therefore, to compare performance in terms of scattering width reduction, scattering widths were plotted for all cloaks with a PEC cylinder of radius a in the hidden region. This is shown in Figure 4.11. The blue line is the normalized scattering width for an uncloaked PEC, the red line is the normalized scattering width for cloak with

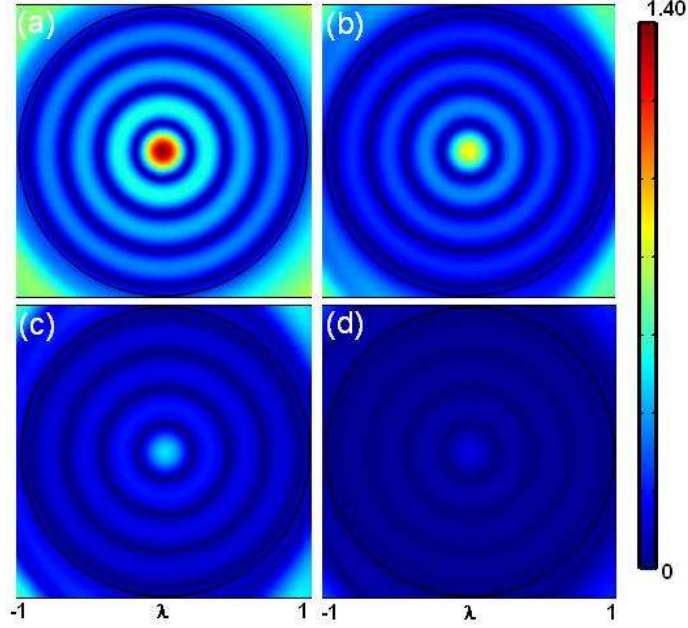


Figure 4.10: Electric field magnitude in the hidden region for cloaks with material parameters defined by (a) Equation 4.12, (b) Equation 4.5, (c) Equation 4.14, and (d) Equation 4.15.

the simplified parameter set (Equation 4.5), the green line is the scattering width for a cloak with the improved parameter set (Equation 4.12), and the cyan and black lines are the scattering widths for cloaks with parameter sets shown in Equations 4.14 and 4.15 respectively. By altering the material parameters such that less fields are transmitted into the hidden region, the change in impedance at $r = b$ dramatically increases the overall scattering width of the cloaking structure. Obviously if scattering width reduction is the goal, use of the improved simplified parameter set (Equation 4.12, [102]) is the best option as its scattering width is significantly less than an uncloaked PEC cylinder. The two new cloaks actually have larger scattering widths at various observation angles than the uncloaked PEC, making them a bad choice if signature reduction is desired. However, if one is attempting to simply shield an object from incident radiation, then the use of Equation 4.9 becomes important in that parameters should be chosen such that the deviation from this equation is minimized. One may say shielding can easily be accomplished using a PEC; why use a modified cloak for such a task? A PEC does act as a suitable barrier for a large

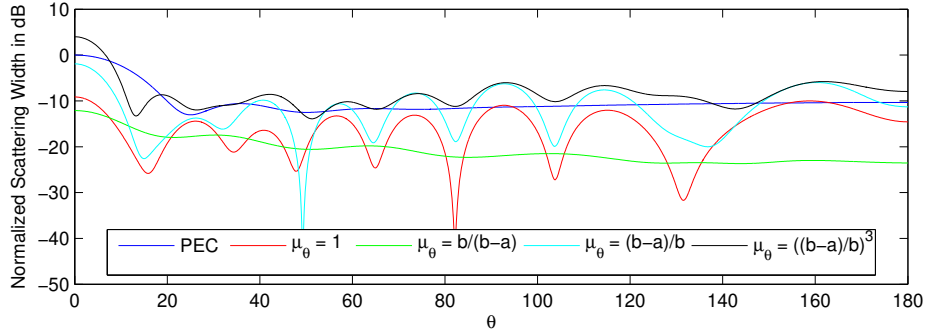


Figure 4.11: Scattering widths for cloaks with a PEC cylinder of radius a in the hidden region.

bandwidth of electromagnetic radiation. However, at extremely low frequencies, skin depths must be considered. It might be less costly, in terms of weight or size, to use a designed cloak for such a shielding application.

It has been shown that, in terms of overall signature reduction, the cloak put forth in [102] is the best option, and that this particular cloak satisfies Equations 4.7 and 4.8 and has a matched impedance at $r = b$. However, note the significant variation in the scattered field when different objects are placed in this cloak's hidden region. Is it possible to reduce this variation in the scattered field with different objects in the hidden region while maintaining the overall reduction in scattering width?

There are four parameters that must be met for a cylindrical cloak to be perfect: Equations 4.7, 4.8, and 4.9 must be satisfied, and the cloak must have a matched impedance at $r = b$. To this point, simplified cloaks that satisfy Equations 4.7 and 4.8, and that either do or do not have a matched impedance at $r = b$ have been analyzed. The results showed the cloak with the matched impedance results in the best improvement in scattering width even though this cloak has the largest field transmitted into its hidden region.

Now, consider a cloak with material parameters shown in Equation 4.16.

$$\mu_r = 0.5, \quad \mu_\theta = \frac{r}{r-a}, \quad \varepsilon_z = \frac{r-a}{r} \left(\frac{b}{b-a} \right)^2. \quad (4.16)$$

Like the improved parameter set put forth in [102], these parameters satisfy three of the four requirements. The difference is these parameters satisfy Equations 4.7 and 4.9 while having a matched impedance at $r = b$. Equation 4.8 is not satisfied.

As done previously, a cloak having the constitutive parameters shown in Equation 4.16 was simulated with a PEC cylinder of radius a and a square PEC of side length a separately in the hidden region were simulated. The scattered field results are shown in Figure 4.12. Note how the scattered fields for all three images shown in

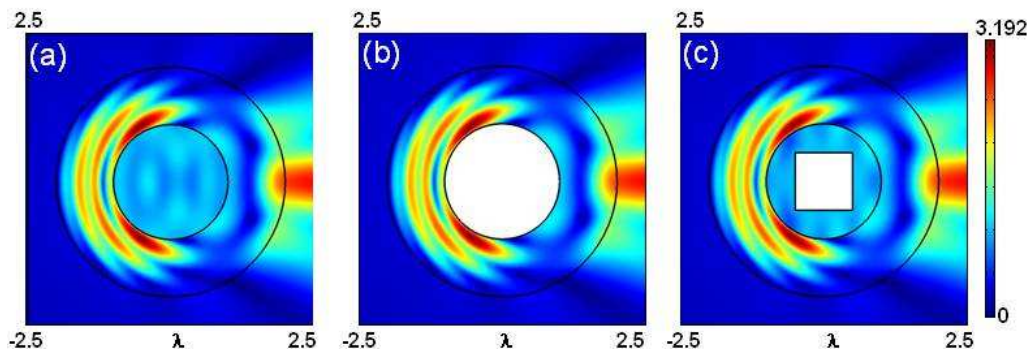


Figure 4.12: Scattered electric field magnitude for a cylindrical cloak with parameters shown in Equation 4.16 that has (a) nothing, (b) PEC cylinder, and (c) square PEC in the hidden region.

Figure 4.12 appear very similar. This suggests different objects in the hidden region have little effect on the scattered field. This can be seen more clearly by transforming the scattered fields to the far zone. This is shown in Figure 4.13. The blue line is

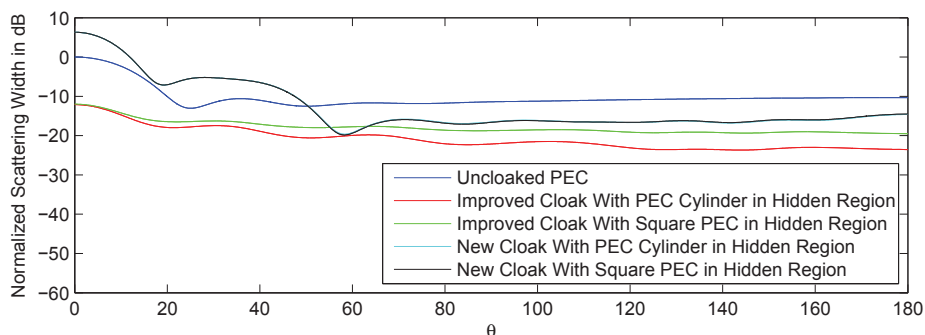


Figure 4.13: Normalized scattering width from cloak defined by Equation 4.16.

the scattering width for an uncloaked PEC, the red and green lines are the scattering

widths for the improved cloak with a PEC cylinder and square PEC in the hidden region. The cyan and black lines are the same but for a cloak with material parameters shown in Equation 4.16. The graphs in Figure 4.13 clearly show there is no difference in the scattering width when different objects are placed in the hidden region of the cloak with parameters put forth in Equation 4.16. Note the cyan and black lines lie virtually on top of the other. In fact, the average difference in the scattering widths is 0.0671 dB. This is because the total field in the hidden region is negligible. The field in the hidden region is negligible because the impedance at $r = a \rightarrow \infty$, which means no energy will be transmitted.

Figure 4.13 shows scattering width results for a cloak using the parameters shown in Equation 4.12. This is done to compare the performance of the cloaks in terms of scattering width. Obviously, the red and green lines are more desirable results because of the smaller scattering width values. However, this cloak's scattering widths vary more as a function of different objects in its hidden region. If various objects are going to be hidden and observation angles are in the specular region, the top cloak may be a better option. Of course, the cloak with parameters put forth in Equation 4.16 has two radially varying parameters, meaning it is currently more difficult to manufacture.

Thus far, cylindrical cloaks that satisfy the ideal values for $\varepsilon_z \mu_\theta$ and $\varepsilon_z \mu_r$ have been analyzed. It has been shown deviations from a third constraint equation shown in Equation 4.9 resulted in larger fields being transmitted into a cylindrical cloak's hidden region. As the cloak's constitutive parameters were changed such that this new constraint was better satisfied, the amount of energy transmitted into the hidden region was shown to be reduced. However, the resulting impedance mismatch at $r = b$ due to changing the constitutive parameters resulted in a significant scattered field. Thus, despite reducing energy transmitted into the hidden region, which resulted in a reduction in the scattered field by the cloaked object, the cloak itself was creating a large scattered field. Hence, in terms of overall scattering width, having a matched

impedance at $r = b$ seems to be more important than reducing the transmitted energy into the hidden region.

A particular cylindrical cloak that satisfied the specific values for $\varepsilon_z \mu_\theta$ and μ'_θ while having a matched impedance at $r = b$ has also been analyzed. For observation angles in the backscatter region, this cloak to performed quite well in terms of scattering width as the scattered field was independent of objects placed in the hidden region. While scattering width performance was not on the same level as the cloak with parameters put forth in [102], the independence of the scattered field due to different objects in the hidden region is noteworthy.

4.3 Improved Cylindrical Cloak Parameters

As discussed in Section 2.2, simplified parameter sets are necessary in order to make cloaks more manufacturable. Due to a derivation error in one of the first papers on simplified cloaks, most simplified parameter sets have focused on the material parameters satisfying Equations 4.7 and 4.8 only. As shown in Section 4.1, a third equation (Equation 4.9) is required in order to fully constrain the material parameters. Recall also from Section 4.1 that if Equation 4.7 is assumed true for a given material parameter set, Equation 4.9 can be rewritten as

$$\mu'_\theta + \mu_\theta \frac{a}{r(r-a)} = 0. \quad (4.17)$$

Equation 4.17 is only a function of the r -varying parameter, μ_θ , and its first derivative, μ'_θ . The solution to this first order differential equation is given by

$$\mu_\theta(r) = C \frac{r}{r-a}. \quad (4.18)$$

Note C is a constant. Initially C is assumed to be unity as this corresponds to a first order transformation, as will be discussed below. Obviously, Equation 4.18 matches the form of μ_θ shown in Equation 1.21. What may not be as obvious is the fact that

Table 4.2: Simplified material parameter values for $N = 0, 1$, and 2 .

N	μ_θ	μ_r	ε_z
0	$\frac{b}{b-a}$	$\frac{b}{b-a} \left(\frac{r-a}{r}\right)^2$	$\frac{b}{b-a}$
1	$\frac{b^2-ar}{(b-a)^2}$	$\frac{b^2-ar}{(b-a)^2} \left(\frac{r-a}{r}\right)^2$	$\frac{b^2}{b^2-ar}$
2	$\frac{b^3-3arb+a^2r+ar^2}{(b-a)^3}$	$\frac{b^3-3arb+a^2r+ar^2}{(b-a)^3} \left(\frac{r-a}{r}\right)^2$	$\frac{b^2(b-a)}{b^3-3arb+a^2r+ar^2}$

the ideal value of $\varepsilon_z \mu_\theta$ is inherently satisfied in Equation 4.17. Thus, to develop a simplified parameter set, one should first obtain an approximate value for μ_θ that is as close as possible to the solution to Equation 4.17. To obtain values for μ_θ that better approximate the ideal value, the solution of the differential equation for μ_θ can be expanded using a Taylor series about the point $r = b$ [26]. Approximations are then made by limiting N in the Taylor series. Thus, the expression for the approximation of μ_θ is

$$\mu_\theta(r) \cong \sum_{n=0}^N \frac{\mu_\theta^n(b)}{n!} (r-b)^n, \quad (4.19)$$

where $\mu_\theta^n(b)$ is the n^{th} derivative of $\mu_\theta(r)$ evaluated at $r = b$. Once the expression for the approximation to μ_θ is determined, values for μ_r and ε_z are found using the remaining constraints defined in Equations 4.7 and 4.8. Since the expansion is performed about the point $r = b$, the impedance at $r = b$ is matched to that of free space. The calculated material parameters using the first term ($N = 0$), the first two terms ($N = 1$), and the first three terms ($N = 2$) to estimate μ_θ are shown in Table 4.2. For $N = 0$, $\mu_\theta = \frac{b}{b-a}$. Consequently, the material values are those of the improved cloak discussed in Section 2.2 and originally put forth in [102]. This explains why the improved cloak was shown to be more effective than the quadratic and original simplified cloaks. Note also that while these expressions may seem complicated, the material parameters themselves are quite well behaved. This is shown in Figure 4.14. As additional terms are included in the Taylor series, μ_θ and ε_z become more varying with respect to r ; they also take on more extreme values at $r = a$. Hence these parameter sets can be used based on the ability to manufacture metamaterials with

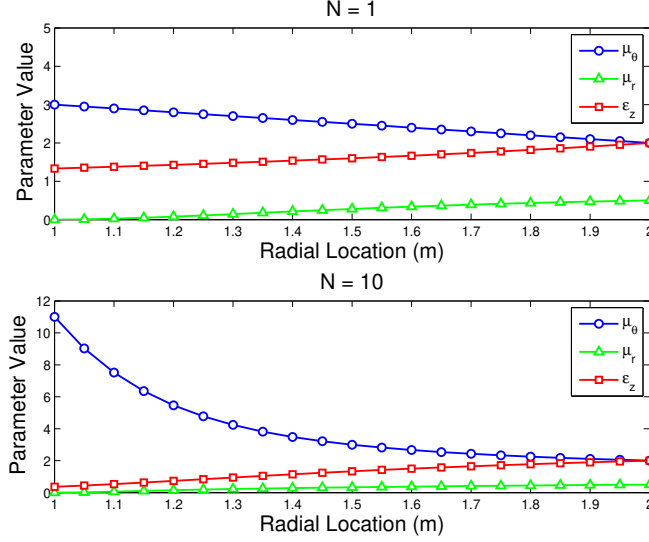


Figure 4.14: Parameter variation as a function of r . In both figures, the \circ -line is μ_θ , the Δ -line is μ_r , and the \square -line is ε_z . In the top figure μ_θ is approximated using $N = 1$; in the bottom figure, $N = 10$.

various properties. If larger values of μ_θ are attainable, simply let N increase to define a new parameter set.

The analysis up to this point has assumed a first-order transformation as shown in Equation 1.7. It can be expanded to include all transformation orders. As an example, an n^{th} -order coordinate transformation that maps the region $r' < b$ to the region $a < r < b$ has the form

$$r = \left(\frac{1}{b^{n-1}} - \frac{a}{b^n} \right) r'^n + a. \quad (4.20)$$

The material parameters for a TM^z electromagnetic field can be found using the method in [72] and are shown below.

$$\mu_r = n \frac{r-a}{r}, \quad \mu_\theta = \frac{1}{n} \frac{r}{r-a}, \quad \varepsilon_z = \frac{(r-a)^{\frac{2}{n}-1}}{rn} \frac{b^2}{(b-a)^{\frac{2}{n}}}. \quad (4.21)$$

As done above, the ideal material parameters shown in Equation 4.21 can be substituted into the general wave equation shown in Equation 4.1 in order to obtain the

constraints on the material parameters.

$$\frac{1}{\varepsilon_z \mu_\theta} = \frac{(b-a)^{\frac{2}{n}}}{b^2} \frac{n^2}{(r-a)^{\frac{2}{n}-2}} \quad (4.22)$$

$$\frac{1}{\varepsilon_z \mu_r} = \frac{(b-a)^{\frac{2}{n}}}{b^2} \frac{r^2}{(r-a)^{\frac{2}{n}}} \quad (4.23)$$

$$\frac{1}{\varepsilon_z \mu_\theta} \frac{1}{r} - \frac{\mu'_\theta}{\varepsilon_z \mu_\theta^2} = \frac{(b-a)^{\frac{2}{n}}}{b^2} \frac{n^2}{(r-a)^{\frac{2}{n}-2}} \left[\frac{1}{r} + \frac{a}{r(r-a)} \right] \quad (4.24)$$

As before, Equation 4.24 can be simplified if Equations 4.22 is assumed to be true. The result is

$$\mu'_\theta + \mu_\theta \frac{a}{r(r-a)} = 0, \quad (4.25)$$

which is identical to Equation 4.13. Hence, the choice of C in Equation 4.18 is important because $C = \frac{1}{n}$ where n is the transformation order. If $C \neq 1$, then one cannot use Equations 4.7 and 4.8 when solving for ε_z and μ_r . Rather, Equations 4.23 and 4.24 must be used to get the proper approximations for the material parameters.

In the next section, the performance of cloaks where μ_θ is approximated using different values of N in the Taylor series are compared.

4.4 Analysis of Cloak Performance

The Comsol Multiphysics software package was used to perform all simulations. Cylindrical cloaks whose material parameters were found using the process described in Section 4.3 using a linear transformation were simulated. The cloaks' inner boundaries were lined with a PEC and an incident wavelength (λ) of one meter traveling in the positive \hat{x} direction was used. The cloak parameters, a and b , were defined such that $a = \lambda$ and $b = 2\lambda$. The impact on the results when a and b were varied is discussed later. Simulation results for the improved cloak and that of a cloak with a 10, 50, and 100-term Taylor series approximations for μ_θ are shown in Figure 4.15. Note all cloaks in Figure 4.15 show good cloaking performance. However, it is difficult to

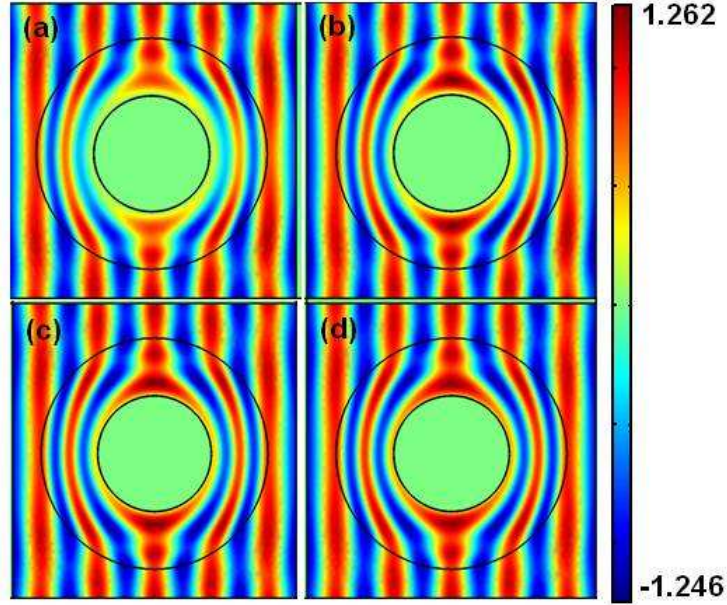


Figure 4.15: Real part of the \hat{z} -component of the total electric field for cloaks with material parameters defined as (a) the improved cloak, while (b), (c), and (d) are cloaks where μ_θ is approximated using a 10, 50, and 100-term Taylor series.

determine which cloak has the best performance. Therefore, only the scattered field outside of the cloaks for each configuration were plotted. These results are shown in Figure 4.16. Figure 4.17 shows the scattered fields from cloaks with the same configurations except that a second order transformation was used when developing the ideal parameter values. Based on the analysis in Section 4.3, the improved cloak should have the largest scattered field while the cloak where μ_θ is approximated using a 100-term Taylor series should have the smallest scattered field for all transformation orders. This is clearly evident in both figures, particularly when one compares the forward scattered fields.

Based on these results, one can conclude the process discussed in Section 4.3 results in material parameter sets that result in better cloak performance as the number of terms in the Taylor series is increased for all transformation orders. However, in order to better classify cloak performance, the near-field results were transformed to the far-field in order to determine each cloak's two-dimensional scattering width.

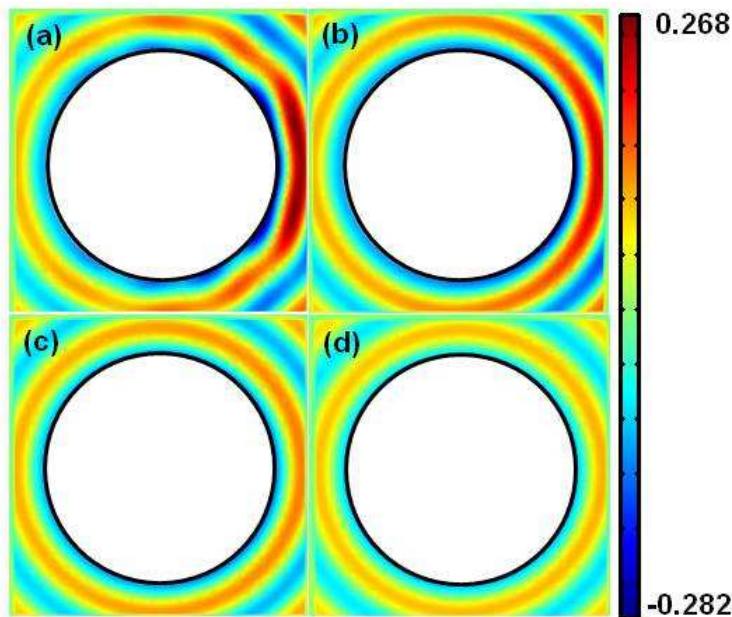


Figure 4.16: Real part of the \hat{z} -component of the scattered electric field for cloaks with material parameters defined as (a) the improved cloak, while (b), (c), and (d) are cloaks where μ_θ is approximated using a 10, 50, and 100-term Taylor series.

In order to compare the cloak's scattering width reduction capabilities, a metric must be established. First the best reduction in scattering width numerically possible was determined. This occurs when an ideal cylindrical cloak is used, theoretically resulting in no scattered field. However, due to numerical issues, there is a residual scattered field. Specifically, the finite element method approximates the field behavior with piecewise continuous elements. Therefore this discretization limits the accuracy of the field representation, particularly near $r = a$ where the cloak has parameter values equal to zero or infinity. Approximations must be made because these values cannot be simulated due to resulting singularities in the differential equation. As stated in Section 4.3, analysis has shown even slight deviations from the ideal material parameters result in degraded cloak performance [42, 77]. To illustrate this degradation, the scattering width for a simulation with no scattering objects in the domain was plotted and compared to the results for an ideally cloaked PEC cylinder. The results are shown in Figure 4.18. Note all plots are normalized by the maximum scattered field magnitude for the uncloaked PEC cylinder. The ideal cloak does

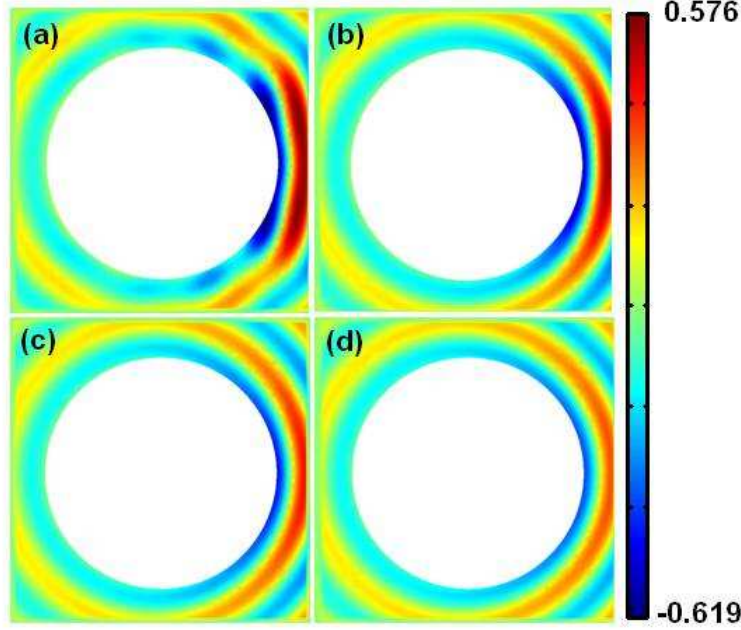


Figure 4.17: Real part of the \hat{z} -component of the scattered electric field for cloaks with material parameters derived using a second order transformation. Images (a), (b), (c), and (d) are cloaks where μ_θ is approximated using a 1, 10, 50, and 100-term Taylor series.

significantly reduce the scattering width of the uncloaked PEC cylinder. However, one would expect the results to be on the order of the scattered field from an empty domain. Clearly, they are not even close to this result due to the aforementioned approximations.

The simulation can be improved by controlling the size of the mesh elements particularly near the region $r = a$. A new simulation domain was constructed by creating a subdomain around $r = a$ of extremely small elements. This increased the resolution with regard to the singular parameter values. The final mesh resulted in approximately 1,500,000 degrees of freedom. At this discretization, the ideal results were -30 dB down from the uncloaked cylinder. Further improvements required significant computation times and would not further aid in the performance analysis as each cloak design is affected equally. Therefore -30 dB is considered to be the ideal solution for comparison purposes.

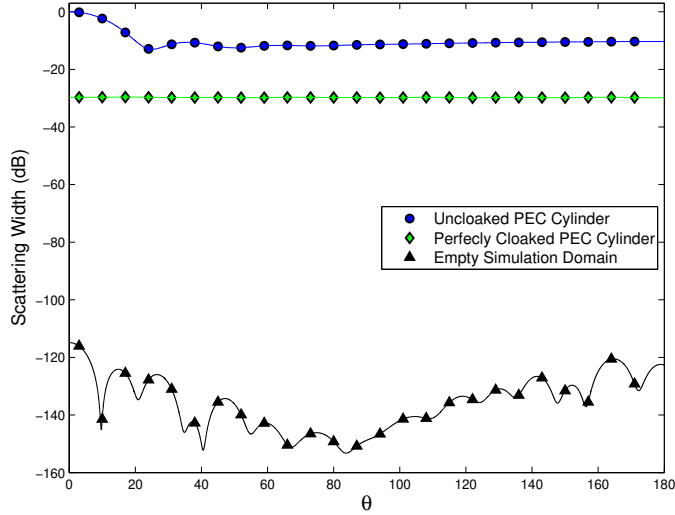


Figure 4.18: Scattering widths for an uncloaked PEC cylinder (\circ -line), ideally cloaked PEC cylinder (\diamond -line), and an empty domain (\triangle -line).

The performance of the improved cloak was compared to cloaks whose material parameters were found using the process described in Section 4.3. Results for the improved cloak and that of a cloak with a 10, 50, and 100-term Taylor series approximations to μ_θ are shown in Figure 4.19. Note even the 10-term Taylor series approximation results in a three dB scattering width improvement in the region near $\theta = 0^\circ$ compared to the improved cloak. Also note the scattering width gets better as more terms in the Taylor series are used, which is expected since the material parameters become the ideal ones as $N \rightarrow \infty$.

In the backscattering region ($\theta = 180^\circ$), improvement towards the ideal solution is extremely slow due to the large slope in the ideal value for μ_θ as $r \rightarrow a$. The Taylor series requires more terms in order to accurately represent μ_θ in this area. It is also interesting to note these new material parameters, although all are spatially varying, are very manufacturable. For example, at $r = a$, $\mu_\theta = 11$ and $\varepsilon_z = 0.3636$ for the 10-term approximation. As the number of terms increases, the values become harder and harder to obtain from a manufacturing perspective ($\mu_\theta = 51$ and $\varepsilon_z = 0.0784$ for 50-term approximation, $\mu_\theta = 101$ and $\varepsilon_z = 0.0396$ for the 100-term approximation). However, as advances in material manufacturing technology continue, these values are

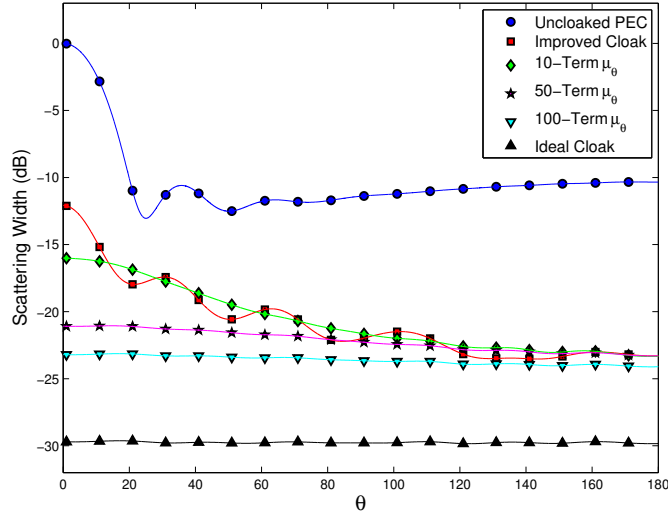


Figure 4.19: Scattering widths for an uncloaked PEC cylinder (\circ -line), and cloaked PEC cylinders using the ideal cloak (\triangle -line), the improved cloak (\square -line), and 10, 50, and 100 term approximations for μ_θ (\diamond , \star , and ∇ -lines).

becoming more approachable. Note similar results are obtained for far field patterns when a second order coordinate transformation is used.

As stated above, all simulations were performed with $\lambda = 1$ meter with the cloak inner and outer boundaries located at $a = \lambda$ and $b = 2\lambda$ respectively. It was shown in [102] the improved cloak is relatively immune to changes in cloak thickness. As shown in Section 4.3, the improved cloak parameters can be derived using the Taylor series expansion method by letting $N = 0$. The material parameter sets developed in this section are refinements to the improved cloak and are derived by increasing N in the Taylor series. Therefore, these new material parameter sets should also be relatively immune to changes in b . A number of simulations were performed with b varying from 1.5λ to 4.5λ . In all simulations, the results were similar to those shown in Figure 4.19. Scattering width results for the geometry when $b = 4.5\lambda$ are shown in Figure 4.20. Note there is a slight degradation in performance as b is increased. When $b = 2\lambda$, the scattering width at $\theta = 0^\circ$ was -16 dB. When b is increased to 4.5λ , the scattering width increased to -14 dB. Hence, a thicker cloak will result in some degradation of performance for the same material parameter set. However, for

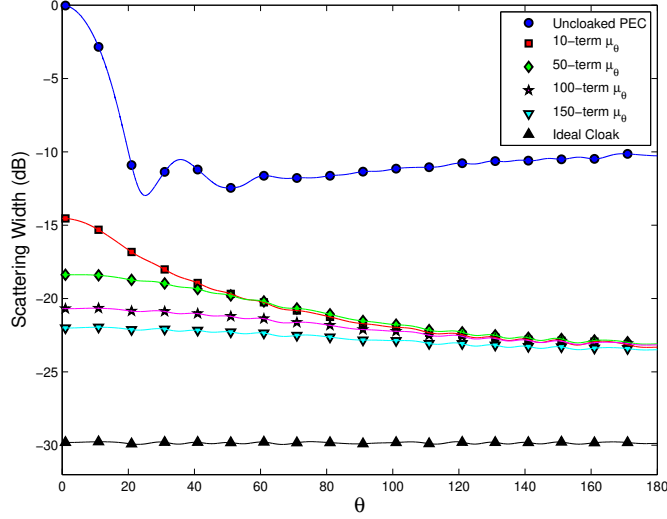


Figure 4.20: Scattering width for cloaks where $b = 4.5\lambda$. Plots show an uncloaked PEC cylinder (\circ -line), an ideally cloaked PEC cylinder (Δ -line), and cloaks for μ_θ approximations using 10, 50, 100, and 150 terms (\square , \diamond , \star , and ∇ -lines).

all values of b , as the number of terms goes to infinity, the performance approaches that of the ideal case, as expected.

4.5 Summary

In this section, a new way to develop simplified material parameter sets for cylindrical cloaks was presented. Specifically, for TM^z incident waves, the approximation of μ_θ should first be defined using a Taylor series expansion of the ideal parameter as defined using all constraint equations. TE^z results are easily obtained by the application of duality. The constitutive parameters μ_r and ε_z can be determined by making the products $\mu_\theta\varepsilon_z$ and $\mu_r\varepsilon_z$ equal to the same products using the ideal material parameter set. The performance of cloaks developed in this manner is limited only by the number of terms used in the Taylor series expansion, which is dictated by existing manufacturing capabilities. Scattering width improvement was observed for all angles when compared to previous published material parameter sets. Significant improvement was noted in the forward scattering region. It was also shown the simplified parameter set put forth in [102] is a simplification of this method in

which the Taylor series expansion of μ_θ is limited to the first term. These parameter sets also have relatively consistent performance for all values of b . Performance for a constant number of terms in the Taylor series does slightly degrade as b increases, but for all b , ideal cloaking performance is approached as $N \rightarrow \infty$.

V. Computational Improvement Using a Green's Function

As discussed in Chapter II, most of the simulations involving cloaks have been done using the Comsol Multiphysics software, a finite-element-based software package. The finite element method is particularly useful to simulate cloaks due to the inhomogeneity of the constitutive parameters. However, there are limitations and trade-offs which must be considered when solving a problem using FEM. FEM partitions a computational domain into a large number of subdomains of simple geometric shapes. The partitioning grid is commonly called the mesh. For two-dimensional problems, triangular elements are commonly used, but there are others. The solution to the differential equation is obtained for each element. Thus, the finer the mesh used when modeling the problem geometry, the more accurate the solution [95]. Some geometries require greater mesh fidelity due to a rapid variation in geometry or spatial parameters. Similarly, simulations with large computational domains require more elements due to the problem size. Larger, denser meshes result in an increased computational burden which can result in long solution times. In this chapter, a Green's function formulation is developed to determine scattering widths from a cylindrically cloaked PEC cylinder. Solution time is significantly reduced when solving for σ_{2D} using the Green's function compared to FEM methods. The tradeoff accompanying the Green's function implementation is the cloak formulation is now limited to a cylindrical geometry with a PEC lining the inner boundary. Changing the cloak geometry would require the derivation of a different Green's function.

5.1 Solution Geometry

Consider the geometry shown in Figure 5.1. A theoretical solution for the PEC cylinder's scattering width when illuminated by an incident TE^z plane wave exists and has the closed form analytic expression shown below [13].

$$\sigma_{2D} = \lim_{r \rightarrow \infty} \frac{2\lambda}{\pi} \left| \sum_{m=0}^{\infty} \epsilon_m \frac{J'_m(k_o a)}{H_m^{(2)'}(k_o a)} \cos(m\theta) \right|^2 \quad (5.1)$$

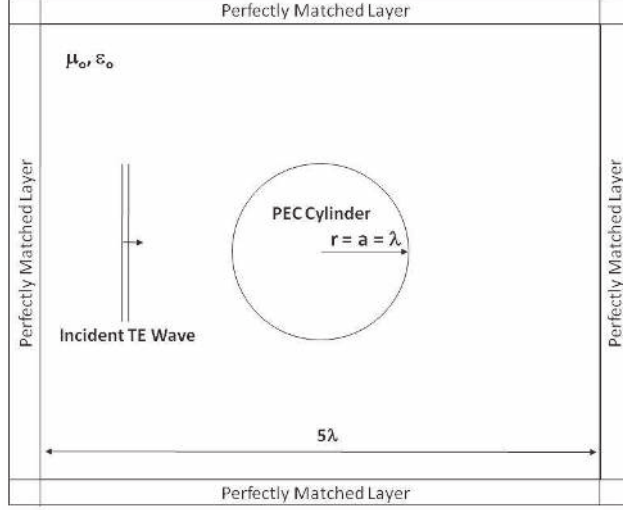


Figure 5.1: Geometry for an FEM simulation of scattering from a PEC cylinder.

In Equation 5.1, k_o is the free space wave number, θ is the observation angle, and ϵ_m is 1 for $m = 0$ and 2 otherwise. Note also that $'$ implies differentiation with respect to r . Obviously Equation 5.1 is an infinite sum, meaning the exact theoretical solution can never be computed using a computer. However, m can be truncated based on the specified level of accuracy. For this work, the summation in Equation 5.1 is truncated to M using the following criteria:

$$x = \max |F_m|, m \in [0, M],$$

$$\forall m > M, |F_m| < 0.01x. \quad (5.2)$$

where $F_m = \frac{J'_m(k_o a)}{H_m^{(2)'}(k_o a)}$ in Equation 5.2. The validity of truncation using Equation 5.2 can be verified by comparing the calculated scattering widths of a PEC cylinder of radius $a = \lambda$ for $m = 10$, which is the determined sum limit based on the criteria in Equation 5.2, and $m = 50$. The metric used to compare the similarity between the solutions is the average difference in σ_{2D} . Mathematically, this is written as

$$\Delta = \frac{1}{M} \sum_{p=1}^M (\sigma_{2D}^A(\theta_p) - \sigma_{2D}^B(\theta_p)), \quad (5.3)$$

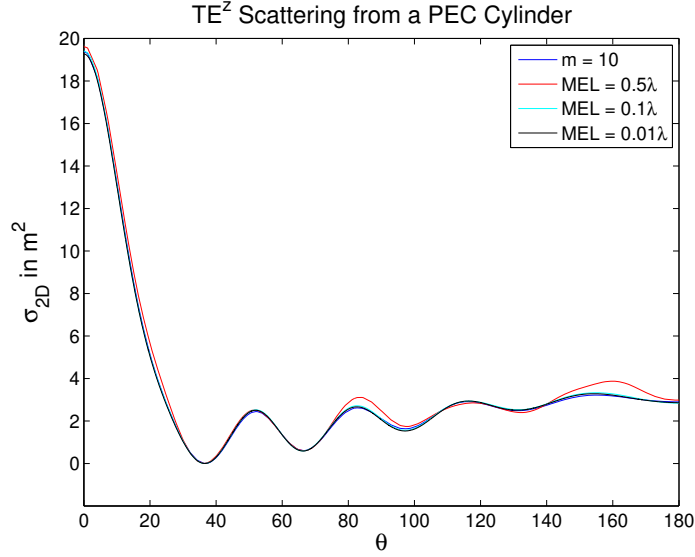


Figure 5.2: Scattering widths for PEC cylinder calculated using analytic and FEM solutions.

where M is the total number of observation angles, and the σ_{2D} terms are the scattering widths which will be compared. Δ for $\sigma_{2D}^A = \sigma_{2D}|_{m=10}$ and $\sigma_{2D}^B = \sigma_{2D}|_{m=50}$ is 0.0063 m^2 . The scattering width for $m = 10$ is plotted in Figure 5.2 (blue line). Note σ_{2D} is on the order of $1 - 20 \text{ m}^2$. Thus, a Δ of 0.0063 m^2 is considered negligible.

The analytic solution in Equation 5.1 can be compared with the FEM solution obtained using the Comsol software. Note the computational boundary is only $5\lambda \times 5\lambda$. As was done in Chapter IV, the near field results obtained using Comsol can be transformed to the far zone to obtain the two-dimensional scattering width. Different meshes were used in the Comsol simulations. A smaller maximum element length (MEL) corresponds to a finer, denser mesh. Simulation results were obtained using seven different meshes. Results are plotted in Figure 5.2 with additional information on problem size and solution speed listed in Table 5.1.

Obviously there is good visual agreement between the analytic and FEM solutions with the only noticeable differences occurring when $\text{MEL} = 0.5\lambda$. However, a metric was needed other than visual alignment to define FEM solution accuracy. Therefore, based on the results in Figure 5.2 and Table 5.1, Δ on the order of 0.1

Table 5.1: Analytic and FEM Solution Comparisons

MEL	Unknowns	Time	$\Delta\sigma_{2D} _{m=10}$
0.5 λ	2,056	0.17 s	0.171 m ²
0.25 λ	3,832	0.23 s	0.125 m ²
0.1 λ	23,146	1.04 s	0.039 m ²
0.075 λ	40,654	1.67 s	0.039 m ²
0.05 λ	92,168	4.02 s	0.043 m ²
0.025 λ	366,024	16.5 s	0.043 m ²
0.01 λ	2,292,872	1,493 s	0.043 m ²

m² was defined as the threshold for good solution agreement. For the geometry in Figure 5.1, an MEL of 0.1 λ is sufficient to obtain good solution agreement. Additional mesh fidelity does not result in better solution agreement, and it also requires significantly longer solution times. As will be seen shortly, there are cloak geometries where an MEL = 0.1 λ does not result in sufficient mesh fidelity due to the thinness of subdomains within the computation region.

5.2 Green's Function for a Layered PEC Cylinder

Green's functions are routinely used in electromagnetic scattering problems. However, they have not been applied to solve radiation problems involving cloaks, likely due to the difficulty in their derivation due to the anisotropic nature of a cloak's material parameters. As discussed in Section 2.4, a cylindrical cloak can be approximated by using concentric layers of isotropic material with homogeneous permittivity and permeability. Therefore, a Green's function for a magnetic line source in the far zone radiating in the presence of a PEC cylinder of radius $r = a$ covered by n layers of homogeneous material approximates a TE^z plane wave incident on a cloaked cylinder. This geometry is shown in Figure 5.3. Once the Green's function is known, the total field can be found by

$$\vec{H}^{TOT} = -\frac{k_o^2}{4\omega\mu_o} I_m \vec{I} \cdot \vec{G}, \tag{5.4}$$

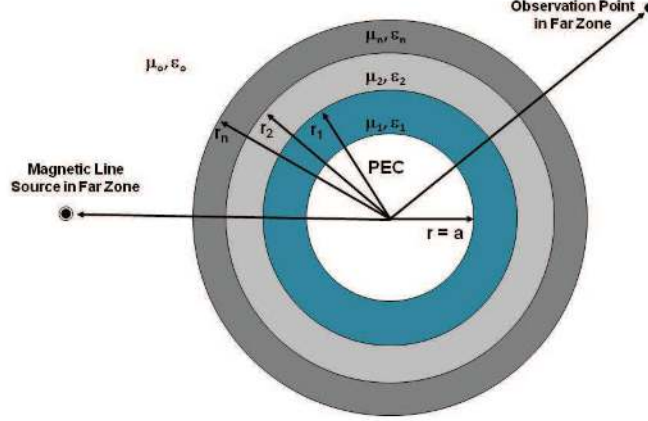


Figure 5.3: Problem geometry for Green's function derivation

where I_m is the strength of the magnetic line source, \vec{I} is the unit dyad, and \vec{G} is the Green's function.

The derivation of such a Green's function is not a new concept. Methods similar to what is proposed here have been used to study near and far field solutions for a PEC cylinder covered by isotropic lossless materials [10,103]. However, these analyses focused on the scattering properties of PEC cylinders layered with double negative materials.

A Green's function for the geometry shown in Figure 5.3 was derived using the method described in [23] with the details shown in Appendix B. A Green's function for a magnetic line source radiating in the presence of a PEC cylinder with n layers of homogeneous, isotropic material has the form:

$$\vec{G} = -\frac{j}{4} \sum_{m=0}^{\infty} \epsilon_m \cos [m(\theta - \theta')] \left[J_m(k_o r_{<}) + \frac{B_m^{n+1}}{A_m^{n+1}} H_m^{(2)}(k_o r_{<}) \right] H_m^{(2)}(k_o r_{>}), \quad (5.5)$$

$$A_m^{n+1} = 1, \quad (5.6)$$

$$B_m^1 = -\frac{J'_m(k_1 a)}{H_m^{(2)'}(k_1 a)}, \quad (5.7)$$

Note that $r_{<}$, $r_{>}$ are the lesser and greater of r and r' respectively, and θ , θ' are the observation and source angular locations. The remaining unknowns in Equation 5.5

are the B_m^{n+1} coefficients. These coefficients are determined based on the junction conditions at the radial boundaries which force continuity of tangential magnetic and electric fields. Due to the PEC boundary at $r = a$, the B_m^1 value is known, which allows the remaining values to be found by solving a system of equations of the form $Ax = B$, where A is a $2n \times 2n$ matrix, and n is the number of layers surrounding the PEC (see Appendix B for details). Note Equation 5.5 is valid when observing the field where $r > r_n$ i.e. in the free space region.

Equation 5.5 contains components for the incident field and the scattered field. The incident field is represented by the $J_m(k_o r_<)$ component while the scattered field is represented by the $H_m^{(2)}(k_o r_<)$ terms. Thus, the Green's function can be rewritten as two separate functions. This is done because the goal is to compute σ_{2D} and compare the result obtained using a Green's function formulation to the result obtained using an FEM-based method (Comsol). Also, without loss of generality, the magnetic line source is assumed to be at $\theta' = 180^\circ$ in the far zone, which results in a plane wave traveling in the \hat{x} direction. Hence, the Green's function for the incident field can first be written as

$$\bar{G}^i = -\frac{j}{4} \sum_{m=0}^{\infty} \epsilon_m (-1)^m \cos(m\theta) J_m(k_o r) H_m^{(2)}(k_o r'). \quad (5.8)$$

The large argument approximation for the Hankel function [7] can then be used to simplify the expression. This is done because the line source is assumed to be in the far zone in order for plane wave incidence.

$$H_m^{(2)}(k_o r') \rightarrow j^m \sqrt{\frac{2}{\pi k_o}} \frac{e^{-jk_o r'}}{\sqrt{r'}} e^{j\frac{\pi}{4}} \quad (5.9)$$

The following is defined for simplicity of writing.

$$H_o = \sqrt{\frac{2}{\pi k_o}} \frac{e^{-jk_o r'}}{\sqrt{r'}} e^{j\frac{\pi}{4}} \quad (5.10)$$

Hence, the Green's function for the incident field at the surface of the layered PEC cylinder ($r = b$) is

$$\bar{G}^i = -\frac{j}{4}H_o \sum_{m=0}^{\infty} \epsilon_m (-j)^m \cos(m\theta) J_m(k_o b). \quad (5.11)$$

Similarly, the Green's function for the scattered field can be represented as

$$\bar{G}^s = -\frac{j}{4}H_o \sum_{m=0}^{\infty} \epsilon_m (-j)^m \cos(m\theta) \frac{B_m^{n+1}}{A_m^{n+1}} H_m^{(2)}(k_o r). \quad (5.12)$$

The large argument approximation for the Hankel function can again be applied since the ultimate goal is to calculate σ_{2D} .

$$\bar{G}^s = -\frac{j}{4}H_o \sqrt{\frac{2}{\pi k_o}} \frac{e^{-jk_o r}}{\sqrt{r}} e^{j\frac{\pi}{4}} \sum_{m=0}^{\infty} \epsilon_m \cos(m\theta) \frac{B_m^{n+1}}{A_m^{n+1}} \quad (5.13)$$

In general, scattering width can be found by

$$\sigma_{2D} = \lim_{r \rightarrow \infty} 2\pi r \frac{|H^s|^2}{|H^i|^2}. \quad (5.14)$$

Therefore, the scattering width for a layered PEC cylinder with an incident TE^z plane wave traveling in the positive \hat{x} direction is

$$\sigma_{2D} = \frac{2\lambda}{\pi} \frac{\left| \sum_{m=0}^{\infty} \epsilon_m \cos(m\theta) \frac{B_m^{n+1}}{A_m^{n+1}} \right|^2}{\left| \sum_{m=0}^{\infty} \epsilon_m (-j)^m \cos(m\theta) J_m(k_o b) \right|^2}. \quad (5.15)$$

The summation in Equation 5.15 is truncated to $m = M$ using the criteria put forth in Equation 5.2. The closed form analytic solution for σ_{2D} can be used to solve for the scattering width from a layered PEC cylinder.

5.3 FEM and Green's Function Comparison

Since it is not yet possible to manufacture cloaks with the required spatially varying anisotropic parameters, concentric rings of *anisotropic* material are used to approximate the spatial variation [79]. Such a realization can be simulated in Comsol, but the thinness of the layers necessitates more elements resulting in an increased computational burden, as will be shown below. Two thin layers of homogeneous *isotropic* material can be used to approximate the anisotropic concentric rings. This geometry approximation can be quickly solved using the Green's function implementation.

Consider a two-dimensional ideal cylindrical cloak with material parameters, repeated below for convenience.

$$\varepsilon_r = \frac{r-a}{r}, \quad \varepsilon_\theta = \frac{r}{r-a}, \quad \mu_z = \frac{r-a}{r} \left(\frac{b}{b-a} \right)^2 \quad (5.16)$$

In order to manufacture this cloak, concentric rings of anisotropic material would be required to approximate the spatial variation, much like what was done in [79]. Based on the results in [40], the anisotropic concentric rings can be approximated by using thin layers of homogeneous isotropic material. Recall from Section 2.4, the required material parameters for the layers approximating the anisotropic layer are

$$\varepsilon_\theta = \frac{\varepsilon_1 + \eta\varepsilon_2}{1 + \eta}, \quad (5.17)$$

$$\frac{1}{\varepsilon_r} = \frac{1}{1 + \eta} \left(\frac{1}{\varepsilon_1} + \frac{\eta}{\varepsilon_2} \right). \quad (5.18)$$

As an example, consider an ideal cloak realized using ten layers of concentric anisotropic rings. Twenty layers of homogeneous, isotropic rings can be used to simulate the ten-layer anisotropic cloak. The values of ε_r , ε_θ , and μ_z for each anisotropic ring are determined by evaluating Equation 5.16 at each of the ten layers ($r = r_n$). The permittivity values for the isotropic layers are then determined by substituting

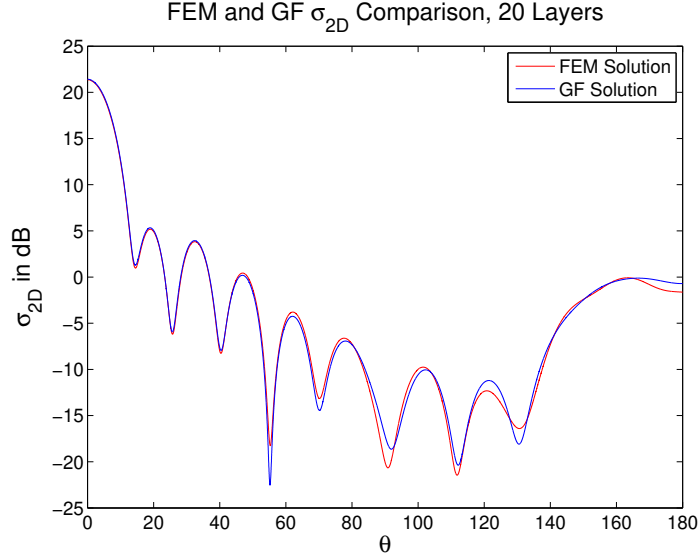


Figure 5.4: Green’s function and FEM results comparison for PEC with 20 layers the values for ε_r and ε_θ into Equations 5.17 and 5.18. The value of μ_z is determined by evaluating μ_z given in Equation 5.16 at $r = r_n$.

A 20-layer isotropic approximation of the ideal cloak surrounding a PEC cylinder was simulated using Comsol. Scattering width values were determined based on Comsol results. Analytic results were found using Equation 5.15. All results are shown in Figure 5.4. Additionally, results from the two methods for a simulation using 40 layers of isotropic material to simulate a 20-layer cloak of anisotropic concentric rings approximating an ideal cloak were computed. These are shown in Figure 5.5.

Note the similarities between the Comsol and Green’s function solutions. For the 20-layer results, Δ was 0.14 m^2 , which shows good agreement between the two solutions. However, there is a noticeable difference in computation time. The Green’s function solution took 2.28 s. The Comsol solution was obtained by first creating a non-uniform mesh over the computational domain. This was necessary because the spacing between layers was only 0.05λ and 0.025λ for the 20 and 40-layer simulations respectively, and a uniform mesh with $\text{MEL} < 0.01\lambda$ was not possible due to memory limitations of the Dell 690 precision work station with eight gigabytes of RAM. The

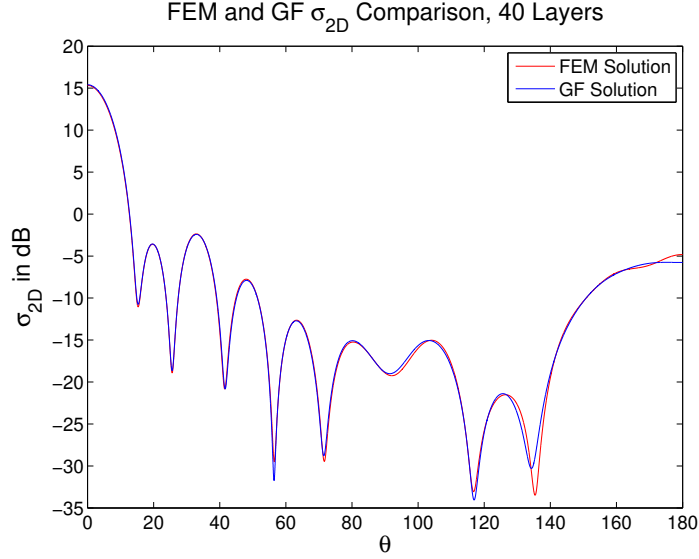


Figure 5.5: Green’s Function and FEM Results Comparison for PEC with 40 Layers

MEL in the concentric layers was limited to 0.007λ , while for the rest of the computational domain, $\text{MEL} = 0.05\lambda$. For the 20-layer FEM simulation, the mesh had 911,004 elements and a solution time of 125 s.

The 40-layer simulation resulted in a Δ of 0.04 m^2 . The Green’s function solution time was 2.82 s. The Comsol solution used a similar non-uniform mesh with 881,892 elements and had a solution time of 124 s. Obviously, the Green’s function method is faster, particularly if a number of simulations are to be performed to conduct an optimization or an error analysis based on parameter or thickness variations in the layers. Additionally, if more layers are to be used, an FEM solution will require finer meshing within the layers, increasing the number of unknowns which will increase solution time.

Another benefit of using the Green’s function to calculate scattering widths is when large cloak geometries are simulated. Up until this point, all previous simulations in this section have used the cloak parameters such that $a = \lambda$ and $b = 2\lambda$. If a and b are increased, the computational domain in an FEM simulation increases. This will increase the number of unknowns if the same limits on MEL are used, ultimately resulting in a longer solution time. The MEL can be increased in order to prevent out-

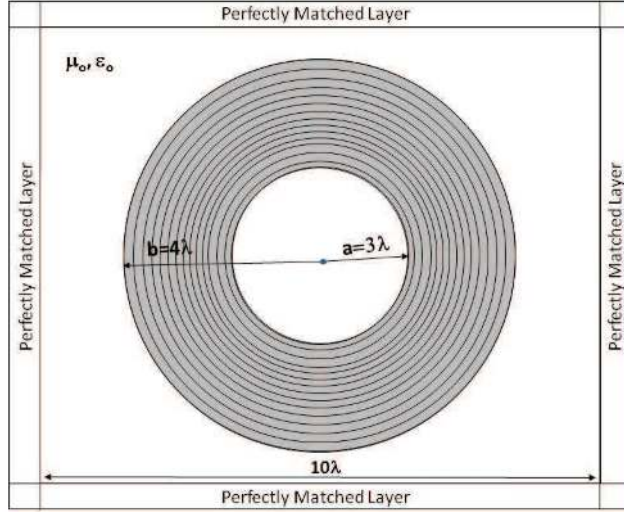


Figure 5.6: Larger computational domain

of-memory errors during solution at the penalty of reduced accuracy. Increasing the cloak radii in the Green's function does result in having to include more terms in the summation due to the constraints of Equation 5.2, but this increase in computational budget is minimal compared to the increased burden in an FEM simulation.

As an example, consider the simulation geometry shown in Figure 5.6. More elements are going to be needed since the computational domain is $10\lambda \times 10\lambda$. A simulation of a 20-layer cloak of homogeneous material approximating the material parameters shown Equation 5.16 was performed using Comsol, with scattering width results obtained and compared to results using the Green's function formulation. These results are shown in Figure 5.7. The Δ between the two simulations was 1.39 m^2 , much larger than the 0.1 m^2 threshold. As before, a non-uniform mesh was applied to prevent out-of-memory errors. The MEL for the layers was 0.01λ , while for the remaining areas, $\text{MEL} = 0.3\lambda$. Note the MEL has been increased compared to the same 20-layer simulation where $a = \lambda$ and $b = 2\lambda$, meaning FEM solution accuracy will decrease. This had to be done due to the increase in the size of the computational domain. The resulting mesh consisted of 972,698 elements and resulted in a solution time of 116 s. In addition to the solution time, Comsol took 168 s to simply create the mesh. Further increases in cloak size resulted in having to significantly increase

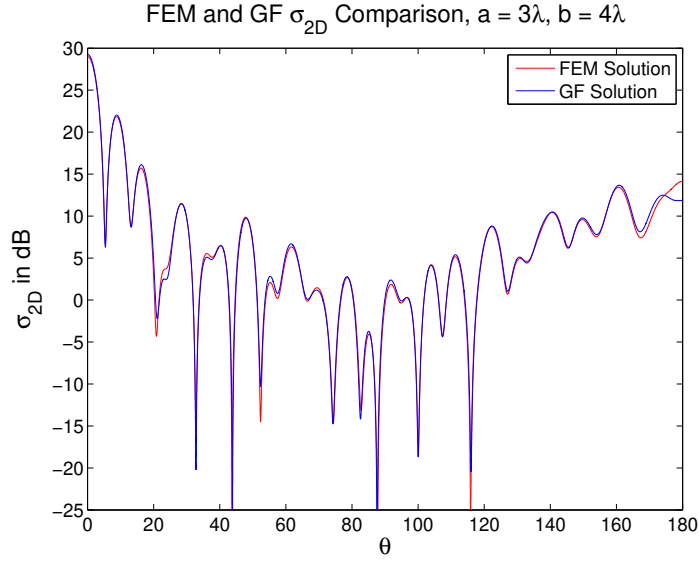


Figure 5.7: σ_{2D} for larger cylinder and cloak size

MEL in order prevent mesh size from growing beyond the computational capabilities. The increase in problem geometry had little impact on the Green’s function solution. The solution time did increase due to the increase in the number of terms in the summation, but the solve time was only 3.89 s. The Green’s function proved to be much less computationally intensive for larger problem sizes

Obviously a Green’s function approach for determining scattering widths from a cylindrical cloak results in a significant computational savings. The computational domain size is directly related to the cylindrical cloaks’s radius in that a larger cloak results in a larger domain size. The increase in computational domain requires either a longer solution time due to the increased number of elements or a reduction in mesh density which impacts solution accuracy. The Green’s function implementation is much faster than an FEM solution and is more adept at handling problem geometries which require denser meshes or have larger computation domains.

5.4 Summary

This chapter presented a Green’s function implementation used to solve for the far zone scattered field from a two-dimensional cylindrical cloak. The Green’s function

implementation used the fact thin, concentric, isotropic, homogeneous layers could be used to realize a cloak's anisotropic properties. The Green's function implementation was shown to be considerably faster when solving for the scattered field compared to FEM solutions particularly for larger computational domains. This benefit is at the expense of being constrained to a cylindrical geometry. A different Green's function would have to be derived for a different cloak shape.

VI. Metamaterial Eigenfrequency Decomposition

Metamaterials are the building blocks for many of the applications defined by transformation optics. Transformation optics defines a material's constitutive parameters necessary to achieve a desired electromagnetic field behavior. As discussed in Chapter III, the unit cells which make up a metamaterial are designed to interact with the electromagnetic fields, resulting in a desired electric or magnetic effect (or in some cases both). The unit cell metallizations are first designed with knowledge of these field interactions, but ultimately, simulations are required to measure the exact resonant frequency of the devices. This results in an empirical catalogue of measurements which help determine how changes in various unit cell design parameters affect the resonant frequencies.

Fischer *et al.* used an eigendecomposition to design substrates for patch antennas [31]. The eigendecomposition identifies the individual eigenfrequencies of a structure. These eigenfrequencies can then be correlated to the device characteristics, whether it be geometry or material property. Fischer *et al.* used this information to manipulate eigenfrequency location by changing the material properties of the device. This resulted in an increased bandwidth for the antennas. A similar eigendecomposition design method could be applied to metamaterial unit cells. This initial investigation determined the eigendecomposition algorithm is applicable to metamaterial unit cell designs. What follows is a description of the process as it applies to metamaterials using the Comsol Multiphysics software package.

6.1 *Comsol and the Finite Element Method*

The Comsol Multiphysics software package is used to obtain all FEM solutions in this chapter. Therefore, it was necessary to understand exactly how Comsol implements the finite element method to solve three dimensional electromagnetics problems. Vector basis functions (also known as edge elements) are used within each element to approximate the unknown [27]. A description and derivation of the gen-

eral form for the vector basis functions within a tetrahedral subdomain is given in Appendix C.

The governing partial differential equation which Comsol solves is the vector wave equation. This can easily be derived from Maxwell's Equations. Assuming a source free domain, Maxwell's equations are

$$\nabla \times \vec{E} = -j\omega\mu\vec{H}, \quad (6.1)$$

$$\nabla \times \vec{H} = j\omega\varepsilon\vec{E}. \quad (6.2)$$

The electric field vector wave equation can be developed by taking the curl of Equation 6.1, and substituting the expression for $\nabla \times \vec{H}$ from Equation 6.2 into this expression. The result is

$$\nabla \times \left(\frac{\nabla \times \vec{E}}{\mu_r} \right) - k_o^2 \varepsilon_r \vec{E} = 0. \quad (6.3)$$

The first vector Green's theorem can be used to develop the weak form of the above equation [95]

$$\int_{V^e} \frac{\nabla \times \vec{E} \cdot \nabla \times \vec{W}_i}{\mu_r} dV - k_o^2 \int_{V^e} \varepsilon_r \vec{E} \cdot \vec{W}_i dV = 0, \quad (6.4)$$

where the \vec{W}_i terms are test functions.

The FEM approximates \vec{E} within each geometric element using vector basis functions. For this work, tetrahedral elements are used, which results in six vector basis functions per tetrahedral. Within each element, the electric field is approximated as

$$\vec{E} \cong \sum_{j=1}^6 \vec{N}_j^e E_j^e. \quad (6.5)$$

The unknowns are the E_j^e terms. These are found by formulating a system of equations which allows the unknowns to be found. The system of equations is formed by first taking the dot-product of each vector basis function with the wave equation, and

integrating the result over the volume of the tetrahedral element.

$$\sum_{i=1}^6 \left(\int_{V^e} \nabla \times \left(\frac{\nabla \times \vec{E}}{\mu_r} \right) \cdot \vec{N}_i dV - k_o^2 \int_{V^e} \varepsilon_r \vec{E} \cdot \vec{N}_i dV \right) = 0 \quad (6.6)$$

Additionally, the test functions, \vec{W}_i , are defined to be the same as the vector basis functions i.e $\vec{W}_i = \vec{N}_i$. Finally, replacing \vec{E} in Equation 6.6 with the approximation in Equation 6.5 yields

$$\sum_{i=1}^6 \sum_{j=1}^6 \int_{V^e} \frac{\nabla \times E_j^e \vec{N}_j \cdot \nabla \times \vec{N}_i^e}{\mu_r} dV - k_o^2 \int_{V^e} \varepsilon_r E_j^e \vec{N}_j \cdot \vec{N}_i^e dV = 0. \quad (6.7)$$

The E_j^e 's are constant coefficients and can be removed from the integration. Additionally, the dot-product is commutative; thus, the order can be reversed. The final equation is

$$\sum_{i=1}^6 \sum_{j=1}^6 \left(E_j^e \int_{V^e} \frac{\nabla \times \vec{N}_i^e \cdot \nabla \times \vec{N}_j^e}{\mu_r} dV - k_o^2 E_j^e \int_{V^e} \varepsilon_r \vec{N}_i^e \cdot \vec{N}_j^e dV \right) = 0. \quad (6.8)$$

Note that each integral can be evaluated analytically. Additionally, within each element, μ_r and ε_r are assumed to be homogeneous and can be removed from the integration. The curl terms can be evaluated based on the following [46]:

$$\begin{aligned} \vec{N}_i^e &= \vec{W}_{i_1 i_2} l_i^e, \\ \nabla \times \vec{W}_{i_1 i_2} &= 2\nabla L_{i_1}^e \times \nabla L_{i_2}^e. \end{aligned} \quad (6.9)$$

The l_i^e represent the length of the i^{th} edge of each element (Appendix C has further details). The linear interpolation functions, $L_{i_1}, L_{i_2}, i = 1, 2, 3, 4$, are defined as

$$L_i^e = \frac{1}{6V^e} (a_i^e + b_i^e x + c_i^e y + d_i^e z), \quad (6.10)$$

where $\bar{a}_i^e, \bar{b}_i^e, \bar{c}_i^e$, and \bar{d}_i^e are constants defined in Appendix C. The gradients in Equation 6.9 are

$$\nabla L_i^e = \frac{1}{6V^e} (\bar{b}_i^e \hat{x} + \bar{c}_i^e \hat{y} + \bar{d}_i^e \hat{z}), \quad (6.11)$$

and the curl, $\nabla \times \vec{N}_i^e$, can be written as

$$\nabla \times \vec{N}_i^e = \frac{2l_i^e}{(6V^e)^2} [(c_{i_1}^e d_{i_2}^e - c_{i_2}^e d_{i_1}^e) \hat{x} + (b_{i_2}^e d_{i_1}^e - b_{i_1}^e d_{i_2}^e) \hat{y} + (b_{i_1}^e c_{i_2}^e - b_{i_2}^e c_{i_1}^e) \hat{z}]. \quad (6.12)$$

Based on this result, it is possible to write the result for the dot product of the two curls as

$$\begin{aligned} \nabla \times \vec{N}_i^e \cdot \nabla \times \vec{N}_j^e &= \frac{4l_i^e l_j^e}{(6V^e)^4} [(c_{i_1}^e d_{i_2}^e - c_{i_2}^e d_{i_1}^e) (c_{j_1}^e d_{j_2}^e - c_{j_2}^e d_{j_1}^e) + \\ & (b_{i_2}^e d_{i_1}^e - b_{i_1}^e d_{i_2}^e) (b_{j_2}^e d_{j_1}^e - b_{j_1}^e d_{j_2}^e) + (b_{i_1}^e c_{i_2}^e - b_{i_2}^e c_{i_1}^e) (b_{j_1}^e c_{j_2}^e - b_{j_2}^e c_{j_1}^e)]. \end{aligned} \quad (6.13)$$

The above are all constants. Thus, the following is the result for the first integral.

$$\begin{aligned} \frac{1}{\mu_r} \int_{V^e} \nabla \times \vec{N}_i^e \cdot \nabla \times \vec{N}_j^e dV &= \frac{4l_i^e l_j^e V^e}{(6V^e)^4 \mu_r} [(c_{i_1}^e d_{i_2}^e - c_{i_2}^e d_{i_1}^e) (c_{j_1}^e d_{j_2}^e - c_{j_2}^e d_{j_1}^e) + \\ & (b_{i_2}^e d_{i_1}^e - b_{i_1}^e d_{i_2}^e) (b_{j_2}^e d_{j_1}^e - b_{j_1}^e d_{j_2}^e) + (b_{i_1}^e c_{i_2}^e - b_{i_2}^e c_{i_1}^e) (b_{j_1}^e c_{j_2}^e - b_{j_2}^e c_{j_1}^e)] \end{aligned} \quad (6.14)$$

A similar procedure can be done to determine $\vec{N}_i^e \cdot \vec{N}_j^e$. The vector basis functions are related to the linear interpolation functions by [46]

$$\vec{N}_i^e = l_i^e (L_{i_1} \nabla L_{i_2} - L_{i_2} \nabla L_{i_1}). \quad (6.15)$$

Therefore, \vec{N}_i^e and \vec{N}_j^e can be expressed as

$$\begin{aligned} \vec{N}_i^e &= \frac{l_i^e}{6V^e} [(L_{i_1} b_{i_2} - L_{i_2} b_{i_1}) \hat{x} + (L_{i_1} c_{i_2} - L_{i_2} c_{i_1}) \hat{y} + (L_{i_1} d_{i_2} - L_{i_2} d_{i_1}) \hat{z}], \\ \vec{N}_j^e &= \frac{l_j^e}{6V^e} [(L_{j_1} b_{j_2} - L_{j_2} b_{j_1}) \hat{x} + (L_{j_1} c_{j_2} - L_{j_2} c_{j_1}) \hat{y} + (L_{j_1} d_{j_2} - L_{j_2} d_{j_1}) \hat{z}]. \end{aligned} \quad (6.16)$$

The dot product can be expressed by the following. First let

$$f_{ij} = b_i^e b_j^e + c_i^e c_j^e + d_i^e d_j^e \quad (6.17)$$

Then the dot product is

$$\vec{N}_i \cdot \vec{N}_j = \frac{l_i^e l_j^e}{(6V^e)^2} [L_{i_1} L_{i_2} f_{i_2 j_2} - L_{i_1} L_{j_2} f_{i_2 j_1} - L_{i_2} L_{j_1} f_{i_1 j_2} + L_{i_2} L_{j_2} f_{i_1 j_1}] \quad (6.18)$$

Note the L_i terms are functions of position. Therefore, the evaluation of the second integral is slightly more complicated. The following formula can be used [46].

$$\int_{V^e} (L_1^e)^k (L_2^e)^l dV = \frac{k!l!}{(k+l+3)!} 6V^e \quad (6.19)$$

As an example, consider $\vec{N}_1^e \cdot \vec{N}_1^e$.

$$\vec{N}_1^e \cdot \vec{N}_1^e = \frac{(l_1^e)^2}{(6V^e)^2} [L_1 L_2 f_{22} - L_1 L_2 f_{21} - L_2 L_1 f_{12} + L_2 L_2 f_{11}] \quad (6.20)$$

Therefore, the second integral for the case where $i = 1$ and $j = 1$ can be written as

$$\begin{aligned} k_o^2 \varepsilon_r \int_{V^e} \vec{N}_1^e \cdot \vec{N}_1^e dV^e &= \frac{k_o^2 \varepsilon_r (l_1^e)^2}{(6V^e)^2} [f_{22} \int_{V^e} (L_1)^2 dV - \\ & f_{21} \int_{V^e} L_1 L_2 dV - f_{12} \int_{V^e} L_2 L_1 dV + f_{11} \int_{V^e} (L_2)^2 dV] . \end{aligned} \quad (6.21)$$

Using the integration formula and noting $f_{12} = f_{21}$, the result is

$$k_o^2 \int_{V^e} \varepsilon_r \vec{N}_1^e \cdot \vec{N}_1^e dV^e = \frac{k_o^2 \varepsilon_r (l_1^e)^2}{360V^e} [f_{11} - f_{12} + f_{22}] \quad (6.22)$$

It is possible to analytically integrate both integrals in Equation 6.8. Therefore, a system of equations can be formulated such that the unknown terms, E_j^e , can be determined. Care must be taken when constructing the global matrices, as elements share edges. Knowing the method used to construct these matrices was not important to this effort. Knowing the formulation was important and verified as such in the next section.

6.2 Cmsol Formulation Verification

As discussed above, the FEM converts a partial differential equation into a matrix problem. The matrix elements consist of two parts: those dependent on the permeability and those dependent on permittivity. Specifically, examining Equation 6.8, it is possible to define the following:

$$A_{ij}^{(1)} = \frac{1}{\mu_r} \int_{V^e} \nabla \times \vec{N}_i^e \cdot \nabla \times \vec{N}_j^e dV, \quad (6.23)$$

$$A_{ij}^{(2)} = -k_o^2 \varepsilon_r \int_{V^e} \vec{N}_i \cdot \vec{N}_j dV. \quad (6.24)$$

The complete impedance matrix, A , is defined as

$$A = A^{(1)} + A^{(2)}. \quad (6.25)$$

It was vital to be able to access the matrices defined in Equations 6.23 and 6.24. However, in its default settings, Cmsol provides access to only the complete impedance matrix. The $A^{(1)}$ matrix could be obtained by setting all domain permittivities to zero, effectively eliminating the $A^{(2)}$ contribution. The $A^{(2)}$ matrix could then be found by first solving for A and then subtracting the $A^{(1)}$ matrix.

The $A^{(2)}$ matrix could also be directly evaluated by manually modifying the partial differential equation which Cmsol uses to generate the system of equations [34]. Effectively, the governing weak form of the partial differential equation was changed to

$$-k_o^2 \int_{V^e} \varepsilon_r \vec{E} \cdot \vec{N}_i dV = 0. \quad (6.26)$$

Note Equation 6.26 is scaled by k_o^2 . Therefore, checking the validity of the $A^{(2)}$ matrix was possible. Doubling k_o resulted in each term in the $A^{(2)}$ matrix being scaled by a factor of four. Additionally, the $A^{(2)}$ matrix obtained by altering the equation system was compared to that obtained by simply solving for the difference of A and $A^{(1)}$.

The results were the same to within 10^{-10} for various test cases. Therefore, it was concluded the correct $A^{(1)}$ and $A^{(2)}$ matrices could be obtained from Comsol.

6.3 Eigendecomposition

A standard FEM formulation will solve a system of equations of the form

$$[A^{(1)}(k) + A^{(2)}(k)][E(k)] = [f(k)], \quad (6.27)$$

where $[E(k)]$ are the unknowns, $[f(k)]$ is some forcing function, and k is the wave number of the excitation. Note wave number is directly related to frequency.

The impedance matrix, A , has two components, $A^{(1)}$ and $A^{(2)}$. Note from Equations 6.23 and 6.24 that $A^{(1)}$ is independent of frequency (k), while $A^{(2)}$ is dependent on it. Hence, a normalized wave number, \tilde{k} , can be defined as [32]

$$\tilde{k} = \frac{k}{k_o}. \quad (6.28)$$

Equation 6.28 can be used to write an equivalent expression for Equation 6.27.

$$[A^{(1)}(k_o) + \tilde{k}A^{(2)}(k_o)][E(k)] = [f(k)] \quad (6.29)$$

The unknowns in Equation 6.29 can be found by

$$[E(k)] = [A^{(1)}(k_o) + \tilde{k}A^{(2)}(k_o)]^{(-1)}[f(k)]. \quad (6.30)$$

The normalized eigenfrequencies are those values of \tilde{k} which make the matrix inversion on the right side of Equation 6.30 impossible. The eigenfrequencies can be analytically found using the method put forth by Fischer *et al.* First an eigendecomposition on the $A^{(1)}$ and $A^{(2)}$ matrices is performed.

$$X\Lambda X^{(-1)} = [A^{(2)}(k_o)]^{(-1)}A^{(1)}(k_o) \quad (6.31)$$

X is a matrix whose columns are the eigenvectors while Λ is a diagonal matrix whose elements are the eigenvalues. An equivalent expression for Equation 6.30 can be written using the eigendecomposition.

$$[E(k)] = \left[\tilde{k}^2 \vec{I} + X \Lambda X^{(-1)} \right]^{(-1)} [A^{(2)}(k_o)]^{(-1)} [f(k)] \quad (6.32)$$

The \vec{I} term is the identity matrix. Equation 6.32 can be rewritten by defining

$$\Lambda_{\tilde{k}} = \Lambda + D(\tilde{k}^2), \quad (6.33)$$

where $D(\tilde{k}^2)$ is a diagonal matrix with elements \tilde{k}^2 . Therefore, an equivalent form for Equation 6.30 is [32]

$$[E(k)] = X \Lambda_{\tilde{k}}^{(-1)} X^{(-1)} [A^{(2)}(k_o)]^{(-1)} [f(k)]. \quad (6.34)$$

Note that $X \Lambda_{\tilde{k}}^{(-1)} X^{(-1)} [A^{(2)}(k_o)]^{(-1)}$ is resonant at $\tilde{k}_i = \sqrt{-Re(\lambda_i)}$. This is because the elements of the diagonal matrix $\Lambda_{\tilde{k}}$ are $\lambda_i + \tilde{k}^2$. Therefore, by defining \tilde{k}_i as such, there becomes a zero on the diagonal of the $\Lambda_{\tilde{k}}$ matrix, making it noninvertible or resonant [31]. Thus, the eigenfrequencies for Equation 6.29 can be determined.

6.4 Eigendecomposition Verification

In order to verify the Comsol-generated $A^{(1)}$ and $A^{(2)}$ matrices could be used to identify the eigenfrequencies for structures by the method described in the previous section, a simple test case was performed. A rectangular cavity as shown in Figure 6.1 has easily determined eigenvalues. When PEC boundary conditions are applied to all six faces, the TE^z eigenvalues are given by [13]

$$(f_r)_{mnp} = \frac{1}{2\pi\sqrt{\mu\epsilon}} \sqrt{\left(\frac{m\pi}{a}\right)^2 + \left(\frac{n\pi}{b}\right)^2 + \left(\frac{p\pi}{c}\right)^2}, \quad (6.35)$$

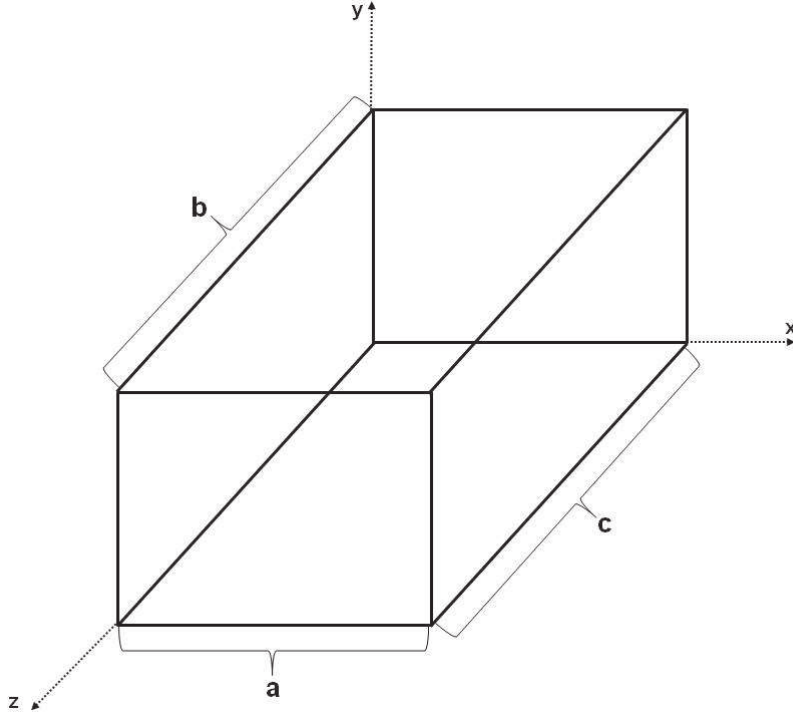


Figure 6.1: PEC Rectangular Resonator Geometry

where $m = 0, 1, 2, \dots$, $n = 0, 1, 2, \dots$, $p = 1, 2, 3, \dots$ and $m = n \neq 0$. The TM^z modes are given by the same equation with the exception that $m = 1, 2, 3, \dots$, $n = 1, 2, 3, \dots$, and $p = 0, 1, 2, \dots$

A PEC rectangular resonator as shown in Figure 6.1 was created in Comsol where $a = 0.02286$ m, $b = 0.01016$ m, and $c = 0.1143$ m. The eigenfrequencies were extracted using the method described in the previous section. These are plotted in Figure 6.2. The top graph shows all extracted eigenfrequencies while the bottom graph zooms in to the region where the eigenfrequencies from 6 - 20 GHz are shown. For the rectangular resonator shown in Figure 6.1 with values previously defined for a , b , and c , the theoretically calculated eigenfrequencies were compared to the extracted eigenfrequencies. These results are shown in Table 6.1. The extracted eigenfrequencies matched the theoretical values to within 0.25% for all 21 eigenfrequencies less than 16 GHz. Above 16 GHz, the extracted frequencies did not match the theoretical ones. However, the extraction also produced non-theoretical values. For

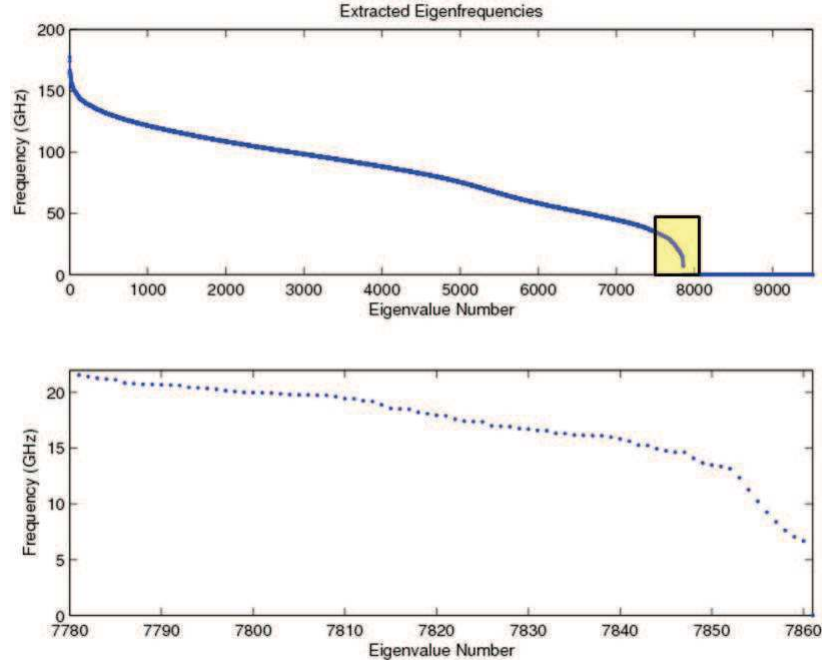


Figure 6.2: PEC Resonator Eigenfrequencies

example, there are 50 theoretical eigenfrequencies below 20 GHz. The extraction algorithm produced 61. There are 145 eigenfrequencies below 30 GHz. The extraction algorithm produced 205.

Equation 6.35 shows there to be an infinite number of eigenfrequencies. The number of extracted eigenfrequencies is finite because the number of eigenfrequencies is related to the size of the impedance matrices. It was found the frequency at which the algorithm begins to extract non-theoretical values is also related to the size of the impedance matrix. The size of the impedance matrices can be controlled by increasing the mesh fidelity in Comsol. However, increases in mesh fidelity will result in significant increases in computation time because the eigendecomposition shown in Equation 6.31 is an $O(N^3)$ operation [32]. As an example, the results shown in Figure 6.2 were obtained with a $9,516 \times 9,516$ element impedance matrix. Eigenfrequency extraction execution time was 75 minutes. A less dense mesh resulting in an impedance matrix with $1,190 \times 1,190$ elements resulted in a solution time of 7.57 seconds. However, the extraction algorithm found nontheoretical eigenfrequencies at

Table 6.1: Eigenfrequencies in GHz for PEC Rectangular Resonator

m	n	p	f_{Theory}	$f_{Extracted}$	% Error
1	0	1	6.687	6.686	0.009
1	0	2	7.062	7.061	0.018
1	0	3	7.647	7.646	0.009
1	0	4	8.397	8.394	0.030
1	0	5	9.273	9.268	0.050
1	0	6	10.243	10.237	0.049
1	0	7	11.281	11.273	0.076
1	0	8	12.372	12.362	0.085
2	0	1	13.180	13.169	0.082
2	0	2	13.374	13.363	0.084
1	0	9	13.502	13.481	0.152
2	0	3	13.692	13.678	0.099
2	0	4	14.125	14.105	0.136
1	0	10	14.662	14.638	0.161
2	0	5	14.662	14.646	0.110
0	1	1	14.812	14.774	0.253
0	1	2	14.985	14.949	0.235
0	1	3	15.269	15.240	0.189
2	0	6	15.294	15.275	0.120
0	1	4	15.659	15.627	0.202
1	0	11	15.846	15.823	0.143
2	0	7	16.008	15.985	0.145

12.79 and 13.00 GHz. Additionally, the error between the extracted and theoretical eigenfrequencies increases as mesh fidelity decreases. For example, the error for the 101 mode for the reduced mesh is 0.33%, still small, but much larger than the result in Table 6.1. Also, the extraction for the less dense mesh produced 72 eigenfrequencies less than 20 GHz. Obviously better results are obtained with a denser mesh at the penalty of increased solve times.

6.5 S-Parameter Measurements

As discussed in Chapter III, the published literature shows no S-parameter results had been obtained using the Comsol Multiphysics software. To validate the software’s capability, a unit cell as described in [90] was created in Comsol. This unit

cell is shown in Figure 6.3. The dimensions of the unit cell were identical to those

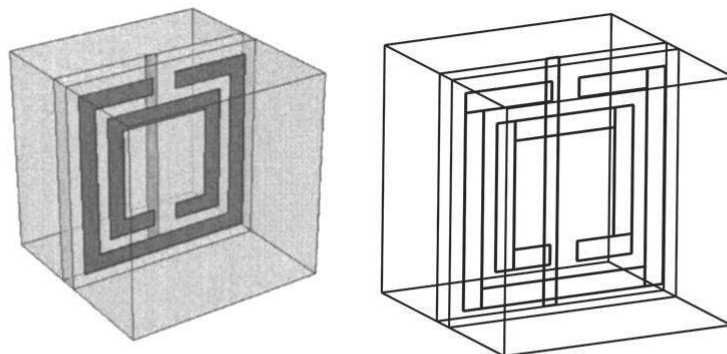


Figure 6.3: Unit Cell for S-Parameter Measurements

used by Smith *et al.*. The cell size was cubic with $d = 2.5$ mm. The substrate was 0.25 mm thick with $\epsilon_r = 4.4 - j0.088$. The outer ring was 2.2 mm with a linewidth of 0.2 mm. The gap between the inner and outer ring was 0.15 mm, and the gap between the ring end's were each 0.3 mm. The rod on the opposite side had a width of 0.14 mm and was 2.5 mm long. All metal thicknesses were $17 \mu\text{m}$ and were given the properties of a PEC. S-parameter measurements were simulated in Comsol. The constitutive parameters were extracted using the method described in Section 3.3.2. All results were compared to the published ones and are shown in Figure 6.4. The Comsol's results were nearly identical to those in [90]. Therefore, it was concluded the software could accurately provide S-parameter measurements.

The goal of this chapter is to perform an eigenfrequency extraction on the unit cell shown in Figure 6.3. However, the size of the impedance matrix would be an issue. The impedance matrix resulting from a Comsol S-parameter simulation of the unit cell shown in Figure 6.3 was $352,692 \times 352,692$. Using even the coarsest settings to create the mesh resulted in a $39,142 \times 39,142$ impedance matrix. Various tests with the eigendecomposition algorithm showed any matrices larger than $20,000 \times 20,000$ elements would overwhelm the machine. Therefore, the thickness of the metal was eliminated by making all metal structures infinitely thin PEC boundaries. There was a concern this would drastically change the resonant characteristics of the structure. However, S-parameter measurements were taken and compared to the

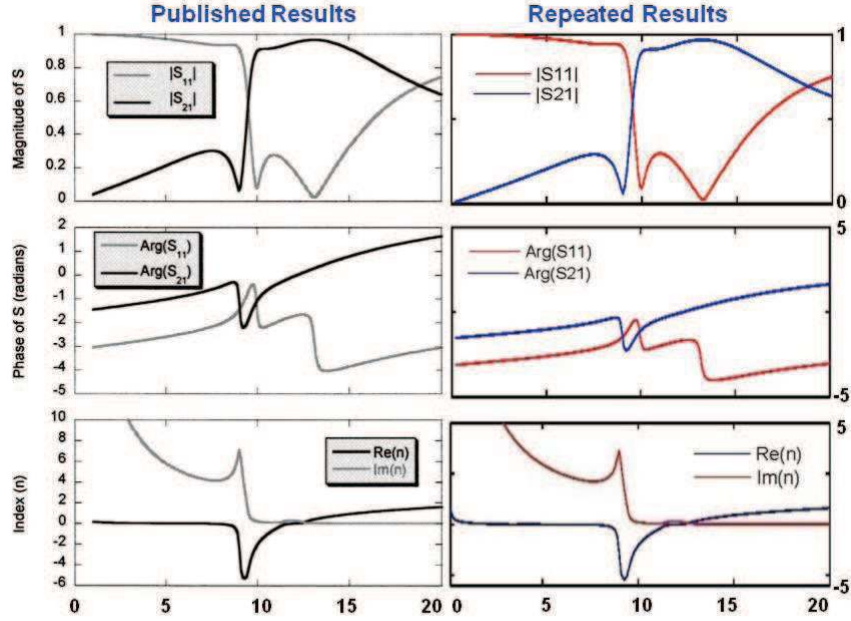


Figure 6.4: S-Parameter Measurements and Extracted Index of Refraction

Table 6.2: Mesh Density and Impedance Matrix Size

Mesh Setting	Mesh Number	Impedance Matrix Size
Normal	One	$116,932 \times 116,932$
Coarse	Two	$34,578 \times 34,578$
Coarser	Three	$20,866 \times 20,866$
Extra Coarse	Four	$7,248 \times 7,248$
Extremely Coarse	Five	$3,260 \times 3,260$

original results. Infinitely thin metallic structures slightly shifted the S-parameter measurements, but by approximately 0.1 GHz. There was still the same resonant type behavior when using an embedded PEC structure compared to PEC structures with small thicknesses. The advantage of removing the metal thickness is significantly fewer mesh elements are required.

Using embedded PEC structures resulted in a smaller impedance matrix. However, the matrices were still too large. The density of the mesh was varied to determine mesh density's impact on the S-parameter measurements. Five different mesh settings were used, each resulting in different impedance matrix sizes. These are shown in Table 6.2 with the resulting S-parameter measurements shown in Figure 6.5.

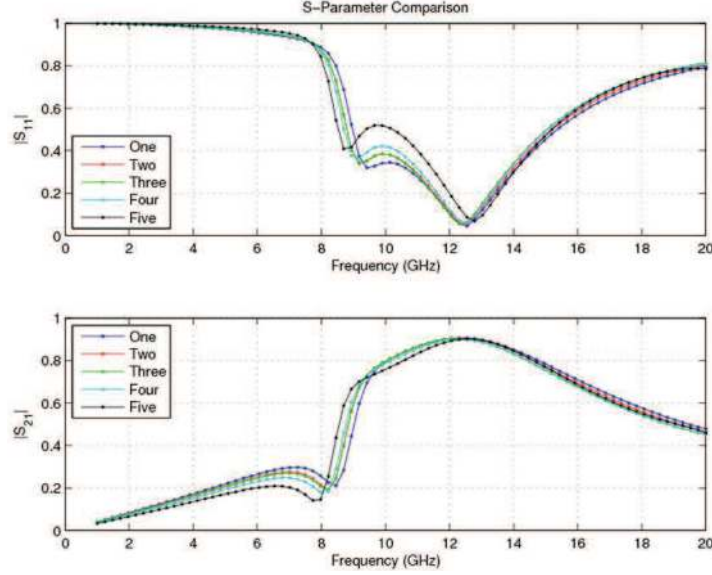


Figure 6.5: S-Parameter Magnitude Comparison for Mesh Densities

Based on these results, it is obvious the impact of using a smaller impedance matrix (less dense mesh) does not significantly impact the resonant characteristics of the unit cell. In the previous section it was shown the size of the impedance matrix directly relates to the accuracy of the extracted eigenfrequencies. However, due to computer limitations, the densest impedance matrix used for the unit cell eigendecomposition in the following section was mesh number four, which had an impedance matrix of $7,248 \times 7,248$.

6.6 Unit Cell Eigendecomposition

An eigendecomposition was performed on unit cells having the ring characteristics shown in Figure 6.3. To help further reduce the impedance matrix size, the metal rod was removed from the structure. This rod impacts the effective permittivity of the unit cell structure. The permeability is a function of the metal rings.

The ring characteristics were slightly modified. The gap between the ring ends was changed to 0.1 mm (Mod 1) and 0.6 mm (Mod 2). This significantly changes the capacitance of the unit cell structure, which will alter the resonant behavior. This can be seen in the S-parameter measurements shown in Figure 6.6. Note the pronounced

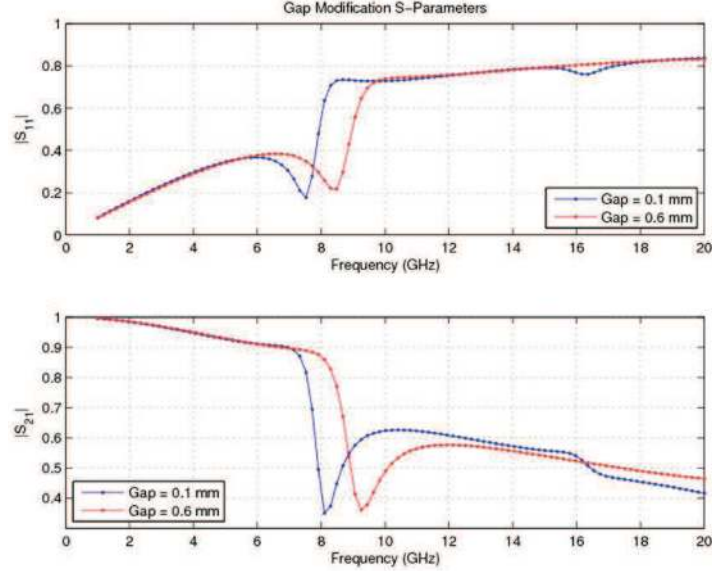


Figure 6.6: S-Parameter Magnitudes for Gap Modifications

shift in the S-parameters by more than 1 GHz. An eigendecomposition was done on the Mod 1 and Mod 2 configurations. The eigenvalues for each geometry were extracted using the eigendecomposition method described in this chapter. Plots of the extracted eigenvalues from each structure and the magnitude of their differences are shown in Figure 6.7. Note each configuration resulted in 128 nonzero eigenvalues less than 100 GHz. Additionally, some values were significantly different, but these large differences manifested in the higher eigenfrequencies. Those eigenvalues in the 6 - 18 GHz range were very close. This is better seen in Figure 6.8. Based on the S-parameter measurements, the structures have significantly different resonant behaviors. However, this is not as obvious when examining the individual eigenfrequencies. It does appear there are specific resonant regions. Note the lack of eigenvalues between 5.9 and 6.3 GHz, 8.5 and 9.4 GHz, and 13.4 and 14.1 GHz. However, no definitive conclusions could be drawn from this data. Further eigenfrequency extractions were performed with the gap in the rings modified to different widths (0.2, 0.3, 0.4, and 0.5 mm). Extracted eigenfrequencies were compared, but no definitive changes in specific eigenfrequencies were noted.

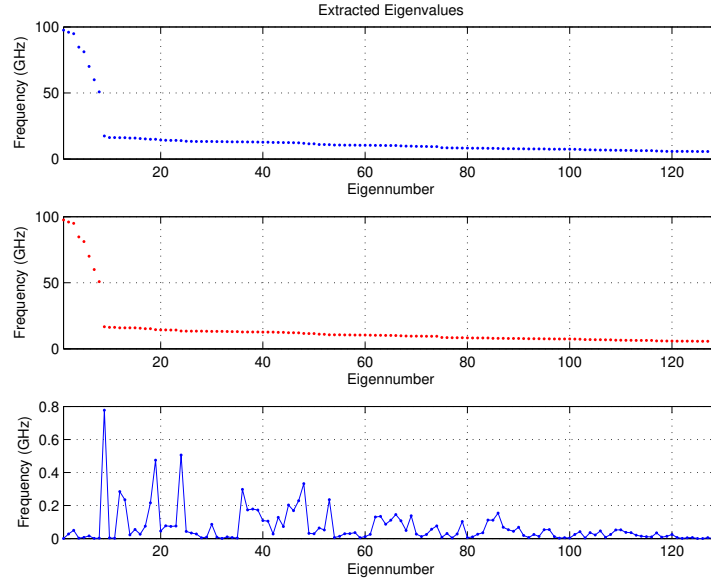


Figure 6.7: Eigenvalues for Gap Modifications

It was determined the reduced impedance matrix sizes were not allowing enough fidelity to see the eigenvalue changes. To test this, two different meshes were used to create different, although similarly sized, impedance matrices for the Mod 2 structure. The different meshes were created by toggling the jiggle function within Comsol. The extracted eigenfrequencies obtained for the same structure but using different meshes were compared. Results are shown in Figure 6.9. The extracted eigenfrequencies are not identical. In fact, note the similarities between Figures 6.7 and 6.9. The graphs of the differences between the extracted eigenfrequencies in both figures seem to indicate the variations in the eigenfrequencies are a function of the mesh rather than a function of changes in the structure of the unit cell. Unfortunately, increasing the mesh size to the maximum capability did not alleviate this problem. It is believed, however, that further increases in mesh fidelity will lead to specific eigenfrequency identification of different unit cell structures. However, this could not be tested due to memory limitations on the computational hardware.

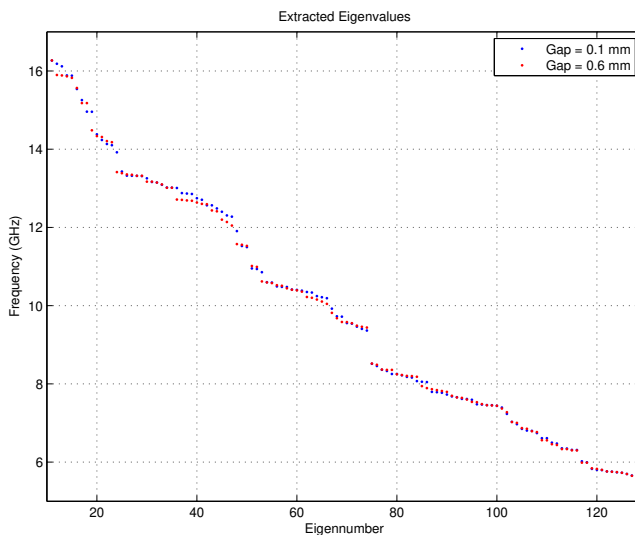


Figure 6.8: Eigenvalues from 6-18 GHz

6.7 Summary

This chapter presented an eigenfrequency decomposition method which has been shown to be able to extract a structure’s individual eigenfrequencies. The method was implemented using the Comsol Multiphysics software and tested using a structure with theoretically known eigenfrequencies. Extracted eigenfrequencies of a rectangular PEC resonator matched the theoretical values. However, it was shown mesh density plays an important roll in the fidelity of the solution.

The eigenfrequency decomposition method was applied to a metamaterial unit cell. In order to reduce impedance matrix size, infinitely thin metallic boundaries were used in place of actual metal structures. S-parameter measurements showed this change had little impact on the device’s resonant behavior. Eigenfrequencies were extracted from the unit cells. However, the mesh was not dense enough to allow identification of shifts in eigenfrequencies as a result of changes to the device structures. The extracted eigenfrequencies were impacted by changes in the mesh. A finer, denser mesh is needed to adequately simulate these unit cells. However, computational limits were reached due to memory limitations.

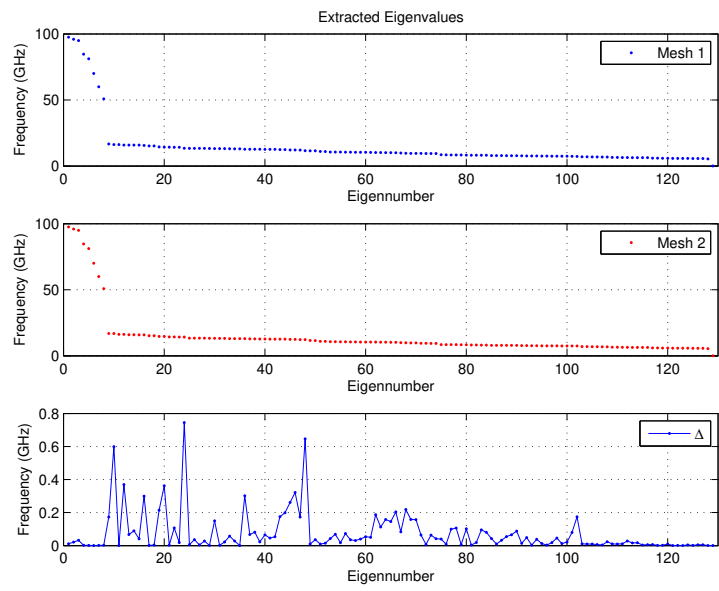


Figure 6.9: Extracted Eigenfrequencies Using Different Meshes

VII. Conclusions

7.1 Research Summary

The performance of simplified cylindrical cloaks with various constitutive parameters was analyzed in order to understand the impact constitutive values have on field behavior. Prior to this research, the material parameters of simplified cloaks have focused on satisfying specific values of $\varepsilon_z\mu_\theta$ and $\varepsilon_z\mu_r$ while matching the impedance at the cloak's outer boundary. A third constraint equation was introduced which helps control the overall effectiveness of the cylindrical cloak.

Cylindrical cloaks were analyzed with constitutive parameters that satisfied the specific values for $\varepsilon_z\mu_\theta$ and $\varepsilon_z\mu_r$. It was shown deviations from this derived third constraint equation resulted in larger fields being transmitted into a cylindrical cloak's hidden region. As the cloak's constitutive parameters were changed such that this new constraint was better satisfied, the amount of energy transmitted into the hidden region was shown to be reduced. The resulting impedance mismatch at $r = b$ due to changing the constitutive parameters resulted in a significant scattered field. However, despite reducing energy transmitted into the hidden region, which resulted in a reduction in the scattered field by the cloaked object, the cloak itself was creating a large scattered field. Hence, in terms of overall scattering width, having a matched impedance at $r = b$ was shown to be more important than reducing the transmitted energy into the hidden region.

A new way to develop simplified material parameter sets for cylindrical cloaks was developed. Specifically, for TM^z incident waves, the approximation of μ_θ should first be defined using a Taylor series expansion of the ideal parameter as defined by the derived third constraint equation. The constitutive parameters μ_r and ε_z can then be determined by making the products $\mu_\theta\varepsilon_z$ and $\mu_r\varepsilon_z$ equal to the same products using the ideal material parameter set. The performance of cloaks developed in this manner is limited only by the number of terms used in the Taylor series expansion, which is dictated by existing manufacturing capabilities. Additionally, the applicability of this method extends to TE^z fields by duality.

Scattering width improvement was observed for all angles when compared to previous published material parameter sets. Significant improvement was noted in the forward scattering region. It was also shown the simplified parameter set put forth in [102] is a simplification of this method in which the Taylor series expansion of μ_θ is limited to the first term. These parameter sets were found to have relatively consistent performance for all values of the cloak’s radial boundary, b . Performance for a constant number of terms in the Taylor series does slightly degrade as b increases, but for all b , ideal cloaking performance is approached as $N \rightarrow \infty$.

A Green’s function approach for determining scattering widths from a cylindrical cloak was shown to have significant computational savings compared to standard FEM methods. This savings can be useful for error analysis or optimization studies on a particular cloak geometry. Also, the computational domain size is directly related to the cylindrical cloak’s radius. A larger cloak results in a larger domain size. The increase in computational domain requires either a longer solution time due to the increased number of elements or a reduction in mesh density which impacts solution accuracy. The Green’s function implementation is much faster than an FEM solution and is more adept at handling larger problem geometries.

Metamaterial unit cells were analyzed using an eigendecomposition technique. S-parameter measurements showed definite shifts in unit cell resonant frequencies due to structural changes. Eigenfrequencies were extracted from the unit cells. Shifts in resonant frequency locations were noted for different cell geometries, but no definitive relationships could be drawn. Mesh densities were limited to very coarse settings due to computational limitations. Extracted eigenfrequencies were shown to be mesh-dependent. The problem could be ameliorated by increasing mesh fidelity, but memory limitations were reached preventing this from being further explored.

7.2 Recommendations for Future Research

The work done in Chapter IV considered infinite cylindrical cloaks. Such analysis was done due to computational efficiencies gained when solving two-dimensional

problems. To physically realize such a structure, a three-dimensional analysis will be required i.e. the cloak must be terminated in the \hat{z} direction at $z = z_1$ and $z = z_2$. This is shown in Figure 7.1. The termination of the infinite cylinder will result in

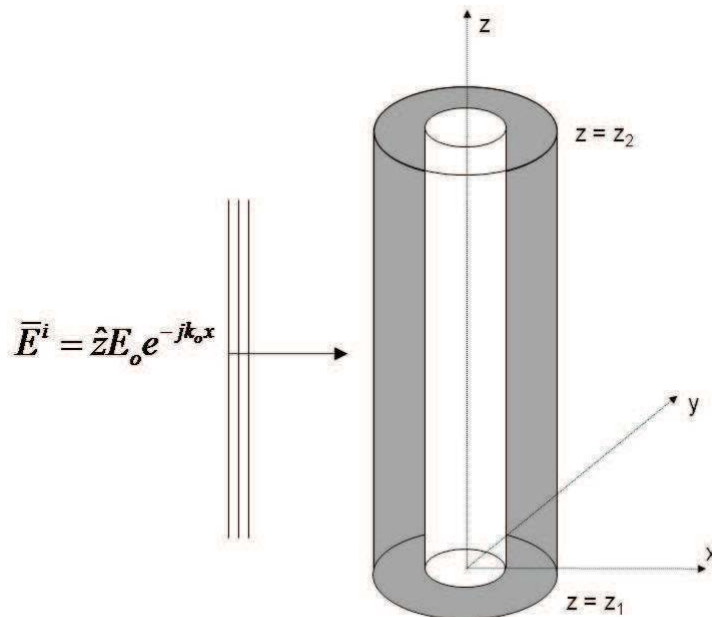


Figure 7.1: Three-Dimensional Cylindrical Cloak

scattering from the cloak even if the ideal parameters are assumed. This is due to trailing edge diffraction resulting from the edges at z_1 and z_2 in Figure 7.1. It is not clear how large the diffracted field will be. The typical 2-D-to-3-D conversion formula [49],

$$\sigma_{3D} = \sigma_{2D} \frac{2l^2}{\lambda}, \quad (7.1)$$

cannot be used since σ_{2D} for ideal cloaks is zero. However, for reduced parameter cloaks, it will be interesting to analyze the accuracy of Equation 7.1. The \hat{z} directed incident field will excite surface currents in the same direction. There are sharp discontinuities at $z = z_1$ and $z = z_2$, which will result in a significant scattered field. The size of the scattered field will depend on the properties of the terminating ends of the cloak. Ways to reduce to the scattering could include tapering using a resistive material to better match the termination to free space.

Additionally, a three-dimensional cloak’s functionality with the ideal cloak parameters should be independent of θ . As the incident angle is swept around the body of the cloak. The diffraction effects should be identical for all incident θ angles. However, when θ is changed i.e. the incident wave approaches from a direction not normal to the cylinder’s broad-side, there will be a significant change in RCS because the terminated ends’ scattering mechanism is changing from that of a grazing incidence to a specular return.

This work focused specifically on two-dimensional cylindrical cloaks. A computational improvement was noted by using a Green’s function to compute the scattering width of a cloaked PEC cylinder. A PEC has a complex permittivity such that

$$\varepsilon_c(r, \phi, \omega) = \lim_{\sigma \rightarrow \infty} \varepsilon + j \frac{\sigma}{\omega}, \quad (7.2)$$

where σ is the conductivity of the material. Alternate Green’s functions can be derived such that σ is finite at $r = a$, which results in field penetration into the hidden region. The material inside the hidden region may be inhomogeneous and not symmetric with respect to θ . This would result in a significantly more complex Green’s function, but allows for any geometry to be placed inside the inner boundary.

As discussed in Chapter II, there have been a number of different cloak geometries discussed in the published literature. It would be an interesting academic exercise to derive the Green’s function for these geometries and implement a computational solution as was done in Chapter V. Green’s functions can help gain physical insight into the cloaking function, which may prove useful for these alternate geometries. Additionally, it is expected the Green’s function will provide a significant computational improvement which may be beneficial if optimizations are being performed.

Finally, further work can be done extracting the eigenfrequencies from unit cell designs. Specifically, increasing the memory should allow for denser meshes. This increase in mesh density should allow for structural differences to manifest in eigenfrequency shifts. This could create a new unit cell design paradigm where eigenfre-

quency location is correlated to a structural feature. Designs could be optimized for larger bandwidths by using Fischer's optimization technique described in [31]. Additionally, alternate techniques to address the bandwidth problem of unit cells should be investigated. Specifically, multiresonant structures within the same unit cell might provide an increase in bandwidth. Additionally, active materials could be used in unit cell designs to increase or actively change the bandwidth characteristics of the unit cells.

7.3 Acknowledgement

This work was sponsored by the National Radar Cross Section Test Facility (NRTF). It supports their efforts investigating novel ways to control electromagnetic fields during RCS measurements. AFIT appreciates NRTF's support and continued interest in investigating the exciting field of electromagnetic cloaks and metamaterials.

Appendix A. Material Parameter Derivation

The development below mirrors what is shown in [97] with clarifying text added where the original text was deemed ambiguous or unclear. Maxwell's equations govern the behavior of electromagnetic waves; they are valid in any coordinate system. Ward and Pendry have shown the behavior of electromagnetic waves in a general coordinate system can be modeled in Cartesian coordinates using a designed material with specific permittivity and permeability tensors [72,97]. It is this fact upon which cloaking is based. To prove this, take the general form of Faraday's Law in free space.

$$\nabla \times \vec{E} = -\mu_o \frac{\partial \vec{H}}{\partial t} \quad (\text{A.1})$$

The desire is to find the form of Faraday's law in a general coordinate system given by the variables (q_1, q_2, q_3) with unit vectors, \hat{u}_1 , \hat{u}_2 , and \hat{u}_3 in the direction of the q_1 , q_2 , and q_3 axes. Additionally, it is assumed there exists a transformation from Cartesian coordinates to this general coordinate system where the point q_i is a function of (x, y, z) expressed as

$$\begin{aligned} q_1 &= F_1(x, y, z), \\ q_2 &= F_2(x, y, z), \\ q_3 &= F_3(x, y, z). \end{aligned} \quad (\text{A.2})$$

It is assumed the transformation is invertible such that the point (q_1, q_2, q_3) can be transformed back to Cartesian coordinates by

$$\begin{aligned} x &= f_1(q_1, q_2, q_3), \\ y &= f_2(q_1, q_2, q_3), \\ z &= f_3(q_1, q_2, q_3). \end{aligned} \quad (\text{A.3})$$

Next, it is important to understand how to calculate the differential length, ds , of a line segment in the general coordinate system. This requires the use of the Euclidean

metric, which is defined in terms of the Jacobian, J , and is equal to $J^T J$ where

$$J = \begin{pmatrix} \frac{\partial x}{\partial q_1} & \frac{\partial x}{\partial q_2} & \frac{\partial x}{\partial q_3} \\ \frac{\partial y}{\partial q_1} & \frac{\partial y}{\partial q_2} & \frac{\partial y}{\partial q_3} \\ \frac{\partial z}{\partial q_1} & \frac{\partial z}{\partial q_2} & \frac{\partial z}{\partial q_3} \end{pmatrix}, \quad \text{and} \quad J^T = \begin{pmatrix} \frac{\partial x}{\partial q_1} & \frac{\partial y}{\partial q_1} & \frac{\partial z}{\partial q_1} \\ \frac{\partial x}{\partial q_2} & \frac{\partial y}{\partial q_2} & \frac{\partial z}{\partial q_2} \\ \frac{\partial x}{\partial q_3} & \frac{\partial y}{\partial q_3} & \frac{\partial z}{\partial q_3} \end{pmatrix}. \quad (\text{A.4})$$

The squared length of a differential line segment is expressed as

$$ds^2 = \sum_{i=1}^3 \sum_{j=1}^3 (J^T J)_{ij} dq^i dq^j. \quad (\text{A.5})$$

Obviously, in Cartesian coordinates, $q_1 = x$, $q_2 = y$, and $q_3 = z$ and the resulting Jacobian, transpose Jacobian, and product of the two matrices are

$$J = \begin{pmatrix} 1 & 0 & 0 \\ 0 & 1 & 0 \\ 0 & 0 & 1 \end{pmatrix}, \quad \text{and} \quad J^T = \begin{pmatrix} 1 & 0 & 0 \\ 0 & 1 & 0 \\ 0 & 0 & 1 \end{pmatrix} \quad (\text{A.6})$$

$$J^T J = \begin{pmatrix} 1 & 0 & 0 \\ 0 & 1 & 0 \\ 0 & 0 & 1 \end{pmatrix}. \quad (\text{A.7})$$

Hence, the squared differential length is the familiar form

$$ds^2 = dx^2 + dy^2 + dz^2. \quad (\text{A.8})$$

In their paper, Ward and Pendry use the following notation

$$ds^2 = Q_{11}dq_1^2 + Q_{22}dq_2^2 + Q_{33}dq_3^2 + 2Q_{12}dq_1dq_2 + 2Q_{13}dq_1dq_3 + 2Q_{23}dq_2dq_3, \quad (\text{A.9})$$

where

$$Q_{ij} = \frac{\partial x}{\partial q_i} \frac{\partial x}{\partial q_j} + \frac{\partial y}{\partial q_i} \frac{\partial y}{\partial q_j} + \frac{\partial z}{\partial q_i} \frac{\partial z}{\partial q_j}. \quad (\text{A.10})$$

Using the definition of Q_{ij} , it is obvious Equation A.9 matches that of Equation A.5.

It is necessary to represent the differential length of a line segment in the direction of one of the unit vectors. As an example, suppose there exists a differential length only in the \hat{u}_1 direction. The result is $dq_2 = dq_3 = 0$. This results in the length, ds to be

$$ds = \sqrt{(J^T J)_{11}} dq_1. \quad (\text{A.11})$$

Using the notation of Ward and Pendry, this is identical to

$$ds = \sqrt{Q_{11}} dq_1. \quad (\text{A.12})$$

As a simplification, Ward and Pendry let $Q_1^2 = Q_{11}$ and $Q_1 = \sqrt{Q_{11}}$. Therefore

$$ds = Q_1 dq_1, \quad (\text{A.13})$$

or, in more general terms, the differential length along the direction of the i^{th} unit vector is

$$ds_i = Q_i dq_i. \quad (\text{A.14})$$

This notation is necessary because the desire is to determine the form of Faraday's Law in the general coordinate system. To do this, consider a small differential element of the shape of a parallelepiped as shown in Figure A.1. It is possible to calculate

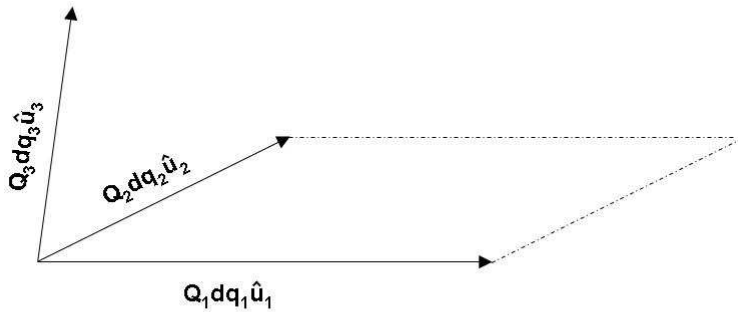


Figure A.1: Differential parallelepiped element

the projection of $\nabla \times \vec{E}$ onto the normal to the \hat{u}_1 - \hat{u}_2 plane. To do this, first take the

line integral.

$$\oint_C \vec{E} \cdot d\vec{l} \quad (\text{A.15})$$

The integral can be evaluated by letting $E_i = \vec{E} \cdot \hat{u}_i$. The components along the closed path are shown in Figure A.2. By taking into account the direction of the contour,

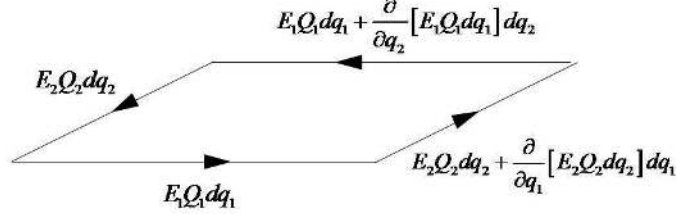


Figure A.2: Line integral differential components

the line integral is evaluated to be

$$\oint_C \vec{E} \cdot d\vec{l} = dq_1 \frac{\partial}{\partial q_1} [E_2 Q_2 dq_2] - dq_2 \frac{\partial}{\partial q_2} [E_1 Q_1 dq_1]. \quad (\text{A.16})$$

Stokes Theorem can now be applied. Recall, Stokes Theorem states

$$\oint_C \vec{E} \cdot d\vec{l} = \iint_S \nabla \times \vec{E} \cdot \hat{n} dS = \iint_S \nabla \times \vec{E} \cdot (\hat{u}_1 \times \hat{u}_2) Q_1 dq_1 Q_2 dq_2. \quad (\text{A.17})$$

For this geometry note that

$$\begin{aligned} \hat{n} &= \hat{u}_1 \times \hat{u}_2, \\ dS &= Q_1 dq_1 Q_2 dq_2. \end{aligned} \quad (\text{A.18})$$

Thus, applying Stokes Theorem to the line integral along this differential contour yields

$$\nabla \times \vec{E} \cdot (\hat{u}_1 \times \hat{u}_2) Q_1 dq_1 Q_2 dq_2 = dq_1 \frac{\partial}{\partial q_1} [E_2 Q_2 dq_2] - dq_2 \frac{\partial}{\partial q_2} [E_1 Q_1 dq_1]. \quad (\text{A.19})$$

This can be simplified to

$$\nabla \times \vec{E} \cdot (\hat{u}_1 \times \hat{u}_2) Q_1 Q_2 = \frac{\partial}{\partial q_1} [E_2 Q_2] - \frac{\partial}{\partial q_2} [E_1 Q_1]. \quad (\text{A.20})$$

Letting $\hat{E}_i = Q_i E_i$ results in the following.

$$\nabla \times \vec{E} \cdot (\hat{u}_1 \times \hat{u}_2) Q_1 Q_2 = \frac{\partial \hat{E}_2}{\partial q_1} - \frac{\partial \hat{E}_1}{\partial q_2}. \quad (\text{A.21})$$

Note the right hand side is component 3 of the curl of the electric field in the general coordinate system.

$$\left(\nabla_q \times \hat{E} \right)^3 = \frac{\partial \hat{E}_2}{\partial q_1} - \frac{\partial \hat{E}_1}{\partial q_2} = \nabla \times \vec{E} \cdot (\hat{u}_1 \times \hat{u}_2) Q_1 Q_2 \quad (\text{A.22})$$

Similarly, component 1 and component 2 of the curl of the electric field in the general coordinate system can be written as

$$\left(\nabla_q \times \hat{E} \right)^1 = \frac{\partial \hat{E}_3}{\partial q_2} - \frac{\partial \hat{E}_2}{\partial q_3} = \nabla \times \vec{E} \cdot (\hat{u}_2 \times \hat{u}_3) Q_2 Q_3 \quad (\text{A.23})$$

$$\left(\nabla_q \times \hat{E} \right)^2 = \frac{\partial \hat{E}_1}{\partial q_3} - \frac{\partial \hat{E}_3}{\partial q_1} = \nabla \times \vec{E} \cdot (\hat{u}_3 \times \hat{u}_1) Q_1 Q_3 \quad (\text{A.24})$$

Note how the curl operation in the general coordinate system is of the same form as in Cartesian coordinates, with the only difference being scale factors on the component parts of the vector field.

The form for the curl in the general coordinated system can be substituted into the left-hand side of Faraday's Law (Equation A.22) and determine Faraday's Law's form in the general coordinate system.

$$\left(\nabla_q \times \hat{E} \right)^3 = \nabla \times \vec{E} \cdot (\hat{u}_1 \times \hat{u}_2) Q_1 Q_2 = -\mu_o \frac{\partial \vec{H}}{\partial t} \cdot (\hat{u}_1 \times \hat{u}_2) Q_1 Q_2 \quad (\text{A.25})$$

The magnetic field can be expressed in terms of its contravariant components as

$$\vec{H} = H^1 \hat{u}_1 + H^2 \hat{u}_2 + H^3 \hat{u}_3 \quad (\text{A.26})$$

The relationship between the contravariant and covariant components of a vector is

$$\begin{bmatrix} H_1 \\ H_2 \\ H_3 \end{bmatrix} = \begin{pmatrix} \hat{u}_1 \cdot \hat{u}_1 & \hat{u}_1 \cdot \hat{u}_2 & \hat{u}_1 \cdot \hat{u}_3 \\ \hat{u}_2 \cdot \hat{u}_1 & \hat{u}_2 \cdot \hat{u}_2 & \hat{u}_2 \cdot \hat{u}_3 \\ \hat{u}_3 \cdot \hat{u}_1 & \hat{u}_3 \cdot \hat{u}_2 & \hat{u}_3 \cdot \hat{u}_3 \end{pmatrix} \begin{bmatrix} H^1 \\ H^2 \\ H^3 \end{bmatrix} = \bar{g} \begin{bmatrix} H^1 \\ H^2 \\ H^3 \end{bmatrix}, \quad (\text{A.27})$$

where \bar{g} is the metric tensor of the general coordinate system (not the Euclidean metric). A more compact way of expressing this is

$$H_i = \sum_{j=1}^3 g_{ij} H^j. \quad (\text{A.28})$$

Solving for the H^i components results in

$$H^i = \sum_{j=1}^3 g^{ij} H_j, \quad (\text{A.29})$$

where g^{ij} are the components of g^{-1} . The above can be used in the expressions to solve for components 1, 2, and 3 for the curl of the electric field in the general coordinate system.

$$\left(\nabla_q \times \hat{E} \right)^1 = -\mu_o \sum_{j=1}^3 g^{1j} \frac{\partial H_j}{\partial t} \hat{u}_1 \cdot (\hat{u}_2 \times \hat{u}_3) Q_2 Q_3 \quad (\text{A.30})$$

$$\left(\nabla_q \times \hat{E} \right)^2 = -\mu_o \sum_{j=1}^3 g^{2j} \frac{\partial H_j}{\partial t} \hat{u}_2 \cdot (\hat{u}_3 \times \hat{u}_1) Q_3 Q_1 \quad (\text{A.31})$$

$$\left(\nabla_q \times \hat{E} \right)^3 = -\mu_o \sum_{j=1}^3 g^{3j} \frac{\partial H_j}{\partial t} \hat{u}_3 \cdot (\hat{u}_1 \times \hat{u}_2) Q_1 Q_2 \quad (\text{A.32})$$

By defining

$$\hat{\mu}^{ij} = g^{ij} |\hat{u}_1 \cdot (\hat{u}_2 \times \hat{u}_3)| Q_1 Q_2 Q_3 (Q_i Q_j)^{-1}, \quad (\text{A.33})$$

and

$$\hat{H}_j = Q_j H_j, \quad (\text{A.34})$$

the following is the expression for the components of the curl of the electric field.

$$\left(\nabla_q \times \hat{E} \right)^i = -\mu_o \sum_{j=1}^3 \hat{\mu}^{ij} \frac{\partial \hat{H}_j}{\partial t} \quad (\text{A.35})$$

A similar process can be done for Ampere's Law to show that

$$\left(\nabla_q \times \hat{H} \right)^i = \varepsilon_o \sum_{j=1}^3 \hat{\varepsilon}^{ij} \frac{\partial \hat{E}_j}{\partial t}. \quad (\text{A.36})$$

Thus, given a coordinate transformation from Cartesian coordinates, the behavior of the electromagnetic fields in the coordinate transform space can be realized in Cartesian coordinates using a complex material with permittivity and permeability tensors described as [97]

$$\hat{\varepsilon}^{ij} = g^{ij} |\hat{u}_1 \cdot (\hat{u}_2 \times \hat{u}_3)| Q_1 Q_2 Q_3 (Q_i Q_j)^{-1}, \quad (\text{A.37})$$

$$\hat{\mu}^{ij} = g^{ij} |\hat{u}_1 \cdot (\hat{u}_2 \times \hat{u}_3)| Q_1 Q_2 Q_3 (Q_i Q_j)^{-1}. \quad (\text{A.38})$$

Appendix B. Green's Function Derivation

A Green's function for a magnetic line source radiating in the presence of a layered PEC cylinder is derived. The geometry for this problem is shown in Figure B.1. The final solution will be reached by first solving for the Green's function for a PEC

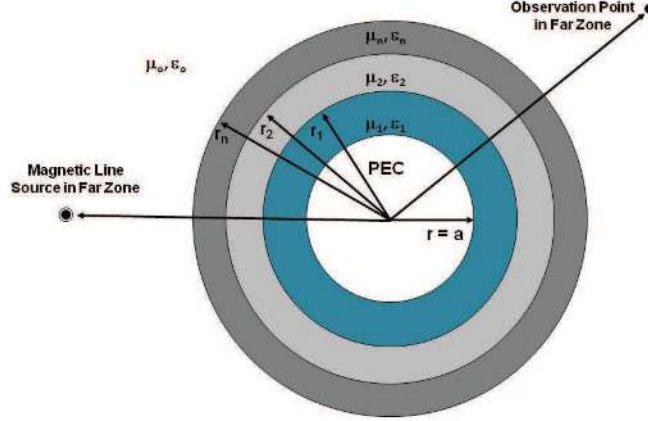


Figure B.1: Problem geometry for Green's function derivation

cylinder illuminated by a magnetic line source. This is done to ensure the process is correct and to provide a series of checks for solution accuracy. Multiple layers of dielectric materials surrounding the PEC will then be added to arrive at the final solution.

For this problem, the source is an infinite magnetic line current in the \hat{z} direction. Because of this, the incident and scattered magnetic fields will only be in the \hat{z} direction. Since the \vec{H} field will only have a \hat{z} component, the vector potential \vec{F} will also only have a \hat{z} component; the vector potential, $\vec{A} = 0$. The potential field must obey

$$\nabla^2 \vec{F} + k^2 \vec{F} = -\epsilon \vec{M}, \quad (\text{B.1})$$

which is a vector wave equation. Since both \vec{F} and \vec{M} are \hat{z} directed, the following scalar equation results

$$\nabla^2 F_z + k^2 F_z = -\epsilon M_z. \quad (\text{B.2})$$

Also, z-invariance has been assumed. Thus,

$$\nabla_t^2 F_z + k^2 F_z = -\varepsilon M_z, \quad (\text{B.3})$$

where ∇_t^2 is the transverse Laplacian, which in cylindrical coordinates is

$$\nabla_t^2 = \frac{1}{r} \frac{\partial}{\partial r} \left(r \frac{\partial}{\partial r} \right) + \frac{1}{r^2} \frac{\partial^2}{\partial \theta^2}. \quad (\text{B.4})$$

The boundary conditions are

$$\left. \frac{\partial F_z}{\partial r} \right|_{r=a} = 0, \quad (\text{B.5})$$

which is a result of the PEC boundary at $r = a$. Also the radiation condition must be satisfied.

$$\left. \frac{\partial F_z}{\partial r} \right|_{r \rightarrow \infty} = -jk F_z|_{r \rightarrow \infty} \quad (\text{B.6})$$

Finally, it is expected that

$$F(r, \theta) = F(r, \theta + 2\pi). \quad (\text{B.7})$$

Now, the Green's function must solve

$$\nabla_t^2 G(\bar{r}, \bar{r}') + k^2 G(\bar{r}, \bar{r}') = -\delta(\bar{r} - \bar{r}'). \quad (\text{B.8})$$

Note that

$$\delta(\bar{r} - \bar{r}') = \frac{\delta(r - r')\delta(\theta - \theta')}{r}, \quad (\text{B.9})$$

and that

$$G(\bar{r}, \bar{r}') = G(r, \theta; r', \theta') \quad (\text{B.10})$$

The differential equation the Green's function must satisfy can be rewritten as

$$\nabla_t^2 G(\bar{r}, \bar{r}') + k^2 G(\bar{r}, \bar{r}') = -\frac{\delta(r - r')\delta(\theta - \theta')}{r}. \quad (\text{B.11})$$

From [25], the solution can be found by

$$G(r, \theta; r', \theta') = \sum_{m=0}^{\infty} \tilde{u}_m(\theta) \tilde{u}_m^*(\theta') G_r(r, r'; \lambda_m), \quad (\text{B.12})$$

where \tilde{u}_m are the orthonormal eigenfunctions which satisfy

$$\left[\frac{d^2}{d\theta^2} + \lambda_m \right] \tilde{u}_m(\theta) = 0. \quad (\text{B.13})$$

Also, note that

$$k^2 - \lambda_r - \frac{\lambda_\theta}{r^2} = 0, \quad (\text{B.14})$$

and that G_r satisfies

$$\frac{1}{r} \frac{d}{dr} \left(r \frac{dG_r}{dr} \right) + \left(k^2 - \frac{\lambda_m}{r^2} \right) G_r = -\frac{\delta(r - r')}{r}. \quad (\text{B.15})$$

The following boundary conditions on the Green's function are enforced.

$$\left. \frac{\partial G(r, \theta; r', \theta')}{\partial r} \right|_{r=a} = 0 \quad (\text{B.16})$$

$$G(r, \theta; r', \theta') = G(r, \theta + 2\pi; r', \theta') \quad (\text{B.17})$$

$$\left. \frac{\partial G(r, \theta; r', \theta')}{\partial r} \right|_{r \rightarrow \infty} = -jkG(r, \theta; r', \theta')|_{r \rightarrow \infty} \quad (\text{B.18})$$

By having $G(r, \theta; r', \theta')$ satisfy the same boundary conditions as F_z , the complementary solution will vanish.

To begin, first solve for $\tilde{u}_m(\theta)$ and apply the appropriate boundary condition.

Recall

$$\left[\frac{d^2}{d\theta^2} + \lambda_m \right] \tilde{u}_m(\theta) = 0. \quad (\text{B.19})$$

A general solution for $\tilde{u}_m(\theta)$ is

$$\tilde{u}_m(\theta) = A \cos \sqrt{\lambda_m} \theta + B \sin \sqrt{\lambda_m} \theta. \quad (\text{B.20})$$

Applying $\tilde{u}_m(\theta) = \tilde{u}_m(\theta + 2\pi)$ yields

$$A \cos \sqrt{\lambda_m} \theta + B \sin \sqrt{\lambda_m} \theta = A \cos \sqrt{\lambda_m} (\theta + 2\pi) + B \sin \sqrt{\lambda_m} (\theta + 2\pi). \quad (\text{B.21})$$

The only way this equation can be satisfied is if $\sqrt{\lambda_m} = m$ where $m = 0, 1, 2, \dots$

Therefore

$$\begin{aligned} \sqrt{\lambda_m} &= m, & m &= 0, 1, 2, 3, \dots, \\ \lambda_m &= m^2, & m &= 0, 1, 2, 3, \dots \end{aligned} \quad (\text{B.22})$$

The general solution can be written as

$$\tilde{u}_m(\theta) = A \cos m\theta + B \sin m\theta, \quad m = 0, 1, 2, \dots \quad (\text{B.23})$$

$A \cos m\theta$ is orthogonal to $B \sin m\theta$. Therefore, it is known that $A \cos m\theta$, $m = 0, 1, 2, \dots$ are all part of the solution of eigenvectors. Additionally, $B \sin m\theta$, $m = 1, 2, \dots$ are also part of the solution for the eigenvectors. Also $\tilde{u}_m(\theta)$ has been defined as an orthonormal set of eigenfunctions. Therefore, it is possible to calculate the coefficients, A and B because

$$\int_0^{2\pi} A^2 \cos^2 m\theta d\theta = 1, \quad (\text{B.24})$$

$$\int_0^{2\pi} B^2 \sin^2 m\theta d\theta = 1. \quad (\text{B.25})$$

Using the trigonometric identities

$$\begin{aligned} \cos^2 m\theta &= \frac{1}{2} + \frac{1}{2} \cos 2m\theta, \\ \sin^2 m\theta &= \frac{1}{2} - \frac{1}{2} \cos 2m\theta, \end{aligned} \quad (\text{B.26})$$

results in the coefficients being found.

$$\int_0^{2\pi} A^2 \cos^2 m\theta d\theta = \frac{A^2}{2} \left[\int_0^{2\pi} d\theta + \int_0^{2\pi} \cos 2m\theta d\theta \right] = 1 \quad (\text{B.27})$$

This simplifies to

$$A = \sqrt{\frac{1}{\pi}}. \quad (\text{B.28})$$

However, this is only valid if $m \neq 0$. Note when $m = 0$, the integral becomes

$$A^2 \int_0^{2\pi} d\theta = 1, \quad (\text{B.29})$$

which yields

$$A = \sqrt{\frac{1}{2\pi}}. \quad (\text{B.30})$$

Following a similar process, it is found that

$$B = \sqrt{\frac{1}{\pi}}. \quad (\text{B.31})$$

There is no issue when $m = 0$ for B since $\sin(0) = 0$ which results in a trivial solution.

To make things easy to write, express A and B as

$$A, B = \sqrt{\frac{\epsilon_m}{2\pi}} \quad (\text{B.32})$$

where

$$\epsilon_m = \begin{cases} 1 & m = 0 \\ 2 & m = 1, 2, 3... \end{cases} \quad (\text{B.33})$$

Note this shows that when $m = 0$, $B = \sqrt{\frac{1}{2\pi}}$. This isn't necessarily true, but makes no difference since the term is multiplied by 0 and the result is the same. Now, substituting the eigenvectors results in

$$\sum_{m=0}^{\infty} \tilde{u}_m(\theta) \tilde{u}_m(\theta') = \frac{1}{2\pi} \sum_{m=0}^{\infty} \epsilon_m [\cos m\theta \cos m\theta' + \sin m\theta \sin m\theta']. \quad (\text{B.34})$$

Using the trigonometric identity

$$\cos x \cos y + \sin x \sin y = \cos(x - y), \quad (\text{B.35})$$

the result is

$$\sum_{m=0}^{\infty} \tilde{u}_m(\theta) \tilde{u}_m(\theta') = \frac{1}{2\pi} \sum_{m=0}^{\infty} \epsilon_m \cos m(\theta - \theta'), \quad (\text{B.36})$$

which is the first part of the solution for the Green's function.

Next, the solution for $G(r, r'; \lambda_m)$ is found. It has been shown $\lambda_m = m^2$; thus the notation can be rewritten as $G(r, r'; m^2)$. $G(r, r'; m^2) = G_r$ will satisfy

$$\frac{1}{r} \frac{d}{dr} \left(r \frac{dG_r}{dr} \right) + \left(k^2 - \frac{\lambda_m}{r^2} \right) G_r = -\frac{\delta(r - r')}{r} \quad (\text{B.37})$$

Multiplying each side of the equation by r results in

$$\frac{d}{dr} \left(r \frac{dG_r}{dr} \right) + \left(k^2 r - \frac{m^2}{r} \right) G_r = -\delta(r - r'). \quad (\text{B.38})$$

This equation can be solved using the $U - T$ method, where $U(r)$ and $T(r)$ solve the following:

$$\left[\frac{d}{dr} \left(r \frac{dG_r}{dr} \right) + \left(k^2 r - \frac{m^2}{r} \right) \right]_{T(r)}^{U(r)} = 0. \quad (\text{B.39})$$

Note $U(r)$ satisfies the boundary condition at $r = a$ and $T(r)$ satisfies the radiation condition as $r \rightarrow \infty$. The above equation is Bessel's equation, and Bessel's equation is solved by Bessel, Neumann, and Hankel functions.

$U(r)$ will be used to construct the solution for when $r < r'$. In this region, either standing waves or waves radiating outward (depending on θ) are expected. Therefore, the form of the solution for $U(r)$ is written as

$$U(r) = AJ_m(kr) + BH_m^{(2)}(kr). \quad (\text{B.40})$$

The boundary condition at $r = a$ results in $U'(r = a) = 0$. Therefore, the relationship between the coefficients, A and B , can be found.

$$B = -A \frac{J'_m(ka)}{H_m^{(2)'}(ka)} \quad (\text{B.41})$$

Letting $A = 1$, the result is

$$U(r) = J_m(kr) - \frac{J'_m(ka)}{H_m^{(2)'}(ka)} H_m^{(2)}(kr). \quad (\text{B.42})$$

For $T(r)$, the form of the solution is

$$T(r) = C H_m^{(1)}(kr) + D H_m^{(2)}(kr). \quad (\text{B.43})$$

$T(r)$ will have to satisfy the radiation condition. This requires that $C = 0$. Thus

$$T(r) = H_m^{(2)}(kr), \quad (\text{B.44})$$

where $D = 1$. The Green's function will have the form

$$G_r = \frac{U(r_<)T(r_>)}{c}, \quad (\text{B.45})$$

where $r_<$ is the lesser of r and r' , $r_>$ is the greater of r and r' , and c is the conjunct and is defined as

$$c = r[TU' - T'U]. \quad (\text{B.46})$$

The relevant equations are

$$\begin{aligned} U(r) &= J_m(kr) - \frac{J'_m(ka)}{H_m^{(2)'}(ka)} H_m^{(2)}(kr), \\ U'(r) &= J'_m(kr) - \frac{J'_m(ka)}{H_m^{(2)'}(ka)} H_m^{(2)'}(kr), \\ T(r) &= H_m^{(2)}(kr), \\ T'(r) &= H_m^{(2)'}(kr), \end{aligned} \quad (\text{B.47})$$

Solving for the conjunct, the result is

$$c = r \left[J'_m(kr)H_m^{(2)}(kr) - \frac{J'_m(ka)}{H_m^{(2)}(ka)}H_m^{(2)}(kr)H_m^{(2)}(kr) \right. \\ \left. - J_m(kr)H_m^{(2)}(kr) \frac{J'_m(ka)}{H_m^{(2)}(ka)}H_m^{(2)}(kr)H_m^{(2)}(kr) \right], \quad (\text{B.48})$$

which simplifies to

$$c = r [J'_m(kr)H_m^{(2)}(kr) - J_m(kr)H_m^{(2)}(kr)]. \quad (\text{B.49})$$

Knowing that

$$H_m^{(2)}(kr) = J_m(kr) - jY_m(kr), \quad (\text{B.50}) \\ H_m^{(2)}(kr) = J'_m(kr) - jY'_m(kr),$$

it is found that

$$c = r [J'_m(kr)J_m(kr) - jJ'_m(kr)Y_m(kr) - J'_m(kr)J_m(kr) + jJ_m(kr)Y'_m(kr)], \quad (\text{B.51})$$

which reduces to

$$c = jr[J_m(kr)Y'_m(kr) - J'_m(kr)Y_m(kr)]. \quad (\text{B.52})$$

Using the identity

$$J_m(kr)Y'_m(kr) - J'_m(kr)Y_m(kr) = \frac{2}{\pi r}, \quad (\text{B.53})$$

it is found that

$$c = j\frac{2}{\pi}, \quad (\text{B.54})$$

which is a constant, as it should be.

Next, the Green's function is written as

$$G_r = -j\frac{\pi}{2} \left[J_m(kr_{<}) - \frac{J'_m(ka)}{H_m^{(2)}(ka)}H_m^{(2)}(kr_{<}) \right] H_m^{(2)}(kr_{>}). \quad (\text{B.55})$$

Subbing back into the standard form

$$G(r, \theta; r', \theta') = \sum_{m=0}^{\infty} \tilde{u}_m(\theta) \tilde{u}_m^*(\theta') G_r(r, r'; \lambda_m), \quad (\text{B.56})$$

the result is

$$G(r, \theta; r', \theta') = -\frac{j}{4} \sum_{m=0}^{\infty} \epsilon_m \cos m(\theta - \theta') \left[J_m(kr_{<}) - \frac{J'_m(ka)}{H_m^{(2)'}(ka)} H_m^{(2)}(kr_{<}) \right] H_m^{(2)}(kr_{>}). \quad (\text{B.57})$$

To ensure this is the correct answer, a coordinate shift can be performed. First, let $a \rightarrow 0$ and then shift the coordinate system such that $r' = 0$ i.e. move the origin of the system to the location of the line source. The Green's function should reduce to the Green's function for the radiation from a magnetic line source in free space.

First note that for $a = 0$, the term $\frac{J'_m(ka)}{H_m^{(2)'}(ka)}$ will vanish for all m . This is because for all m , the denominator, $H_m^{(2)'}(0)$ goes to $-\infty$. Therefore, if $a \rightarrow 0$, the Green's function becomes

$$G(r, \theta; r', \theta') = -\frac{j}{4} \sum_{m=0}^{\infty} \epsilon_m \cos m(\theta - \theta') J_m(kr_{<}) H_m^{(2)}(kr_{>}). \quad (\text{B.58})$$

A coordinate transformation can be performed such that the origin is shifted to r' .

$$\begin{aligned} r_{<} &= 0 \\ r_{>} &= |\bar{r} - \bar{r}'| \end{aligned} \quad (\text{B.59})$$

The Green's function can be rewritten as

$$G(r, \theta; r', \theta') = -\frac{j}{4} \sum_{m=0}^{\infty} \epsilon_m \cos m(\theta - \theta') J_m(0) H_m^{(2)}(k|\bar{r} - \bar{r}'|). \quad (\text{B.60})$$

It is known that $J_m(0) = 1$ only when $m = 0$. For all other possible values for m , $J_m(0) = 0$. Thus, the summation is no longer required, and the result is

$$G(r, \theta; r', \theta') = -\frac{j}{4} H_0^{(2)}(k|\bar{r} - \bar{r}'|), \quad (\text{B.61})$$

which is the correct answer. Thus, the methodology used is correct, and the Green's function for an infinite magnetic line source radiating in the presence of a PEC with radius a surrounded by a layered material can be developed. For the geometry shown in Figure B.1, all the media are homogeneous. Thus, the same governing wave equation applies with the only change being to the wave number. Specifically, the equation that must be solved is

$$\nabla_t^2 F_z + k^2 F_z = -\varepsilon M_z \quad (\text{B.62})$$

where

$$k = \begin{cases} k_1 = \pm\omega\sqrt{\mu_{r1}\varepsilon_{r1}\mu_o\varepsilon_o} & a < r < r_1 \\ k_i = \pm\omega\sqrt{\mu_{ri}\varepsilon_{ri}\mu_o\varepsilon_o} & r_i < r < r_{i+1} \\ k_{n+1} = k_o = \omega\sqrt{\mu_o\varepsilon_o} & r > r_n \end{cases} \quad (\text{B.63})$$

where $i = 2, 3, \dots, n$. The same boundary conditions as before apply and are repeated here for convenience

$$\begin{aligned} \frac{\partial F_z}{\partial r} \Big|_{r=a} &= 0, \\ \frac{\partial F_z}{\partial r} \Big|_{r \rightarrow \infty} &= -jk F_z \Big|_{r \rightarrow \infty}, \\ F_z(r, \theta) &= F_z(r, \theta + 2\pi). \end{aligned} \quad (\text{B.64})$$

Additionally, there are now multiple junction conditions at $r = r_1, r = r_2, \dots, r = r_n$.

These are

$$\begin{aligned} F_z \Big|_{r=r_m^-} &= F_z \Big|_{r=r_m^+}, \\ \frac{1}{\varepsilon^-} \frac{\partial F_z}{\partial r} \Big|_{r=r_m^-} &= \frac{1}{\varepsilon^+} \frac{\partial F_z}{\partial r} \Big|_{r=r_m^+}, \end{aligned} \quad (\text{B.65})$$

where $m = 1, 2, \dots, n$ and ε^- and ε^+ are the relative permittivities in the regions around the boundary. The Green's function solves

$$\nabla_t^2 G(\bar{r}, \bar{r}') + k^2 G(\bar{r}, \bar{r}') = -\frac{\delta(r - r')\delta(\theta - \theta')}{r}. \quad (\text{B.66})$$

The solution can be found by

$$G(r, \theta; r', \theta') = \sum_{m=0}^{\infty} \tilde{u}_m(\theta) \tilde{u}_m^*(\theta') G_r(r, r'; \lambda_m). \quad (\text{B.67})$$

From this point, the development proceeds exactly as it did for the unlayered PEC. It has been shown that

$$\sum_{m=0}^{\infty} \tilde{u}_m(\theta) \tilde{u}_m^*(\theta') = \frac{1}{2\pi} \sum_{m=0}^{\infty} \epsilon_m \cos [m(\theta - \theta')]. \quad (\text{B.68})$$

The Green's function, $G_r(r, r'; \lambda_m)$, can be found using the U-T method where $U(r)$ and $T(r)$ satisfy

$$\left[\frac{d}{dr} \left(r \frac{dG_r}{dr} \right) + \left(k^2 r - \frac{m^2}{r} \right) \right]_{T(r)}^{U(r)} = 0. \quad (\text{B.69})$$

There are now multiple regions necessitating the need to write the form for the solution of $U(r)$ and $T(r)$ in each region and then apply the junction conditions to solve for the unknown constants. The form for $U(r)$ in each region is

$$U(r) = \begin{cases} A_m^1 J_m(k_1 r) + B_m^1 H_m^{(2)}(k_1 r) & a < r < r_1, \\ A_m^i J_m(k_i r) + B_m^i H_m^{(2)}(k_i r) & r_{i-1} < r < r_i, \end{cases} \quad (\text{B.70})$$

where $i = 2, 3, \dots, n+1$, n is the number of layers material, and $r = r_{n+1}$ is understood such that $r_{n+1} \rightarrow \infty$. Note the first equation must satisfy the boundary condition at $r = a$. B_m^1 has already been found in previous parts of this exam, and it is the same here due to the same boundary condition at $r = a$.

$$B_m^1 = -\frac{J'_m(k_1 a)}{H_m^{(2)'}(k_1 a)} \quad (\text{B.71})$$

A similar procedure is followed when solving for $T(r)$. First, the forms of the solution for $T(r)$ in the various regions are

$$T(r) = \begin{cases} C_m^1 J_m(k_1 r) + D_m^1 H_m^{(2)}(k_1 r) & a < r < r_1, \\ C_m^i J_m(k_i r) + D_m^i H_m^{(2)}(k_i r) & r_{i-1} < r < r_i. \end{cases} \quad (\text{B.72})$$

Like before, the solution for the coefficients in a particular region are already known, except in this case, the known coefficients are C_m^{n+1} and D_m^{n+1} due to the same bound-

ary condition as $r \rightarrow \infty$.

$$\begin{aligned} C_m^{n+1} &= 0 \\ D_m^{n+1} &= 1 \end{aligned} \tag{B.73}$$

Note G_r will again have the form

$$G_r = \frac{U(r_<)T(r_>)}{c}, \tag{B.74}$$

where c is the conjunct and is equal to

$$c = \frac{j2A_m^{n+1}}{\pi}. \tag{B.75}$$

The magnetic line source will always be in the free space region. Additionally, this formulation will only be used such that $r \leq r'$. Substituting these results in the final form for the Green's function, $G(r, \theta; r', \theta')$ for a PEC cylinder of radius a surrounded by n layers of dielectrics with varying radii, r_i in the presence of an infinite magnetic line source. There are two forms. The first is for the region $r_{i-1} < r < r_i$.

$$G(r, \theta; r', \theta') = -\frac{j}{4} \sum_{m=0}^{\infty} \frac{\epsilon_m}{A_m^{n+1}} \cos[m(\theta - \theta')] \left[A_m^i J_m(k_i r) + B_m^i H_m^{(2)}(k_i r) \right] H_m^{(2)}(k_o r') \tag{B.76}$$

The second is for the region $r > r_n$.

$$G(r, \theta; r', \theta') = -\frac{j}{4} \sum_{m=0}^{\infty} \frac{\epsilon_m}{A_m^{n+1}} \cos[m(\theta - \theta')] \left[A_m^{n+1} J_m(k_o r_<) + B_m^{n+1} H_m^{(2)}(k_o r_<) \right] H_m^{(2)}(k_o r_>), \tag{B.77}$$

where

$$A_m^{n+1} = 1, \tag{B.78}$$

$$B_m^1 = -A_m^1 \frac{J'_m(k_1 a)}{H_m^{(2)'}(k_1 a)}, \tag{B.79}$$

and $i = 2, 3 \dots n$. The A_m^i and B_m^i coefficients are found by applying the junction conditions at the radial interfaces.

$$A_m^1 \left[J_m(k_1 r_1) - \frac{J'_m(k_1 a)}{H_m^{(2)}(k_1 a)} H_m^{(2)}(k_1 r_1) \right] = A_m^2 J_m(k_2 r_1) + B_m^2 H_m^{(2)}(k_2 r_1) \quad (\text{B.80})$$

$$A_m^1 \left[J'_m(k_1 r_1) - \frac{J'_m(k_1 a)}{H_m^{(2)}(k_1 a)} H_m^{(2)}(k_1 r_1) \right] = A_m^2 J'_m(k_2 r_1) + B_m^2 H_m^{(2)'}(k_2 r_1) \quad (\text{B.81})$$

$$A_m^2 J_m(k_2 r_2) + B_m^2 H_m^{(2)}(k_2 r_2) = A_m^3 J_m(k_3 r_2) + B_m^3 H_m^{(2)}(k_3 r_2) \quad (\text{B.82})$$

$$A_m^2 J'_m(k_2 r_2) + B_m^2 H_m^{(2)'}(k_2 r_2) = A_m^3 J'_m(k_3 r_2) + B_m^3 H_m^{(2)'}(k_3 r_2) \quad (\text{B.83})$$

○

○

○

$$A_m^n J_m(k_n r_n) + B_m^n H_m^{(2)}(k_n r_n) = J_m(k_o r_n) + B_m^{n+1} H_m^{(2)}(k_o r_n) \quad (\text{B.84})$$

$$A_m^n J'_m(k_n r_n) + B_m^n H_m^{(2)'}(k_n r_n) = J'_m(k_o r_n) + B_m^{n+1} H_m^{(2)'}(k_o r_n) \quad (\text{B.85})$$

These equations can be written in matrix notation of the form $Ax = B$, where A is a $2n \times 2n$ matrix, B are the forcing functions, and x is the solution vector. As an example, consider a case where four layers of homogeneous material surround the PEC cylinder. The matrix to solve for the unknown coefficients is

$$\begin{bmatrix} H_m^{(2)}(k_o r_3) & -J_m(k_3 r_3) & -H_m^{(2)}(k_3 r_3) & 0 & 0 & 0 \\ H_m^{(2)'}(k_o r_3) & -J'_m(k_3 r_3) & -H_m^{(2)'}(k_3 r_3) & 0 & 0 & 0 \\ 0 & J_m(k_3 r_2) & H_m^{(2)}(k_3 r_2) & -J_m(k_2 r_2) & H_m^{(2)}(k_2 r_2) & 0 \\ 0 & J'_m(k_3 r_2) & H_m^{(2)'}(k_3 r_2) & -J'_m(k_2 r_2) & H_m^{(2)'}(k_2 r_2) & 0 \\ 0 & 0 & 0 & J_m(k_2 r_1) & H_m^{(2)}(k_2 r_1) & -J_m(k_1 r_1) + K_m H_m^{(2)}(k_1 r_1) \\ 0 & 0 & 0 & J'_m(k_2 r_1) & H_m^{(2)'}(k_2 r_1) & -J'_m(k_1 r_1) + K_m H_m^{(2)'}(k_1 r_1) \end{bmatrix} \begin{bmatrix} B_m^4 \\ A_m^3 \\ B_m^3 \\ A_m^2 \\ B_m^2 \\ A_m^1 \end{bmatrix} = \begin{bmatrix} -J_m(k_o r_3) \\ -J'_m(k_o r_3) \\ 0 \\ 0 \\ 0 \\ 0 \end{bmatrix}$$

where $K_m = \frac{J'_m(k_1 a)}{H_m^{(2)}(k_1 a)}$.

To ensure the accuracy of the derived Green's function, the form in Equation B.77 was used to determine σ_{2D} for a layered cylinder. The results were compared to those obtained using a Comsol simulation for a simplified cloak with material

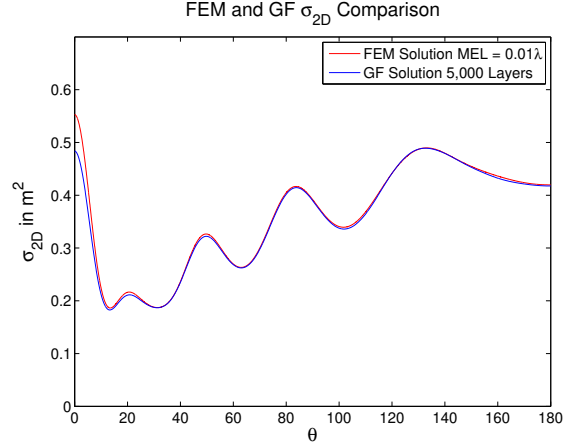


Figure B.2: Green's function and FEM results comparison

parameters put forth by Yan *et al.* and shown in Equation B.86.

$$\varepsilon_r = \left(\frac{r-a}{r}\right)^2 \frac{b}{b-a}, \quad \varepsilon_\theta = \frac{b}{b-a}, \quad \mu_z = \frac{b}{b-a} \quad (\text{B.86})$$

In order for the Green's function to approximate a radially varying cloak as described in Equation B.86, the number of layers used in the formulation must be large. The Green's function results were determined using 5,000 layers to approximate the anisotropic material. The FEM results were obtained with $\text{MEL} = 0.01\lambda$. The calculated scattering widths from the two methods were very similar, as shown in Figure B.2. The Δ for these results is 0.004 m^2 , which is quite good. There is a noticeable difference in the region where $\theta = 0^\circ$. This error can be further reduced by increasing the number of layers. Based on these results, it was concluded the Green's function was correct.

Appendix C. Vector Basis Functions

The Comsol Multiphysics software package uses the finite element method to solve the vector wave equation and associated boundary conditions. The formulation used relies heavily on that developed in Jianming Jin's book, *The Finite Element Method in Electromagnetics*, Second Edition [33]. For the simulations in this research effort, tetrahedral elements, as shown in Figure C.1, were used to discretize all three-dimensional domains. Each tetrahedral element has four vertices with coordinates (x_i^e, y_i^e, z_i^e) with $i = 1, 2, 3, 4$ (black numbers) specifying the node numbers. Within

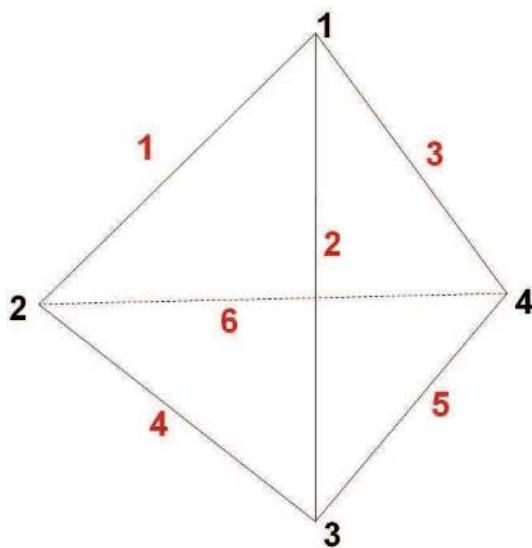


Figure C.1: Local Tetrahedral Element

each tetrahedral element, the electric field is approximated such that

$$\vec{E}^e \cong \sum_{j=1}^6 \vec{N}_j^e E_j^e \quad (\text{C.1})$$

where \vec{N}_j^e are the vector basis functions for edge j (red numbers) and the E_j^e are the unknown coefficients. Each tetrahedral element will have four nodes and six edges.

Vector basis functions (or edge functions) are used in electromagnetics because node-based expansion functions are not able to accurately represent the boundary conditions associated with various aspects of the vector fields [95]. The vector basis

Table C.1: Edge Node Numbers

Edge i	Node i_1	Node i_2
1	1	2
2	1	3
3	1	4
4	2	3
5	4	2
6	3	4

functions effectively enforce the requirement for continuity of tangential fields at interfaces. A vector basis function is defined for each edge in every element. Hence, each element has six vector basis functions. These vector basis functions, $vectN_i^e$, can be expressed as

$$\vec{N}_i^e = \vec{W}_{i_1 i_2} l_i^e = [L_{i_1} \nabla L_{i_2} - L_{i_2} \nabla L_{i_1}] l_i^e. \quad (\text{C.2})$$

Note $i = 1, 2, \dots, 6$ and is the edge number while $i_{1,2} = 1, 2, \dots, 4$ and refer to node numbers. An edge connects node i_1 to node i_2 . The values for i_1 and i_2 which correspond to the edge number are shown in Table C.1. As an example, in Figure C.1, \vec{N}_1 is the vector basis function for edge 1 (red), which connects nodes 1 and 2 (black). Similarly, \vec{N}_6 is the vector basis function for edge 6 (red) which connects nodes 3 and 4. The l_i^e term is the length of edge i .

The linear interpolation functions (L_i^e , $i = 1, 2, 3, 4$) are found using a process developed when using nodal-based expansion functions. First, the linear interpolation functions can be written as

$$L_i^e(x, y, z) = \frac{1}{6V^e} (a_i^e + b_i^e x + c_i^e y + d_i^e z). \quad (\text{C.3})$$

The yet-to-be-defined terms are the $a_i^e, b_i^e, c_i^e, d_i^e$ and V^e terms. This is done below.

In nodal-based expansion functions, the unknown function within the tetrahedral element, ϕ^e , is defined as

$$\phi^e(x, y, z) = a^e + b^e x + c^e y + d^e z. \quad (\text{C.4})$$

Evaluating ϕ^e at each node yields

$$\begin{aligned}
\phi_1^e &= a^e + b^e x_1 + c^e y_1 + d^e z_1 \\
\phi_2^e &= a^e + b^e x_2 + c^e y_2 + d^e z_2 \\
\phi_3^e &= a^e + b^e x_3 + c^e y_3 + d^e z_3 \\
\phi_4^e &= a^e + b^e x_4 + c^e y_4 + d^e z_4
\end{aligned} \tag{C.5}$$

These can be written in matrix form as

$$\begin{pmatrix} 1 & x_1^e & y_1^e & z_1^e \\ 1 & x_2^e & y_2^e & z_2^e \\ 1 & x_3^e & y_3^e & z_3^e \\ 1 & x_4^e & y_4^e & z_4^e \end{pmatrix} \begin{bmatrix} a^e \\ b^e \\ c^e \\ d^e \end{bmatrix} = \begin{bmatrix} \phi_1^e \\ \phi_2^e \\ \phi_3^e \\ \phi_4^e \end{bmatrix}. \tag{C.6}$$

Cramer's rule can be used to solve for a^e , b^e , c^e , and d^e .

$$a^e = \frac{1}{6V^e} \det \begin{pmatrix} \phi_1^e & x_1^e & y_1^e & z_1^e \\ \phi_2^e & x_2^e & y_2^e & z_2^e \\ \phi_3^e & x_3^e & y_3^e & z_3^e \\ \phi_4^e & x_4^e & y_4^e & z_4^e \end{pmatrix}, \quad b^e = \frac{1}{6V^e} \det \begin{pmatrix} 1 & \phi_1^e & y_1^e & z_1^e \\ 1 & \phi_2^e & y_2^e & z_2^e \\ 1 & \phi_3^e & y_3^e & z_3^e \\ 1 & \phi_4^e & y_4^e & z_4^e \end{pmatrix}, \tag{C.7}$$

$$c^e = \frac{1}{6V^e} \det \begin{pmatrix} 1 & x_1^e & \phi_1^e & z_1^e \\ 1 & x_2^e & \phi_2^e & z_2^e \\ 1 & x_3^e & \phi_3^e & z_3^e \\ 1 & x_4^e & \phi_4^e & z_4^e \end{pmatrix}, \quad d^e = \frac{1}{6V^e} \det \begin{pmatrix} 1 & x_1^e & y_1^e & \phi_1^e \\ 1 & x_2^e & y_2^e & \phi_2^e \\ 1 & x_3^e & y_3^e & \phi_3^e \\ 1 & x_4^e & y_4^e & \phi_4^e \end{pmatrix}. \tag{C.8}$$

Note V^e is defined as

$$V^e = \frac{1}{6} \det \begin{pmatrix} 1 & x_1^e & y_1^e & z_1^e \\ 1 & x_2^e & y_2^e & z_2^e \\ 1 & x_3^e & y_3^e & z_3^e \\ 1 & x_4^e & y_4^e & z_4^e \end{pmatrix}. \tag{C.9}$$

Table C.2: Example Tetrahedral Element Node Locations

Node i	x_i^e	y_i^e	z_i^e
1	2	2	2
2	1	1	1
3	3	1	1
4	2	3	1

$|V^e|$ is the volume of the element. The a_j^e , b_j^e , c_j^e , and d_j^e terms are found by evaluating the determinants.

$$\begin{aligned}
 a^e &= \frac{1}{6V^e} (a_1^e \phi_1^e + a_2^e \phi_2^e + a_3^e \phi_3^e + a_4^e \phi_4^e), \\
 b^e &= \frac{1}{6V^e} (b_1^e \phi_1^e + b_2^e \phi_2^e + b_3^e \phi_3^e + b_4^e \phi_4^e), \\
 c^e &= \frac{1}{6V^e} (c_1^e \phi_1^e + c_2^e \phi_2^e + c_3^e \phi_3^e + c_4^e \phi_4^e), \\
 d^e &= \frac{1}{6V^e} (d_1^e \phi_1^e + d_2^e \phi_2^e + d_3^e \phi_3^e + d_4^e \phi_4^e).
 \end{aligned} \tag{C.10}$$

Therefore, the a_j^e , b_j^e , c_j^e , and d_j^e terms are

$$\begin{aligned}
 a_1^e &= \begin{vmatrix} x_2^e & y_2^e & z_2^e \\ x_3^e & y_3^e & z_3^e \\ x_4^e & y_4^e & z_4^e \end{vmatrix}, & a_2^e &= \begin{vmatrix} x_1^e & y_1^e & z_1^e \\ x_3^e & y_3^e & z_3^e \\ x_4^e & y_4^e & z_4^e \end{vmatrix}, & a_3^e &= \begin{vmatrix} x_1^e & y_1^e & z_1^e \\ x_2^e & y_2^e & z_2^e \\ x_4^e & y_4^e & z_4^e \end{vmatrix}, & a_4^e &= \begin{vmatrix} x_1^e & y_1^e & z_1^e \\ x_2^e & y_2^e & z_2^e \\ x_3^e & y_3^e & z_3^e \end{vmatrix} \\
 b_1^e &= \begin{vmatrix} 1 & y_2^e & z_2^e \\ 1 & y_3^e & z_3^e \\ 1 & y_4^e & z_4^e \end{vmatrix}, & b_2^e &= \begin{vmatrix} 1 & y_1^e & z_1^e \\ 1 & y_3^e & z_3^e \\ 1 & y_4^e & z_4^e \end{vmatrix}, & b_3^e &= \begin{vmatrix} 1 & y_1^e & z_1^e \\ 1 & y_2^e & z_2^e \\ 1 & y_4^e & z_4^e \end{vmatrix}, & b_4^e &= \begin{vmatrix} 1 & y_1^e & z_1^e \\ 1 & y_2^e & z_2^e \\ 1 & y_3^e & z_3^e \end{vmatrix} \\
 c_1^e &= \begin{vmatrix} 1 & x_2^e & z_2^e \\ 1 & x_3^e & z_3^e \\ 1 & x_4^e & z_4^e \end{vmatrix}, & c_2^e &= \begin{vmatrix} 1 & x_1^e & z_1^e \\ 1 & x_3^e & z_3^e \\ 1 & x_4^e & z_4^e \end{vmatrix}, & c_3^e &= \begin{vmatrix} 1 & x_1^e & z_1^e \\ 1 & x_2^e & z_2^e \\ 1 & x_4^e & z_4^e \end{vmatrix}, & c_4^e &= \begin{vmatrix} 1 & x_1^e & z_1^e \\ 1 & x_2^e & z_2^e \\ 1 & x_3^e & z_3^e \end{vmatrix} \\
 d_1^e &= \begin{vmatrix} 1 & x_2^e & y_2^e \\ 1 & x_3^e & y_3^e \\ 1 & x_4^e & y_4^e \end{vmatrix}, & d_2^e &= \begin{vmatrix} 1 & x_1^e & y_1^e \\ 1 & x_3^e & y_3^e \\ 1 & x_4^e & y_4^e \end{vmatrix}, & d_3^e &= \begin{vmatrix} 1 & x_1^e & y_1^e \\ 1 & x_2^e & y_2^e \\ 1 & x_4^e & y_4^e \end{vmatrix}, & d_4^e &= \begin{vmatrix} 1 & x_1^e & y_1^e \\ 1 & x_2^e & y_2^e \\ 1 & x_3^e & y_3^e \end{vmatrix}
 \end{aligned}$$

In the above matrices, (x_i^e, y_i^e, z_i^e) , $i = 1, 2, 3, 4$, are the coordinates of the nodes of the tetrahedral elements.

As an example, consider a tetrahedral element with the vertices shown in Table C.2. First, evaluate V^e .

$$V^e = \frac{1}{6} \det \begin{pmatrix} 1 & 2 & 2 & 2 \\ 1 & 1 & 1 & 1 \\ 1 & 3 & 1 & 1 \\ 1 & 2 & 3 & 1 \end{pmatrix} = -\frac{2}{3} \quad (\text{C.11})$$

Note the volume of the tetrahedral element as defined in Table C.2 can be found by

$$V = \frac{1}{3} A_o h = \frac{1}{3} \left(\frac{1}{2} (2)(2) \right) 1 = \frac{2}{3}. \quad (\text{C.12})$$

Thus, $|V^e|$ does equal the volume of the element. Next, evaluate the a_i^e , b_i^e , c_i^e , and d_i^e elements using the matrices defined above.

$$\begin{aligned} a_1^e &= 4, & a_2^e &= -8, & a_3^e &= 0, & a_4^e &= 0, \\ b_1^e &= 0, & b_2^e &= 2, & b_3^e &= -2, & b_4^e &= 0, \\ c_1^e &= 0, & c_2^e &= 1, & c_3^e &= 1, & c_4^e &= -2, \\ d_1^e &= -4, & d_2^e &= 1, & d_3^e &= 1, & d_4^e &= 2. \end{aligned} \quad (\text{C.13})$$

Using these values, the linear interpolation functions, L_i^e , are

$$\begin{aligned} L_1^e(x, y, z) &= -1 + z, \\ L_2^e(x, y, z) &= -\frac{1}{4} (2x + y + z - 8), \\ L_3^e(x, y, z) &= -\frac{1}{4} (-2x + y + z), \\ L_4^e(x, y, z) &= -\frac{1}{4} (-2y + 2z), \end{aligned} \quad (\text{C.14})$$

with the gradients being

$$\begin{aligned} \nabla L_1^e &= \hat{z}, \\ \nabla L_2^e &= -\frac{1}{4} (2\hat{x} + \hat{y} + \hat{z}), \\ \nabla L_3^e &= -\frac{1}{4} (-2\hat{x} + \hat{y} + \hat{z}), \\ \nabla L_4^e &= -\frac{1}{4} (-2\hat{y} + 2\hat{z}). \end{aligned} \quad (\text{C.15})$$

The lengths of each side in the tetrahedral element are

$$\begin{aligned} l_1^e &= \sqrt{3}, & l_2^e &= \sqrt{3}, & l_3^e &= \sqrt{2}, \\ l_4^e &= 2, & l_5^e &= \sqrt{5}, & l_6^e &= \sqrt{5}. \end{aligned} \tag{C.16}$$

It is now possible to determine the N_j^e functions.

$$\begin{aligned} \vec{W}_{12} &= -\frac{1}{4} [(2z - 2) \hat{x} + (z - 1) \hat{y} + (7 - 2x - y) \hat{z}], \\ \vec{W}_{13} &= -\frac{1}{4} [(2 - 2z) \hat{x} + (z - 1) \hat{y} + (2x - y - 1) \hat{z}], \\ \vec{W}_{14} &= -\frac{1}{4} [(2 - 2z) \hat{y} + (2y - 2) \hat{z}], \\ \vec{W}_{23} &= -\frac{1}{4} [(y + z + 4) \hat{x} + (-x + 2) \hat{y} + (-x + 2) \hat{z}], \\ \vec{W}_{42} &= -\frac{1}{4} [(y - z) \hat{x} + (-x - z + 4) \hat{y} + (x + y - 16) \hat{z}], \\ \vec{W}_{34} &= -\frac{1}{4} [(y - z) \hat{x} + (-x + z) \hat{y} + (x - y) \hat{z}]. \end{aligned} \tag{C.17}$$

Note that for all $\vec{W}_{i_1 i_2}$, the following hold:

$$\begin{aligned} \nabla \cdot \vec{W}_{i_1 i_2} &= 0, \\ \nabla \times \vec{W}_{i_1 i_2} &= 2 \nabla L_{l_1}^e \times \nabla L_{l_2}^e, \\ \vec{e}_i \cdot \nabla L_{l_1}^e &= -\frac{1}{l_i^e}, \\ \vec{e}_i \cdot \nabla L_{l_2}^e &= \frac{1}{l_i^e}, \end{aligned} \tag{C.18}$$

where \vec{e}_j is a unit vector for edge i pointing from node i_1 to node i_2 . By satisfying these constraints, all $\vec{W}_{i_1 i_2}$ vectors have a constant tangential component along the i^{th} edge while having no tangential component along the five other edges. Thus, the vector-based edge elements are well-suited for electromagnetics problems. The final

vector-based edge elements are

$$\begin{aligned}
\vec{N}_1^e &= \vec{W}_{12}l_1^e = -\frac{\sqrt{3}}{4} [(2z - 2) \hat{x} + (z - 1) \hat{y} + (7 - 2x - y) \hat{z}], \\
\vec{N}_2^e &= \vec{W}_{13}l_2^e = -\frac{\sqrt{3}}{4} [(2 - 2z) \hat{x} + (z - 1) \hat{y} + (2x - y - 1) \hat{z}], \\
\vec{N}_3^e &= \vec{W}_{14}l_3^e = -\frac{\sqrt{2}}{4} [(2 - 2z) \hat{y} + (2y - 2) \hat{z}], \\
\vec{N}_4^e &= \vec{W}_{23}l_4^e = -\frac{2}{4} [(y + z + 4) \hat{x} + (-x + 2) \hat{y} + (-x + 2) \hat{z}], \\
\vec{N}_5^e &= \vec{W}_{42}l_5^e = -\frac{\sqrt{5}}{4} [(y - z) \hat{x} + (-x - z + 4) \hat{y} + (x + y - 16) \hat{z}], \\
\vec{N}_6^e &= \vec{W}_{34}l_6^e = -\frac{\sqrt{5}}{4} [(y - z) \hat{x} + (-x + z) \hat{y} + (x - y) \hat{z}].
\end{aligned} \tag{C.19}$$

Thus, given any tetrahedral element within a domain, the above method is used to determine the linear, vector-based edge elements which will approximate the solution within each element. This is done for each element within the domain. The unknowns are manipulated into a system of equations which are solved using standard techniques such as conjugate gradient.

Bibliography

1. “How Stealth is Achieved on F-117a,” <http://www.aeronautics.ru/f117a.htm>.
2. “Metamaterials Hold Key to Cloak of Invisibility,” <http://www.eetimes.com/showArticle.jhtml?articleID=191901472>.
3. “Radar Absorbant Material,” http://en.wikipedia.org/wiki/Radar_absorbent_material.
4. “RCS Facility Design: The Howland Company,” <http://www.thehowlandcompany.com/RCS-ranges.htm>.
5. “Studying Stealth: Air Force Begins Operation of Largest Wide Band Imaging and RCS Test Facility,” <http://gtresearchnews.gatech.edu/newsrelease/BICOMS.html>.
6. “Sukhoi’s Lightning Strikes the F-35 JSF,” <http://www.ausairpower.net/APA-NOTAM-030907-1.html>.
7. Abramowitz, Milton and Irene A. Stegun (editors). *Handbook of Mathematical Functions with Formulas, Graphs, and Mathematical Tables*. Dover Publications, Inc., New York, New York, 1970.
8. Alù, Andrea and Nader Engheta. “Achieving transparency with plasmonic and metamaterial coatings,” *Phys. Rev. E: Stat. Phys., Plasmas, Fluids*, 72(1), 2005.
9. Alù, Andrea and Nader Engheta. “Plasmonic materials in transparency and cloaking problems: mechanism, robustness, and physical insights,” *Opt. Express*, 15(6):3318–3332, 2007.
10. Arslanagic, S. and O. Breinbjerg. “Electric-line-source illumination of a circular cylinder of lossless double-negative material: an investigation of near field, directivity, and radiation resistance,” *IEEE Antennas Propag. Mag.*, 48(3):38–54, 2006.
11. Aydin, K. and E. Ozbay. “Capacitor-loaded split ring resonators as tunable metamaterial components,” *J. Appl. Phys.*, 101(2), 2007.
12. Aydin, Koray, Irfan Bulu, Kaan Guven, Maria Kafesaki, Costas M. Soukoulis, and Ekmel Ozbay. “Investigation of magnetic resonances for different split-ring resonator parameters and designs,” *New J. Phys.*, 7:168, 2005.
13. Balanis, Constatine A. *Advanced Engineering Electromagnetics*. John Wiley & Sons, Inc, Hoboken, New Jersey, 1989.
14. Cai, Wenshan, Uday K. Chettiar, Alexander V. Kildishev, and Vladimir M. Shalaev. “Optical Cloaking with Metamaterials,” *Nat. Photonics*, 224–228, Apr 2007.

15. Cai, Wenshan, Uday K. Chettiar, Alexander V. Kildishev, Vladimir M. Shalaev, and Graeme W. Milton. "Nonmagnetic cloak with minimized scattering," *Appl. Phys. Lett.*, 91(11), 2007.
16. Chen, H. S., L. X. Ran, J. T. Huangfu, X. M. Zhang, K. S. Cheng, T. M. Grzegorzczuk, and J. A. Kong. "Magnetic properties of s shaped split-ring resonators," *Prog. Electromagn. Res.*, 51:231–247, 2005.
17. Chen, Hongshen, Lixin Ran, Jiangtao Huangfu, Xianmin Zhang, Knagsheng Chen, Tomasz M. Grzegorzczuk, and Jin Au Kong. "Left-handed materials composed of only S-shaped resonators," *Phys. Rev. E: Stat. Phys., Plasmas, Fluids*, 70(5), 2004.
18. Chen, Hongshen, Bae-Ian Wu, Baile Zhang, and Jin Au Kong. "Electromagnetic Wave Interactions with a Metamaterial Cloak," *Phys. Rev. Lett.*, 99(6), 2007.
19. Chen, Hongshen, Jingjing Zhang, Yang Bai, Yu Luo, Lixin Ran, Qin Jiang, and Jin Au Kong. "Experimental retrieval of the effective parameters of metamaterials based on a waveguide method," *Opt. Express*, 14(26):12944–12949, 2006.
20. Chen, Huanyang, Zixian Liang, Peijun Yao, Xunya Jiang, Hongru Ma, and C. T. Chan. "Extending the bandwidth of electromagnetic cloaks," *Phys. Rev. B: Condens. Matter*, 76(24), 2007.
21. Chen, Huanyang, Xudong Luo, Hongru Ma, and C. T. Chan. "The Anti-Cloak," *Opt. Express*, 16(19):14603–14608, 2008.
22. Chen, Xudong, Tomasz M. Grzegorzczuk, Bae-Ian Wu, Joe Pacheco, and Jin Au Kong. "Robust method to retrieve the constitutive effective parameters of metamaterials," *Phys. Rev. E: Stat. Phys., Plasmas, Fluids*, 70(1), 2004.
23. Collin, Robert E. *Field Theory of Guided Waves*. John Wiley & Sons, Inc, New York, New York, second edition, 1991.
24. Collins, Peter J. "EENG 627 Class Notes," 2007.
25. Collins, Peter J. "EENG 725 Class Notes," 2007.
26. Collins, Peter J. and Jeffrey S. McGuirk. "A novel methodology for deriving improved material parameter sets for simplified cylindrical cloaks," *J. Opt. A: Pure Appl. Opt.*, 11(1), 2009.
27. Comsolab. *Comsol Multiphysics User's Guide Version 3.4*. 2007.
28. Cummer, Steven A., Bogdan-Ioan Popa, David Schurig, David R. Smith, and John Pendry. "Full-wave simulations of electromagnetic cloaking structures," *Phys. Rev. E: Stat. Phys., Plasmas, Fluids*, 74(3), 2006.
29. Degiron, Aloyse, Jack J. Mock, and David R. Smith. "Modulating and tuning the response of metamaterials at the unit cell level," *Opt. Express*, 15(3):1115–1127, 2007.

30. Engheta, Nader and Richard Ziolkowski (editors). *Metamaterials Physics and Engineering Exploration*. John Wiley & Sons, Inc, Hoboken, New Jersey, 2006.
31. Fischer, Brian E., John L. Volakis, and Andrew E. Yagle. "Computation and Use of Characteristic Frequency Modes for Patch Antenna Design." *2007 Antenna Measurement and Techniques Association*. St. Louis, MO, 2007.
32. Fischer, Brian E., Andrew E. Yagle, and John L. Volakis. "On the Eigen-Decomposition of Electromagnetic Systems and the Frequency Dependence of the Associated Eigenvalues." *2005 IEEE Antennas and Propagation Conference*. Washington D.C., 2005.
33. Frei, Walter R. "Question 1, Case 257448," Email, May 2009.
34. Frei, Walter R. "Question 2, Case 257448," Email, May 2009.
35. Gaillot, Davy P., Charles Croënne, and Didier Lippens. "An all-dielectric route for terahertz cloaking," *Opt. Express*, 16(6):3986–3992, 2008.
36. Gil, I., J. García-García, J. Bonache, F. Martín, M. Sorolla, and R. Marqués. "Varactor-loaded split ring resonators for tunable notch filters at microwave frequencies," *Electron. Lett.*, 40(21):1347–1348, Oct. 2004.
37. Greigor, R., C. Parazzoli, K. Li, B. E. C. Koltenbah, and M. Tanielian. "Experimental determination and numerical simulation of the properties of negative index of refraction materials," *Opt. Express*, 11(7):688–695, 2003.
38. Hand, Thomas and Steven Cummer. "Characterization of tunable metamaterial elements using MEMS switches," *IEEE Antennas Wirel. Propag. Lett.*, 6:401–404, 2007.
39. Havrilla, Michael J. *Analytical and experimental techniques for the electromagnetic characterization of materials*. Ph.D. Dissertation, Michigan State University, 2001.
40. Huang, Ying, Yijun Feng, and Tian Jiang. "Electromagnetic cloaking by layered structure of homogeneous isotropic materials," *Opt. Express*, 15(18):11133–11141, 2007.
41. Huangfu, Jiangtao, Lixin Ran, Hongsheng Chen, Xian min Zhang, Kangsheng Chen, Tomasz M. Grzegorzcyk, and Jin Au Kong. "Experimental confirmation of negative refractive index of a metamaterial composed of Omega-like metallic patterns," *Appl. Phys. Lett.*, 84:1537–1539, 2004.
42. Isić, G., R. Gajić, B. Novaković, Z. V. Popović, and K. Hingerl. "Radiation and scattering from imperfect cylindrical electromagnetic cloaks," *Opt. Express*, 16(3):1413–1422, 2008.
43. Isić, G., R. Gajić, B. Novaković, Z.V. Popović, and K. Hingerl. "Imperfect cloaking devices based on metamaterials," *Acta Physica Polonica A*, 112(5):1083–1088, 2007.

44. Jiang, Wei X., Jessie Y. Chin, Zhuo Li, Qiang Cheng, Ruopeng Liu, and Tie J. Cui. "Analytical design of conformally invisible cloaks for arbitrarily shaped objects," *Phys. Rev. E: Stat. Phys., Plasmas, Fluids*, 77(6), 2008.
45. Jiang, Wei X., Tie J. Cui, Guan X. Yu, Xian Q. Lin, Qiang Cheng, and Jessie Y. Chin. "Arbitrarily elliptical-cylindrical invisible cloaking," *J. Phys. D: Appl. Phys.*, 41, 2008.
46. Jin, Jianming. *The Finite Element Method in Electromagnetics*. John Wiley & Sons, Inc., second edition, 2002.
47. Kildal, Per-Simon, Ahmed Kishk, and Zvonimir Sipus. "RF invisibility using metamaterials: Harry Potters Cloak or The Emperors New Clothes?," *IEEE Antennas Propag. International Symposium*.
48. Knott, Eugene F. *Radar Cross Section Measurements*. Scitech Publishing, Inc, Raleigh, North Carolina, 2006.
49. Knott, Eugene F., John F. Shaeffer, and Michael T. Tuley. *Radar Cross Section*. Scitech Publishing, Inc, Raleigh, North Carolina, second edition, 2004.
50. Kock, Winston E. "Metal-Lens Antennas," *Proceedings of the IRE*, 34(11):828–836, 1946.
51. Kock, Winston E. "Metallic Delay Lenses," *Bell System Technical Journal*, 27:58–82, 1948.
52. Kong, Jin Au. *Advanced Electromagnetic Wave Theory*. John Wiley & Sons, Inc., second edition, 1990.
53. Kwon, Do-Hoon and Douglas H. Werner. "Two-dimensional eccentric elliptic electromagnetic cloaks," *Appl. Phys. Lett.*, 92(1), 2008.
54. Lapine, M. and S. Tretyakov. "Contemporary notes on metamaterials," *IET Microwaves Antennas Propag.*, 1(1):3–11, Feb 2007.
55. Leonhardt, Ulf. "Optical Conformal Mapping," *Science*, 312(5781):1777–1780, 2006.
56. Leonhardt, Ulf and Thomas G. Philbin. "General relativity in electrical engineering," *New J. Phys.*, 8(10), 2006.
57. Lerat, Jean-Marie, Nicolas Malléjac, and Olivier Acher. "Determination of the effective parameters of a metamaterial by field summation method," *J. Appl. Phys.*, 100(8), 2006.
58. Li, Zhaofeng, Koray Aydin, and Ekmel Ozbay. "Determination of the effective constitutive parameters of bianisotropic metamaterials from reflection and transmission coefficients," *Phys. Rev. E: Stat. Phys., Plasmas, Fluids*, 79(2), 2009.

59. Liang, Zixian, Peijin Yao, Xiaowei Sun, and Xunya Jiang. “The physical picture and the essential elements of the dynamical process for dispersive cloaking structures,” *Appl. Phys. Lett.*, 92(13), 2008.
60. Ma, Hua, Shaobo Qu, Zhuo Xu, Jieqiu Zhang, Biwu Chen, and Jiafu Wang. “Material parameter equation for elliptical cylindrical cloaks,” *Phys. Rev. A: At. Mol. Opt. Phys.*, 77(1), 2008.
61. Markoš, Peter and C. Soukoulis. “Transmission properties and effective electromagnetic parameters of double negative metamaterials,” *Opt. Express*, 11(7):649–661, 2003.
62. Marqués, Ricardo, Francisco Medina, and Rachid Rafii-El-Idrissi. “Role of bianisotropy in negative permeability and left-handed metamaterials,” *Phys. Rev. B: Condens. Matter*, 65(14), 2002.
63. McGuirk, Jeffrey S. and Peter J. Collins. “Controlling the transmitted field into a cylindrical cloak’s hidden region,” *Opt. Express*, 16(22):17560–17573, 2008.
64. McNamara, D. A., C. W. I. Pistorius, and J. A. G. Malherbe. *Introduction to the Uniform Geometrical Theory of Diffraction*. Artech House, Norwood, Massachusetts, 1990.
65. Miller, David A. B. “On perfect cloaking,” *Opt. Express*, 14(25):12457–12466, 2006.
66. Munk, Ben A. *Metamaterials: Critique and Alternatives*. Wiley, New York, New York, 2009.
67. Nicolson, A. M. and G. F. Ross. “Measurement of the Intrinsic Properties of Materials by Time-Domain Techniques,” *IEEE Trans. Instrum. Meas.*, 19(4):377–382, Nov. 1970.
68. O’Brien, S. and J. B. Pendry. “Magnetic activity at infrared frequencies in structured metallic photonic crystals,” *J. Phys.: Condens. Matter*, 14(25):6383–6394, 2002.
69. Pendry, J. B., A. J. Holden, D. J. Robbins, and W. J. Stewart. “Low frequency plasmons in thin-wire structures,” *J. Phys.: Condens. Matter*, 10(22):4785–4809, 1998.
70. Pendry, J. B., A. J. Holden, D. J. Robbins, and W. J. Stewart. “Magnetism from conductors and enhanced nonlinear phenomena,” *IEEE Trans. Microwave Theory Tech.*, 47(11):2075–2084, 1999.
71. Pendry, J. B., A. J. Holden, W. J. Stewart, and I. Youngs. “Extremely Low Frequency Plasmons in Metallic Mesostructures,” *Phys. Rev. Lett.*, 76(25):4773–4776, 1996.
72. Pendry, J. B., D. Schurig, and D. R. Smith. “Controlling electromagnetic fields,” *Science*, 312(5781):1780–1782, 2006.

73. Rahm, Marco, David Schurig, Daniel A. Roberts, Steven A. Cummer, David R. Smith, and John B. Pendry. "Design of electromagnetic cloaks and concentrators using form-invariant coordinate transformations of Maxwell's equations," *Photon. Nanostruct.: Fundam. Appl.*, 6:87, 2008.
74. Ramo, Simon, John R. Whinnery, and Theodore Van Duzer. *Fields and Waves in Communication Electronics*. John Wiley & Sons, Inc., third edition, 1994.
75. Rederus, Luke. *A MEMS Mult-Cantilever Variable Capacitor on Metamaterial*. Master's Thesis, Air Force Institute of Technology, Air University, Wright Patterson AFB OH, 2009.
76. Rotman, Walter. "Plasma simulation by artificial dielectrics and parallel-plate media," *IEEE Trans. Antennas Propag.*, 10(1):82–95, Jan 1962.
77. Ruan, Zhichao, Min Yan, Curtis W. Neff, and Min Qiu. "Ideal Cylindrical Cloak: Perfect but Sensitive to Tiny Perturbations," *Phys. Rev. Lett.*, 99(11), 2007.
78. Sauviac, B., C. R. Simovski, and S. A. Tretyakov. "Double Split-Ring Resonators: Analytical Modeling and Numerical Simulations," 2004.
79. Schurig, D., J. J. Mock, B. J. Justice, S. A. Cummer, J. B. Pendry, A. F. Starr, and D. R. Smith. "Metamaterial Electromagnetic Cloak at Microwave Frequencies," *Science*, 314(5801):977–980, 2006.
80. Schurig, D., J. J. Mock, and D. R. Smith. "Electric-field-coupled resonators for negative permittivity metamaterials," *Appl. Phys. Lett.*, 88(4), 2006.
81. Schurig, D., J. B. Pendry, and D. R. Smith. "Calculation of material properties and ray tracing in transformation media," *Opt. Express*, 14(21):9794–9804, 2006.
82. Shadrivov, Ilya V., Steven K. Morrison, and Yuri S. Kivshar. "Tunable split-ring resonators for nonlinear negative-index metamaterials," *Opt. Express*, 14(20):9344–9349, 2006.
83. Shalaev, Vladimir M. "Transforming Light," *Science*, 322(5900):384–386, 2008.
84. Sihvola, Ari. "Metamaterials in Electromagnetics," *Metamaterials*, 1(1):3–10, Mar 2007.
85. Simovski, Constantin R. and Sailing He. "Frequency range and explicit expressions for negative permittivity and permeability for an isotropic medium formed by a lattice of perfectly conduction omega particles," *Phys. Lett. A*, 311:254–263, 2003.
86. Simovski, Constantin R. and Sergei A. Tretyakov. "Local constitutive parameters of metamaterials from an effective-medium perspective," *Phys. Rev. B: Condens. Matter*, 75(19), 2007.
87. Skolnik, Merrill I. *Introduction to Radar Systems*. McGraw-Hill, Inc., New York, New York, 1980.

88. Smith, D. R., W. J. Padilla, D. C. Vier, S. C. Nemat-Nasser, and S. Schultz. “Composite Medium with Simultaneously Negative Permeability and Permittivity,” *Phys. Rev. Lett.*, 84:4184–4187, 2000.
89. Smith, D. R., S. Schultz, P. Markoš, and C. M. Soukoulis. “Determination of effective permittivity and permeability of metamaterials from reflection and transmission coefficients,” *Phys. Rev. B: Condens. Matter*, 65(19), 2002.
90. Smith, D. R., D. C. Vier, Th. Koschny, and C. M. Soukoulis. “Electromagnetic parameter retrieval from inhomogeneous metamaterials,” *Phys. Rev. E: Stat. Phys., Plasmas, Fluids*, 71(3), 2005.
91. Smith, David R. and John B. Pendry. “Homogenization of metamaterials by field averaging (invited paper),” *J. Opt. Soc. Am. B*, 23(3):391–403, 2006.
92. Urzhumov, Y. “Nano-Photonics and Plasmonics in COMSOL Multiphysics.” *COMSOL Conference 2008 CD*. 2008.
93. Vasić, Borislav, Goran Isić, Radoš Gajić, and Kurt Hingerl. “Coordinate transformation based design of confined metamaterial structures,” *Phys. Rev. B: Condens. Matter*, 79(8), 2009.
94. Vinoy, K. J. and R. M. Jha. *Radar Absorbing Materials: From Theory to Design and Characterization*. Kluwer Academic Publishers, Boston, Massachusetts, 1996.
95. Volakis, John L., Arindam Chatterjee, and Leo C. Kempel. *Finite Element Method for Electromagnetics: Antennas, Microwave Circuits, and Scattering Applications*. IEEE Press, New York, New York, 1998.
96. Wang, Dongxing, Hongsheng Chen, Lixin Ran, Jiangtao Huangfu, Jin Au Kong, and Bae-Ian Wu. “Reconfigurable cloak for multiple operating frequencies,” *Appl. Phys. Lett.*, 93(4), 2008.
97. Ward, A. J. and J. B. Pendry. “Refraction and geometry in Maxwell’s Equations,” *J. Mod. Opt.*, 43(4):773–793, 1996.
98. Weder, Ricardo. “A rigorous analysis of high-order electromagnetic invisibility cloaks,” *J. Phys. A: Math. Theor.*, 41, 2008.
99. Weir, William B. “Automatic measurement of complex dielectric constant and permeability at microwave frequencies,” *Proc. IEEE*, 62(1):33–36, Jan. 1974.
100. Wood, B., J. B. Pendry, and D. P. Tsai. “Directed subwavelength imaging using a layered metal-dielectric system,” *Phys. Rev. B: Condens. Matter*, 74(11), 2006.
101. Yan, Min, Zhichao Ruan, and Min Qiu. “Cylindrical Invisibility Cloak with Simplified Material Parameters is Inherently Visible,” *Phys. Rev. Lett.*, 99(23), 2007.
102. Yan, Min, Zhichao Ruan, and Min Qiu. “Scattering characteristics of simplified cylindrical invisibility cloaks,” *Opt. Express*, 15(26):17772–17782, 2007.

103. Yao, H., L. Li, and C. Qiu. “Electromagnetic scattering properties in a multilayered metamaterial cylinder,” *IEEE MELECON*, 246, May 2006.
104. Yao, Peijun, Zixian Liang, and Xunya Jiang. “Limitation of the electromagnetic cloak with dispersive material,” *Appl. Phys. Lett.*, 92(3), 2008.
105. Zambonelli, Franco and Marco Mamei. “The cloak of invisibility: challenges and applications,” *IEEE Pervasive Comput.*, 1(4):62–70, Oct-Dec 2002.
106. Zhang, Jingjing, Jiangtao Huangfu, Yu Luo, Hongshen Chen, Jin Au Kong, and Bae-Ian Wu. “Cloak for multilayered and gradually changing media,” *Phys. Rev. B: Condens. Matter*, 77(3), 2008.
107. Zhouhdi, Saïd, Ari Sihvola, and Mohamed Aarsalane (editors). *Advances in Electromagnetics of Complex Media and Metamaterials*. Springer-Verlag, 2003.
108. Ziolkowski, Richard W. “Design, fabrication, and testing of double negative metamaterials,” *IEEE Trans. Antennas Propag.*, 51(7):1516–1529, 2003.

REPORT DOCUMENTATION PAGE

Form Approved
OMB No. 0704-0188

The public reporting burden for this collection of information is estimated to average 1 hour per response, including the time for reviewing instructions, searching existing data sources, gathering and maintaining the data needed, and completing and reviewing the collection of information. Send comments regarding this burden estimate or any other aspect of this collection of information, including suggestions for reducing this burden to Department of Defense, Washington Headquarters Services, Directorate for Information Operations and Reports (0704-0188), 1215 Jefferson Davis Highway, Suite 1204, Arlington, VA 22202-4302. Respondents should be aware that notwithstanding any other provision of law, no person shall be subject to any penalty for failing to comply with a collection of information if it does not display a currently valid OMB control number. **PLEASE DO NOT RETURN YOUR FORM TO THE ABOVE ADDRESS.**

1. REPORT DATE (DD-MM-YYYY) 22-09-2009		2. REPORT TYPE Doctoral Dissertation		3. DATES COVERED (From — To) Sept 2006 — Sep 2009	
4. TITLE AND SUBTITLE Electromagnetic Field Control and Optimization Using Metamaterials				5a. CONTRACT NUMBER 2007-013	
				5b. GRANT NUMBER	
				5c. PROGRAM ELEMENT NUMBER	
				5d. PROJECT NUMBER	
6. AUTHOR(S) Jeffrey S. McGuirk, Maj, USAF				5e. TASK NUMBER	
				5f. WORK UNIT NUMBER	
7. PERFORMING ORGANIZATION NAME(S) AND ADDRESS(ES) Air Force Institute of Technology Graduate School of Engineering and Management (AFIT/EN) 2950 Hobson Way WPAFB OH 45433-7765				8. PERFORMING ORGANIZATION REPORT NUMBER AFIT/DEE/ENG/09-13	
9. SPONSORING / MONITORING AGENCY NAME(S) AND ADDRESS(ES) Christopher M. Miller, LtCol, USAF National RCS Test Facility 871 DeZonia Road Holloman AFB NM 88330 575-679-3323, christopher.miller@holloman.af.mil				10. SPONSOR/MONITOR'S ACRONYM(S) 11. SPONSOR/MONITOR'S REPORT NUMBER(S)	
12. DISTRIBUTION / AVAILABILITY STATEMENT Approval for public release; distribution is unlimited.					
13. SUPPLEMENTARY NOTES					
14. ABSTRACT Transformation optics has shown the ability to cloak an object from incident electromagnetic radiation is possible. However, the material parameters are inhomogeneous, anisotropic, and, in some instances, singular at various locations. In order for a cloak to be practically realized, simplified parameter sets are required. However, the simplified parameters result in a degradation in the cloaking function. Constitutive parameters for simplified two-dimensional cylindrical cloaks have been developed with two material property constraints. It was initially believed satisfying these two constraints would result in the simplified cylindrical cloaks having the same wave equation as an ideal cloak. Because of this error, the simplified cloaks were not perfect. No analysis was done to determine all material parameter constraints to enable a perfect two-dimensional cylindrical cloak. This research developed a third constraint on the material parameters. It was shown as the material parameters better satisfy this new equation, a two-dimensional cylindrical cloak's hidden region is better shielded from incident radiation. Additionally, a novel way to derive simplified material parameters for two-dimensional cylindrical cloaks was developed. A Taylor series expansion dictated by the new constraint equation leads to simplified cloaks with significantly improved scattering width performances when compared to previous published results. During the course of this research, it was noted all cloak simulations are performed using finite element method (FEM) based numerical methods. A Green's function was used to accurately calculate scattering widths from a two-dimensional cylindrical cloak with a perfect electrically conducting inner shell. Significant time improvements were achieved using the Green's function compared to an FEM solution particularly as the computational domain size is increased. Finally, cloaks are physically realized using metamaterials. Design of metamaterials has typically been done empirically. Shifts in S-parameter measurements and the resulting extracted constitutive parameters are used to determine the impact to resonant regions due to various geometries. A new way to design and possibly optimize unit cell metamaterials was investigated using an eigendecomposition to identify the cell resonances. Different structures were shown to have different resonances, and control of the resonant locations can lead to optimum designs.					
15. SUBJECT TERMS Electromagnetics, computational electromagnetics, metamaterials, transformation optics, cloak, eigendecomposition					
16. SECURITY CLASSIFICATION OF: a. REPORT U			17. LIMITATION OF ABSTRACT UU		18. NUMBER OF PAGES 168
b. ABSTRACT U			c. THIS PAGE U		19a. NAME OF RESPONSIBLE PERSON Peter J. Collins
U			U		19b. TELEPHONE NUMBER (include area code) (937) 255-3636, ext 7256; peter.collins@afit.edu